



# Diplomarbeit

## Development of a Computation Method to account for Discrete Tip Injection in a Streamline Curvature Method

**Institut für Energietechnik und Thermodynamik**  
Technische Universität Wien

vorgelegt von:

**Richard Pichler**  
**Matr.-Nr.: 0427419**

Betreuer:

Ao.Univ.Prof. Dipl.-Ing. Dr.techn. Reinhard Willinger, TU Wien  
Dipl.-Ing. Roland Matzgeller, MTU Aero Engines GmbH

Wien, November 2010

## Eidesstattliche Erklärung

Ich erkläre an Eides statt, dass ich meine Diplomarbeit nach den anerkannten Grundsätzen für wissenschaftliche Abhandlungen selbständig ausgeführt habe und alle verwendeten Hilfsmittel, insbesondere die zugrunde gelegte Literatur genannt habe.

Weiters erkläre ich, dass ich dieses Diplomarbeitsthema bisher weder im In- noch im Ausland (einer Beurteilerin / einem Beurteiler zur Begutachtung) in irgendeiner Form als Prüfungsarbeit vorgelegt habe und dass diese Arbeit mit der vom Begutachter beurteilten Arbeit übereinstimmt.

## Statement of Affirmation

Herewith I affirm that I have written this thesis on my own. I did not enlist unlawful assistance of someone else. Cited sources of literature are perceptibly marked and listed at the end of this thesis. The work was not submitted previously in same or similar form to another examination committee and was not yet published.

Wien, am 26.11.2010

---

Richard Pichler

## Abstract

The positive effects of tip injection (i.e. injection of compressed air upstream of a rotor tip) on axial compressor operating behaviour was the topic of several investigations ([32], [30], [4], [13],...). Discrete tip injection (i.e. injection through equally distributed slots around the circumference) was found to be superior to one continuous slot around the whole circumference [27].

These investigations were either performed using rig tests or CFD analysis which are adequate for a small number of configurations. Considering preliminary design or parametric studies where generally many different configurations are treated, rig test and CFD analysis are too time consuming and expensive.

In preliminary design generally streamline curvature methods are used because of their speed. This method though is steady and axisymmetric and does not allow for computations of discrete tip injection configurations where the assumptions of an axisymmetric steady flow can't be applied anymore. Hence, a computation method has to be developed to account for discrete tip injection in a streamline curvature tool.

Due to discrete injection the inflow to the rotor downstream is changed thus that first the circumferentially and radially varying inflow conditions in the absolute frame of reference are developed. Because of the rotor speed the rotor experiences unsteady inflow conditions. As proposed by Melick [24] the unsteady part of the aerodynamics is mapped with altered inflow conditions. Using these altered inflow and steady aerodynamics the unsteady work input can be obtained. This approach is implemented into a computer program. Finally the results are compared to test data and it is found that the method works reasonable well.

## Kurzfassung

Diverse Untersuchungen ([32], [30], [4], [13],...) zeigten das Potential von Einblasung (einblasen von bereits komprimierter Luft in the Rotorspalt) im Hinblick auf das Betriebsverhalten von Axialverdichtern. Diskrete Einblasung (gleichmäßig am Umfang verteilte Einblasedüsen) stellte sich im Hinblick auf Betriebsbereichserweiterung als besser heraus, als Einblasung realisiert mittels einer den gesamten Umfang umspannenden Düse [27].

Diese Untersuchungen wurden mittels CFD Rechnung und Rig Tests durchgeführt. Für Vorauslegung und Parameterstudien, wo im allgemeinen viele verschiedene Konfigurationen untersucht werden, sind diese beiden Verfahren zu teuer und zeitaufwendig.

Stromlinienkrümmungsverfahren sind wesentlich schneller und werden deshalb in der Vorauslegung verwendet. Dieses Verfahren ist allerdings stationär und umfangssymmetrisch und kann deshalb nicht direkt zur Berechnung von diskreter Einblasung herangezogen werden. In dieser Arbeit wurde nun eine Berechnungsmethode entwickelt, die es erlaubt Einblasekonfigurationen mittels eines Stromlinienkrümmungsverfahrens zu berechnen.

Die Zuströmung zum Laufrad stromab der Einblasung wird durch die Einblasung verändert. Zuerst werden die geänderten Zuströmbedingungen im Absolutsystem erfasst. Durch die Drehbewegung des Rotors erfährt dieser eine instationäre Zuströmung. Laut Melick [24] kann man die Systemdynamik in den Zuströmbedingungen abbilden und mit dieser geänderten Zuströmung und einem stationären Strömungslöser die instationäre Arbeitszufuhr berechnen. Dieser Ansatz wurde in einem Computerprogramm implementiert. Mittels eines Vergleichs der Ergebnisse dieser Methodik mit Versuchsdaten wurde dann die Funktionalität des entwickelten Programms gezeigt.

# Contents

<b>1. Introduction and Background</b>	<b>1</b>
1.1. Compressor Characteristics . . . . .	2
1.1.1. Scaling Products . . . . .	2
1.1.2. Compressor Map . . . . .	4
1.1.3. Stage Characteristics . . . . .	5
1.2. Compressor Matching . . . . .	6
1.2.1. Axial Matching . . . . .	7
1.3. Tip Injection as Stability Enhancement . . . . .	9
1.3.1. Layout of a typical Tip Injection System . . . . .	9
1.3.2. Aerodynamic Effects of Tip Injection . . . . .	11
1.4. Research Questions and Outline . . . . .	15
<b>2. Numerical Method</b>	<b>18</b>
2.1. Streamline Curvature Method (SCM) . . . . .	18
2.2. Correlations . . . . .	21
2.3. SGV . . . . .	23
<b>3. Modelling of Tip Injection for SGV</b>	<b>27</b>
3.1. Inflow Conditions . . . . .	27
3.2. Unsteady Flow . . . . .	33
3.2.1. Relations between Isolated Airfoil and Blade Row . . . . .	34
3.2.2. Unsteady flow about airfoils . . . . .	38
3.3. Dynamic System . . . . .	40
3.3.1. Effective quantities . . . . .	41
3.3.2. Validation of the Dynamic System . . . . .	44
3.3.3. Summary . . . . .	49
3.4. Implementation . . . . .	50
<b>4. Results</b>	<b>66</b>
4.1. SGV Baseline Computation . . . . .	66

---

4.2. Computations with Tip Injection . . . . .	74
<b>5. Conclusions and Suggestions for Future Work</b>	<b>78</b>
<b>A. Injection.ein</b>	<b>87</b>
<b>B. Program Flow Chart 2</b>	<b>90</b>

# Nomenclature

## Latin Symbols

Symbol	Unit	Description
$a_{inj}$	$[-]$	ratio of the jet to the angular period (see equation 3.5)
$B$	$[-]$	Blockage (see equation 2.7)
$b_{inj}$	$[m]$	injection slot width (compare Figure 1.4)
$c$	$\left[\frac{m}{s}\right]$	flow velocity in the absolute frame of reference
$c_l$	$[-]$	lift coefficient
$c_b$	$[m]$	blade chord
$c_p$	$\left[\frac{J}{kgK}\right]$	specific heat capacity at constant pressure
$c_v$	$\left[\frac{J}{kgK}\right]$	specific heat capacity at constant volume
$h$	$\left[\frac{J}{kg}\right]$	enthalpy
$h_{inj}$	$[-]$	normed radial extension of the jet from the casing (compare Figure 3.1)
$i_r$	$[-]$	incidence range (see equation 2.6)
$L$	$[N]$	lift
$\bar{L}$	$\left[\frac{N}{m}\right]$	lift per span
$\dot{m}$	$\left[\frac{kg}{s}\right]$	mass flow
$\dot{m}_{red}$	$\left[\frac{kg\sqrt{K}}{s\cdot bar}\right]$	reduced mass flow (see equation 1.6)
$Ma$	$[-]$	Mach number
$n$	$\left[\frac{1}{min}\right]$	mechanical rotor speed
$n_n$	$[-]$	number of injectors (compare Figure 1.4)
$n_{red}$	$\left[\frac{1}{min\sqrt{K}}\right]$	reduced rotor speed (see equation 1.5)
$q$	$[Pa]$	dynamic head
$q$		arbitrary flow quantity
$p$	$[Pa]$	Pressure
$Re$	$[-]$	Reynolds number
$r$	$[-]$	normed radius

$r_{inj}$	$[-]$	normed inner radius of injection jets (compare Figure 3.1)
$s$	$[m]$	blade spacing
$T$	$[K]$	temperature
$u$	$\left[\frac{m}{s}\right]$	blade speed for blade rows
$u$	$\left[\frac{m}{s}\right]$	free stream velocity for isolated airfoils
$w$	$\left[\frac{m}{s}\right]$	flow velocity in the relative frame of reference
$w$	$\left[\frac{J}{kg}\right]$	specific work
$x_{inj}$	$[m]$	axial distance between injector and rotor leading edge (compare Figure 1.4)

## Greek Symbols

Symbol	Unit	Description
$\alpha$	$[^\circ]$	flow angle in the absolute frame of reference
$\beta$	$[^\circ]$	flow angle in the relative frame of reference
$\epsilon$	$[-]$	pressure rise coefficient (see equation 1.10)
$\eta$	$[-]$	efficiency
$\gamma$	$[-]$	ratio of specific heat capacities at constant pressure and volume $\frac{c_p}{c_v}$
$\nu$	$\left[\frac{m^2}{s}\right]$	kinematic viscosity
$\varphi$	$[-]$	flow coefficient (see equation 1.8)
$\varphi$	$[rad]$	angular coordinate
$\pi$	$[-]$	stagnation pressure ratio
$\psi$	$[-]$	temperature rise coefficient (see equation 1.9)
$\theta$	$[-]$	total temperature ratio
$\tau_M$	$[s]$	Melick time constant (see equation 3.38)
$\omega$	$[-]$	stagnation pressure loss coefficient (see equation 2.3)
$\omega_{red}$	$[-]$	reduced frequency (see equation 3.15)

## Subscripts

Subscript	
1	system inlet
2	system outlet
$ax$	axial direction
$eff$	effective flow quantity (see section 3.3)
$inj$	value inside the jet
$is$	isentropic process
$m$	meridional direction
$ms$	value inside the main flow
$q$	quasiorthogonal direction
$st$	stage
$t$	stagnation condition
$\theta$	circumferential direction

## Abbreviations

Abbrev.	
ACARE	Advisory Council of Aeronautic Research in Europe
ADP	Aerodynamic Design Point
FB	Fuel Burn
NEWAC	New Aero Engine Core Concepts
SCM	Streamline Curvature Method
SGV	Stromliniengeometrieverfahren (english: streamline geometry method)
SM	Surge Margin

# List of Figures

1.1. Sample Compressor Map . . . . .	4
1.2. Sample Stage Characteristic . . . . .	6
1.3. Compressor Matching . . . . .	7
1.4. Typical Tip Injection System Layout . . . . .	10
1.5. Stability Enhancement Results by Weigl . . . . .	11
1.6. Stability Enhancement Results by Suder . . . . .	12
1.7. Stability Enhancement of the first Stage by Hiller [13] . . . . .	13
1.8. Radial Profiles of Stagnation Temperature and Pressure for Tip Injection	14
1.9. Characteristics of the First Stage Casing Segment by Schneider [27] . .	15
2.1. System of Streamsurfaces proposed by Wu [31] . . . . .	19
2.2. Coordinate System for SCM Calculations [5] . . . . .	20
2.3. Typical Loss Characteristics . . . . .	22
2.4. SGV Flow Chart [2] . . . . .	24
3.1. Sections of Jet and Main flow presented in a View along the Axis . . .	28
3.2. Geometric Definitions of Correlation Parameters . . . . .	29
3.3. Comparison of Modelled and CFD Inflow Conditions . . . . .	31
3.4. Airfoil Cascade lift coefficient . . . . .	34
3.5. Relation of lift coefficient for Isolated Airfoil and Cascade [33] . . . . .	36
3.6. Lift of a Blade Row . . . . .	37
3.7. Dynamic System for one Segment . . . . .	39
3.8. (a) Unsteady Flow Model (b) Semi - Dynamic Model . . . . .	41
3.9. Dynamic System Response to the rectangular Signal for Tip Injection .	45
3.10. System Verification Data Set: (a) input $s_p$ ; (b) output $L$ . . . . .	47
3.11. System Verification . . . . .	49
3.12. View along the Compressor Axis on the Inlet Plane . . . . .	53
3.13. Prescription of the Radial Profile . . . . .	55
3.14. Radial Profiles computed by the Method . . . . .	58
3.15. Velocity Triangle . . . . .	59

---

4.1. Contour Correction . . . . .	67
4.2. Rotating Stall . . . . .	68
4.3. Rotating Stall Analogy . . . . .	69
4.4. Comparison of Mass and Area Averaging . . . . .	70
4.5. Quasi-Stage 1 Characteristics of SGV Baseline Compressor at 90% $n_{red}$	72
4.6. Overall Characteristics of SGV Baseline Compressor at 90% $n_{red}$ . . . . .	73
4.7. Radial Profiles of SGV and Test results with Tip Injection . . . . .	75
4.8. First Quasi-Stage Characteristics of Test and SGV results 90% $n_{red}$ . . . . .	76

# Chapter 1.

## Introduction and Background

It is well known that one of the main targets in aircraft engine development is to decrease specific fuel consumption (SFC). Predicted rising primary energy costs as well as concerns about environmental protection enforce this endeavor:

*Global air traffic is forecast to grow at an average annual rate of around 5% in the next 20 years. This high level of growth makes the need to address the environmental penalties of air traffic all the more urgent. To reduce CO<sub>2</sub> and NO<sub>x</sub> emissions new engine core configurations with heat management, active systems and advanced component technology will be developed under the EU integrated programme for NEWAC. [1]*

The "New Aero Engine Core Concepts" (NEWAC) programme was started to meet the goals regarding environmental protection set by the "Advisory Council of Aeronautic Research in Europe" (ACARE). Among other research topics, the so called "Tip Injection" was chosen as one of the research candidates [3]. Particularly for axial compressors tip injection can be used to enhance the operability. Enhanced operability in turn allows for more efficient compressor design sufficient operability without stability enhancement methods is often only achieved by trading part speed stability against ADP efficiency [5].

Radial Compressors are not treated in this work thus whenever it is referred to compressors axial compressors in aircraft engines are meant, even though some of the statements might also be applicable to other types.

In chapter 1 the background supporting the understanding of the work along with a presentation of a typical tip injection system and its impact on the compressor operating behaviour is presented. The numerical method used is then presented in chapter 2. In chapter 3 the tip injection computation method is developed and the implementation

into a computer program is explained. Results obtained using the tip injection computation method are presented in chapter 4 before conclusions on the implementation are drawn in chapter 5.

In Section 1.1 the axial compressor map with its parameters and limits is presented. Interaction of the single stages in the compressor, so called matching is then introduced in section 1.2 with emphasises part load stability, followed by tip injection with its impact on the compressor operating behavior in section 1.3. Finally the research questions and the thesis's outline are formulated in section 1.4.

## 1.1. Compressor Characteristics

Compressor Characteristics are used to present operating behavior. Tip injection is used to change the operation range of axial compressor. Hence, in order to present the effects on tip injection scaling products the compressor map and stage characteristics are introduced.

### 1.1.1. Scaling Products

In fluid dynamics usually dimensionless scaling products (e.g. Reynolds Number, Mach Number,..) are used. The set of parameters used here to quantify compressor's operating behavior is comprised of the Reynolds number, stagnation pressure rise coefficient, isentropic efficiency, reduced rotor speed and reduced mass flow. In general these scaling products can be used for arbitrary compression systems, but if not stated explicitly they are used for the overall compressor. The fundamental relation between the scaling products discussed in the following is given by

$$\pi = f(\dot{m}_{red}, n_{red}, Re, \eta_{is}) \quad (1.1)$$

- The *Reynolds Number* gives the ratio of dynamic terms to viscous terms in the Navier Stokes equations and is defined by

$$Re = \frac{Lu}{\nu} \quad (1.2)$$

where  $L$  is a characteristic length,  $u$  is a characteristic velocity and  $\nu$  is the kinematic viscosity.

- The *Stagnation Pressure ratio* is defined by

$$\pi = \frac{p_{t,2}}{p_{t,1}} \quad (1.3)$$

where  $p_{t,2}$  and  $p_{t,1}$  are stagnation pressure at system outlet and inlet respectively.

- *Isentropic efficiency:* Compressor efficiency is basically defined as the ratio of work into the ideal compressor to the work into the actual compressor. The isentropic efficiency defined by

$$\eta_{is} = \frac{\frac{p_{t,2}(\gamma-1)/\gamma}{p_{t,1}} - 1}{\frac{T_{t,2}}{T_{t,1}} - 1} \quad (1.4)$$

is the ratio of isentropic work at given pressure rise (ideal) to the actual work. In this equation  $p$  and  $T$  are pressure and temperature at system outlet (2) and inlet (1) respectively.  $\gamma$  is the ratio of specific heat capacities at constant pressure and volume  $c_p/c_v$ .

- *Reduced speed:* The loading of blades and therefore the pressure rise through the compressor depends on the speed of the rotor. To characterize this, commonly the Mach number obtained with blade speed at rotor tip is used. Commonly this Mach number is based on the speed of sound evaluated with the inlet stagnation temperature  $T_{t,in}$  and is defined by  $\sqrt{\gamma RT_{t,1}}$ , where  $R$  is the specific gas constant.  $\gamma$  and  $R$  are assumed to be constants. Therefore the tip Mach number can be simplified to  $u/\sqrt{T_{t,1}}$ , with  $u$  being the tip speed defined by  $u = 2r_{tip}\pi n$ .  $r_{tip}$  is the rotor tip radius and  $n$  is the rotor mechanical speed. For one machine tip radius is constant thus this ratio yields to the commonly used reduced speed:

$$n_{red} = \frac{n}{\sqrt{T_{t,1}}}. \quad (1.5)$$

- *Reduced mass flow:* The same considerations done for the tip Mach number, can also be applied to the axial Mach number [6]. The axial flow velocity gives a measure for the incidence, i.e. the difference of actual flow angle to blade angle. The blade loading and therefore the pressure rise, depend on the incidence. Under the same conditions used for the simplification of the reduced speed, the reduced mass flow can be derived ([6] p.809):

$$\dot{m}_{red} = \frac{\dot{m}\sqrt{T_{t,1}}}{p_{t,1}} \quad (1.6)$$

where  $\dot{m}$  is the actual mass flow through the compressor,  $T_{t,1}$  and  $p_{t,1}$  being stagnation temperature and stagnation pressure at system inlet.

### 1.1.2. Compressor Map

The usual way to present the performance of a compressor is the compressor map. The stagnation pressure rise  $\pi$  is plotted versus the reduced mass flow  $\dot{m}_{red}$  at compressor inlet. Using this representation the compressor map is independent of inlet conditions.

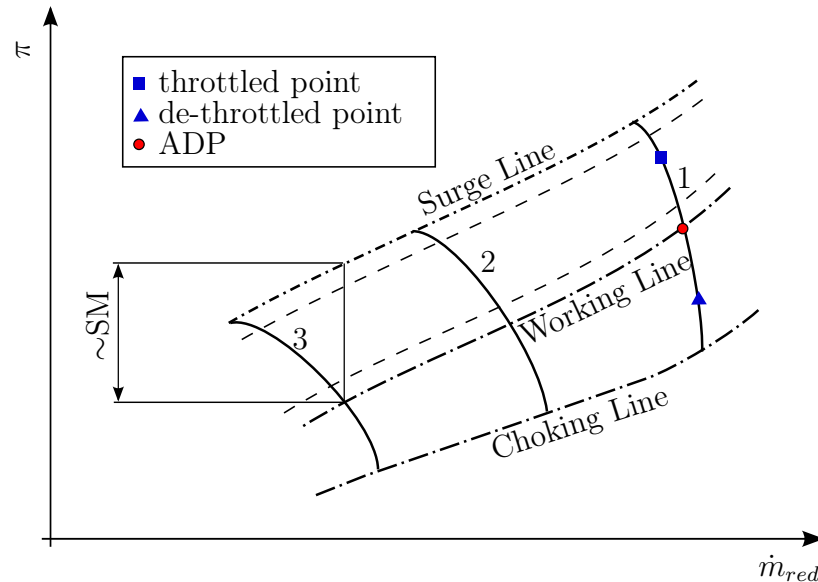


Figure 1.1.: Sample Compressor Map

The solid lines 1,2,3 in Figure 1.1 are called *speed lines* or *throttling lines* and are lines of constant reduced rotor speed. Speed lines are often labeled as percentage of reduced "Aerodynamic Design Point" (ADP) rotor speed, meaning that curve 1 in Figure 1.1 is also referred to as 100% speed line. At the ADP compressor geometry is designed to comply with the required pressure rise ratio and mass flow at maximum achievable efficiency.

Decreasing the static outlet pressure at constant reduced rotor speed yields a higher reduced mass flow through the compressor up to the point where the Mach number reaches unity at the blade's throat and the compressor is "choked". Such states are referred to as "de-throttled".

During throttling at constant reduced rotor speed (i.e. raising the static pressure at compressor outlet) the reduced mass flow through the compressor decreases. Further throttling yields a particular point, where compressor maximum stagnation pressure rise is reached. For points at higher stagnation pressures stability is not given anymore as pointed out by Cumpsty ([5], chapter 9) and surge will arise. However, this operating point must not be exceeded and is called "surge point". According to Greitzer et. al.

[10] surge occurs if the compressor isn't able to provide the required static pressure rise. This criteria is used in this work to determine the surge point.

For each speed line a working point exists, which is a steady operation point fixed by the turbine inlet mass flow. For the 100% speed line this point is the ADP. The working line points of all speed lines give a curve themselves and it is called working line (WL). The surge line (SL) in contrast is composed by the surge points of the speed lines. Those two lines are important, because they show the margin of the calculated steady compressor operation to instability. The *surge margin* (SM, i.e. the distance of the working point to the surge point) is defined in different ways, looking at different references. A simple but common way to define it [5] is

$$SM = \frac{\pi_{SL} - \pi_{WL}}{\pi_{WL}}, \quad (1.7)$$

where  $\pi_{SL}$  and  $\pi_{WL}$  are the stagnation pressure ratios at surge line and working line for the same corrected mass flow, like presented in Figure 1.1.

In operation e.g. inlet distortions, abrasion, transient engine operation lead to a shift of these lines, indicated by the two dashed lines parallel to them. Thus the surge margin is reduced and sufficient surge margin has to be provided by design to account for this. Otherwise the compressor wouldn't be operable.

### 1.1.3. Stage Characteristics

Instead of the scaling products introduced in section 1.1.1 for stage characteristics different ones are used [5]. The flow coefficient, defined by the ratio of axial velocity  $c_{ax}$  to the blade speed  $u$

$$\varphi = \frac{c_{ax}}{u} \quad (1.8)$$

is related to the corrected mass flow derived for the overall compressor and as shown in [5] those two quantities are directly proportional. The advantage of  $\varphi$  is that it is directly proportional to the incidence in contrast to  $\dot{m}_{red}$  where this statement is just true along lines of constant reduced rotor speed.

The work input as presented in [5] is defined as:

$$\psi = \frac{\Delta h_t}{u^2/2} \quad (1.9)$$

where  $\Delta h_t$  is the stage stagnation enthalpy rise. The stage stagnation pressure ratio scaled with the kinetic blade energy (typically at tip) is the third scaling product used

with stage characteristics and is defined by [13]

$$\epsilon = \frac{c_p T_{t1} \left[ \left( \frac{p_{t2}}{p_{t1}} \right)^{\frac{\gamma-1}{\gamma}} - 1 \right]}{u^2/2}. \quad (1.10)$$

The ratio of  $\epsilon$  and  $\psi$  is the isentropic efficiency of the stage:

$$\eta_{is,st} = \epsilon/\psi \quad (1.11)$$

In Fig. 1.2 a sample stage characteristic is presented.  $\psi$  and  $\epsilon$  are plotted versus  $\varphi$ .

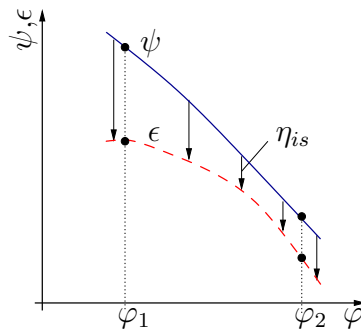


Figure 1.2.: Sample Stage Characteristic

Higher  $\varphi$  implies higher axial velocity and thus lower stage loading and stagnation pressure rise. Hence  $\varphi$  is higher for de-throttled states ( $\varphi_2$ ) than for the throttled states ( $\varphi_1$ ). The  $\epsilon$ -curve is computed from the isentropic temperature difference that occurs for the actual stagnation pressure rise, whereas the  $\psi$ -curve is obtained from the actual stagnation temperature difference, thus the difference of these two curves is proportional to the losses. At  $\varphi_1$  the stage is highly throttled and further throttling would decrease the stagnation pressure rise of the stage, giving a positive slope of the  $\epsilon$ -curve. This occurs because the stage losses rise disproportionate to the work. The compressor behavior for such states is further discussed in section 1.2.

## 1.2. Compressor Matching

Compressors in aero engines are commonly composed of several stages. The interaction of the stages is called stage matching or axial matching, opposed to radial matching which is concerned with the radial work distribution in a single compressor stage [6]. This section only gives a short overview over the compressor matching and a more detailed description can be found in [5].

### 1.2.1. Axial Matching

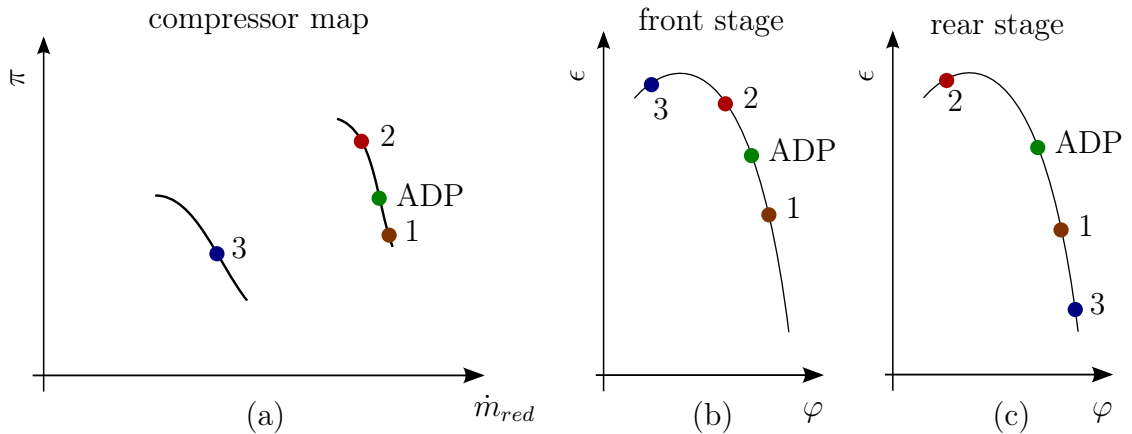


Figure 1.3.: (a) Overall Pressure ratio - Corrected Mass Flow Characteristics; (b) Front Stage Characteristics; (c) Rear Stage Characteristics

In Figure 1.3 a compressor map along with characteristics of the front and rear stage are shown. At ADP condition at which the compressor was designed all stages are at a similar throttled state. Annulus cross-sectional areas of the compressor are obtained at ADP conditions to accommodate the design mass flow rate. These areas remain constant for every operating point, but at off design different mass flow rates pass through the compressor and blade speed may change. As pointed out earlier blade loading and therefore the operating point of stages can be related to the flow coefficient, which only depends on the volume flow rate and rotor speed. Volume flow rate itself is linked to the mass flow rate by density.

Point 2 represents a throttled condition of the compressor at same rotor speed, thus the mass flow rate is smaller resulting in a higher overall pressure rise ratio. Rotor speed and thus blade speed are the same as of ADP. Hence only the change in volume flow rate alters the throttling state of the single stages. Assuming same inlet conditions at compressor entry, volume flow rate scales with mass flow rate and thus the first stage generates higher pressure rise. Higher pressure at stage exit yields higher density and because of continuity the volume rate is even more decreased into stage 2. This effect amplifies through the compressor and generally the last stages are higher throttled than the front ones. Hence, rear stages are more crucial for blade stalling than the front ones.

The compressor is in a de-throttled state with respect to ADP at point 1 and the same reasoning done for point 2 can be applied yielding opposed results. In this case not blade stall, but choke (i.e. Mach number = 1 in the throat) of one of the rear blade

rows is the operation limit.

The points concerned so far had same rotor speed. The change due to different rotor speed is illustrated with point 3. Reduced rotor speed yields lower pressure and temperature rise within a stage. Also the density rise decreases and because of the continuity equation, the axial flow velocity ratio of stage outlet to stage inlet  $\frac{c_{ax2}}{c_{ax1}}$  increases with respect to the ADP. Axial velocity at stage inlet is used to compute the flow coefficient thus the same statement is true for them. This implies that  $\varphi$  is generally higher for rear stages than for front stages, thus front stages are more throttled than the rear ones. At lower part speeds stages further aft are commonly choked thus the mass flow is limited and the axial velocity in the front stages is further decreased. Hence, at part speed, front stages tend to stall, whereas rear stages tend to choke. If stall occurs in a row the stage pressure rise decreases (positive slope in stage characteristics) and other stages have to take over otherwise the static pressure at outlet would decrease which would lead to surge as discussed earlier. In order to improve compressor stability blade stall has to be delayed.

Several stability enhancement methods have been developed to prevent blade stall [5].

- *Bleed*: At part speed the flow through rear stages might get choked, which throttles the front stages even more. Bleeds are used to decrease the mass flow through the rear part of the compressor and higher mass flow can pass through the front stages. Except for customer bleeds where this mass is used for other system devices this mass flow can't be used and thus a drop in engine efficiency occurs.
- *VGV's*: Variable guide vanes can be used to change the inflow conditions to the rotors such that blade load is decreased. The mechanism that drives these guide vanes though adds additional weight to the engine and thus leads to higher fuel burn (FB).
- *Change of compressor design*: Ideally the compressor design is performed in a way that the efficiency, particularly at ADP, is best. Changing some design parameters though enhances compressor stability. A commonly used option is to change incidence at ADP. To get best efficiency at design the incidence needs to be set such that blade losses are smallest (minimum loss incidence). As discussed earlier at part speed front stages tend to stall whereas rear stages tend to choke. Changing the blade angles in a way that incidence for the front stages is decreased and increased for the rear stages the margin of the stages to their critical points is increased. This yields higher stability but on the other hand efficiency is

decreased.

- *Casing Treatment (CT)*: To get recirculation that stabilize the rotor in the tip section the casing is modified. This method was implemented in recent engines at MTU but a drop in efficiency is observed. Casing treatment is a permanent modification of the geometry. Therefore, also at ADP the flow is change which generally leads to recirculation decreasing efficiency [13]

Above methods all improve compressor stability but FB is raised. Tip injection introduced in the next section can be switched on if stability issues arise at particular operating points thus the increased FB is limited to these cases. At design conditions where the engines operates most of the time it can be switched off and FB is not changed.

## 1.3. Tip Injection as Stability Enhancement

### 1.3.1. Layout of a typical Tip Injection System

Tip injection is a system where air is injected from the casing in order to stabilize the rotor. Particularly for tip critical rotors (i.e. stall is incepted at the tip first) this method can be used to delay blade row stall. In order to inject air into the compressor an air reservoir with a higher stagnation pressure compared to the stagnation pressure upstream of the blade row is required. To provide the required air in experiments often an external compressor is used that allows for adjustment of the injection parameters ( $p_t, \dots$ ). For application of tip injection to an engine air that is already compressed is used as reservoir. If an interstage bleed is available this can be used as source for the injection system [29] otherwise an additional bleed would necessary. No matter which type of source is used the air is brought through a piping system to the compressor at the location where the injection system is to be placed. There the air is accelerated using a nozzle and then injected into the annulus.

In Figure 1.4 the tip injection system used for this work is presented. This setup is used for example in [30] and [13]. Subfigure (a) shows a meridional cross-section at a circumferential position through a injection jet. Discrete slots are located a certain distance  $x_{inj}$  upstream of the rotor blade row. The injection jet is inclined to the horizontal plane at  $\gamma_{inj}$ . Due to the Coanda-effect it changes its direction immediately at the location of entrance to be aligned with the casing.

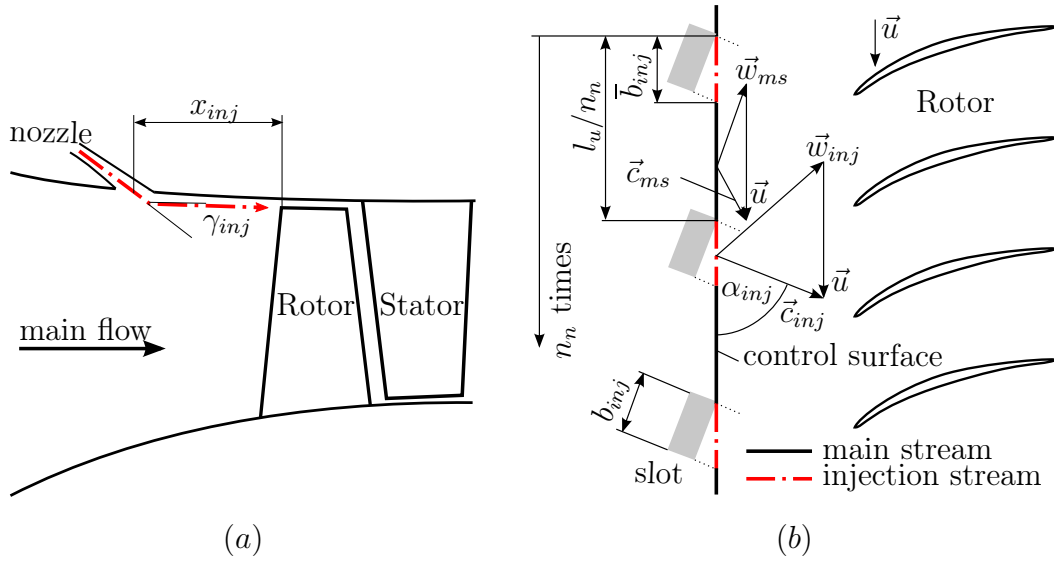


Figure 1.4.: Typical Tip Injection System Layout (a) Cross-Section through the Injection Jet, (b) Circumferential Plane

Figure 1.4 (b) shows a circumferential plane close to rotor tip, which is affected by tip injection. The rotor blade row, located at right hand side of the figure, is turning in the downward direction denoted by blade speed  $u$ . The vertical line left to the blade row represents a control surface. It is located immediately downstream of the injection slots. At this control surface the inlet flow quantities to the compressor are treated following under the assumption that no mixture of jet and main flow takes place up to this point. Flow approaching from the injection nozzles passes through the control surface's dash-dotted sections. Solid lines represent sections where main stream flow is streaming through.  $n_n$  nozzles are equally distributed around the circumference, thus  $n_n$  sections of either flow section exist. With the circumference at the tip defined by  $l_u = 2r_{tip}\pi$ , the length of one periodic unit is thus  $l_u/n_n$ . The width of the nozzle is denoted by  $b_{inj}$ .  $\bar{b}_{inj}$  is the circumferential extension of the jet at the control surface. The nozzles are inclined by the angle  $\alpha_{inj}$  in this plane with respect to the circumferential direction and  $\vec{c}_{inj}$  is the injection jet velocity. Using the velocity triangles the relative flow velocity vectors are obtained.  $\vec{w}_{ms}$  and  $\vec{w}_{inj}$  are the relative flow velocity vectors representing the flow in main and injection stream respectively representing the desired incidence decrease.

### 1.3.2. Aerodynamic Effects of Tip Injection

First research on tip injection (also called air injection) was performed about half a century ago [25]. In the late 90's Weigl et. al. [32] applied discrete tip injection to a single stage axial compressor. The results found are presented in Figure 1.5. A signif-

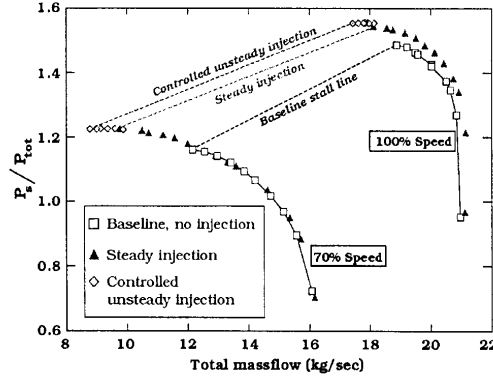


Figure 1.5.: Stability enhancement obtained by Weigl [32]

icant increase in stable operating range was observed using tip injection. Controlled unsteady injection was found to be superior to constant mass flow (Steady Injection). However, controlled unsteady injection adds additional weight to the engine and the benefit unsteady injection has with respect to steady injection is not significant. More recent investigations therefore just considered steady injection. Hence, in this work also only steady injection is treated.

Suder et. al. [30] obtained numerical and experimental results for various tip injection configurations. Suder defined range extension as

$$\Delta\phi_{stall} = \frac{\phi_{stall,b} - \phi_{stall}}{\phi_{stall,b}} \quad (1.12)$$

where  $\phi_{stall,b}$  and  $\phi_{stall}$  are the flow coefficients at stall for the baseline and injection setup respectively. The results are presented in Figure 1.6 (a) and (b). In Figure 1.6 (a) range extension is plotted versus the ratio of injected mass flow to annulus mass flow for various number of slots and their arrangement along the annulus. It was found that range extension was influenced by the ratio of  $b_{inj}$  to  $l_u/n_n$  (i.e number of slots) up to a certain number of slots but not by the circumferential arrangement of the slots. In Figure 1.6 (b) the correlation of the range extension with the mass averaged axial velocity of the outer 6% annulus (i.e. radial extent of injection) is presented. It was found that range extension depended considerably on the injector exit velocity. Maximum range extension was attained when the injectors were choked (i.e the axial

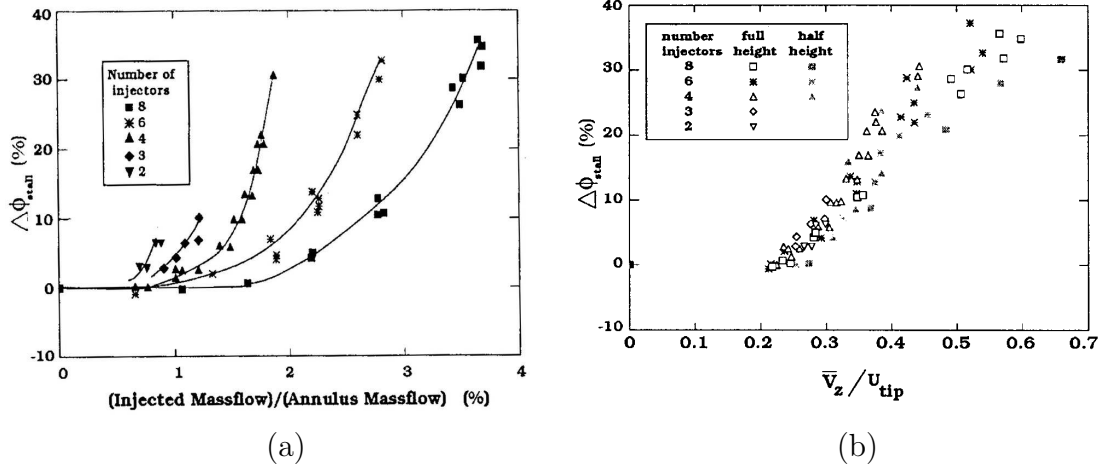


Figure 1.6.: Range extension obtained by Suder [30]: (a) Range extension versus number of injectors; (b) Range extension as a function of mass averaged axial velocity at the outer 6% annulus

velocity is at its maximum). Finally they compared tip injection test runs with VGVs not closed (setup 1) to investigations without tip injection but closed VGVs (setup 2). It was shown that setup 1 achieved the same operation range as setup 2. Hence, in compressors primarily operating at nominal speed VGVs can be replaced by a tip injection system. This is another application for tip injection.

Cassina et. al. [4] performed a parameter study on tip injection using CFD. The effects of tip injection design parameters depicted in following list on the operation range extension  $\Delta\phi_{stall}$  were tested. During every single study one parameter was changed whereas the others remained constant.

- *injected mass flow*: increasing the injected mass flow increased  $\Delta\phi_{stall}$
- *injector aspect ratio*: The slots aspect ratio influences the ratio  $\frac{\bar{b}_{inj}}{l_u}$  (i.e. the circumferential ratio of jet and main-flow segments). It was shown that for this compressor a particular aspect ratio (55.3%) yielded highest stability improvement. The injector throat area was the same for all set-ups yielding the same injector exit velocity.
- *injection angle*: an optimum angle could be found for which  $\Delta\phi_{stall}$  increased most
- *axial gap  $x_{inj}$* : If the injectors are positioned far upstream no difference was obtained. For smaller distances ( $x_{inj}/\text{rotor chord}=0.5$ ) the improvement was less but altogether it was concluded that the influence of the axial gap was minor.

Hiller et. al. [13] carried out tip injection investigations on a multistage compressor. The compressor used in this paper is similar to the one used for verification of computations in this work, thus it is discussed thoroughly, because similar trends are expected. Detailed information on radial work distribution as well as radial matching were obtained. It was found that the reduction in reduced inlet mass flow was less than reduced injected mass flow added for the same throttling condition. Hence, the compressor delivered higher reduced mass flow to the combustion chamber. Results found by earlier works regarding operation range extension could be confirmed. For reduced injected mass flows higher than a certain value, tip injection yields considerable increase of the operation range. Further it was concluded that above a certain mass flow no further increase would be obtained anymore.

The test rig setup allowed for closing half of the nozzles, yielding halved throat area. Using only half the nozzles at same mass flow increased the axial exit velocity, giving the possibility to test that axial velocity correlated with range extension proposed by Suder which was confirmed. When the mass flow through the nozzles got choked the operation range could be extended by increasing the mass flow even though the effect declined. Once the flow was choked the exit axial velocity didn't increase anymore, thus the further enhancement was purely due to higher injected mass flow. Hence, it was concluded that the effect of increased mass flow on operation range extension was less important compared to axial exit velocity. This observation complied with the results obtained by Suder.

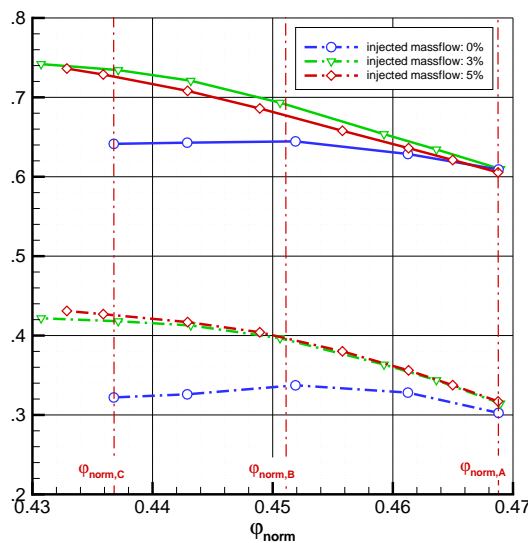


Figure 1.7.: Stability Enhancement of the first Stage by Hiller [13]

Characteristics of the first stage extracted from [13] are shown in Figure 1.7. Looking at the  $\epsilon$  characteristics one can see that the baseline test (i.e. injected mass flow: 0% denoted by circles) already has a positive slope for  $\varphi$ 's smaller than 0.452. Test data suggested that rotating stall occurred for the positive slope characteristics section. The injection test cases still showed negative slopes thus the stable operating range was extended. Moreover, characteristics of injection test were steeper than baseline test characteristics.

Radial profiles of stagnation temperature and stagnation pressure were measured and are presented in Figure 1.8. Measurements obtained from setups using tip injection

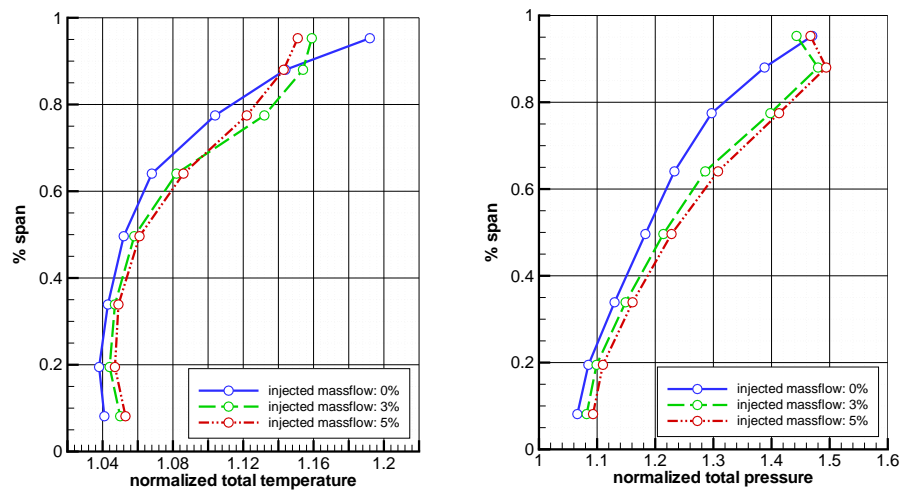


Figure 1.8.: Radial Profiles of Stagnation Temperature and Stagnation Pressure for Tip Injection [13]

showed lower stagnation pressure and stagnation temperature at rotor tip compared to cases without injection, like expected because of the smaller incidence at rotor tip. Test cases compared had similar flow coefficients at first rotor, thus the mean of the axial velocity had to be similar. Because the axial velocity is increased at rotor tip for the rest of the annulus it has to be smaller yielding higher incidence. Hence, the work input at the radial section not affected by tip injection was increased.

Schneider [27] executed comparable work to Hiller for a different compressor, to explore the effect of a different compressor geometry. His work was carried out using CFD rather than rig tests. The result obtained confirmed the work by Hiller. Further comparison between discrete injection slots equally distributed around the circumference to a continuous slot around the whole circumference was made. Injected mass flow for both injection setups was held constant. In order to see the effect of tip injection on

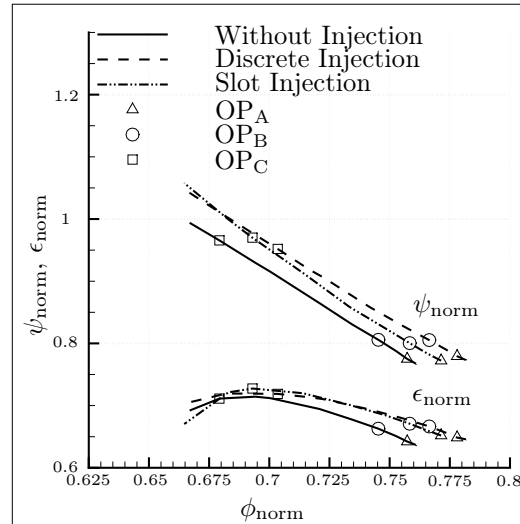


Figure 1.9.: Characteristics of the First Stage Casing Segment by Schneider [27]

radial segments stage characteristics for three radial segments were investigated. The results for the casing segment are presented in Figure 1.9 normed with the ADP. Three compressor operating points ( $OP_A$ ,  $OP_B$  and  $OP_C$ ) are indicated at the characteristics for CFD computations without injection, with discrete injection and an injection slot. All three setups stalled almost at the same flow coefficient. The increase in operating stability is due to the shift of the curves. Considering  $OP_B$  (working line operating point) it is obvious that the point is shifted to higher flow coefficients for the injection cases where the shift is greatest for discrete injection. Similar statements can be made for the throttled operating points  $OP_C$  for the different setups. The compressor without tip injection almost surged at  $OP_C$ , whereas there was still some throttling capability for discrete injection. Tip injection realized with one continuous slot showed a gain in throttling capability compared to the case without injection, but not as much as discrete tip injection. Hence, discrete injection was found to be superior to slot injection. It was concluded that this might be due to unsteady effects.

## 1.4. Research Questions and Outline

Various studies performed with tip injection showed its positive effect in terms of stability enhancement particularly at part speed. In section 1.2 typically used methods for stability enhancement were briefly discussed. In contrast to most of them the drop in efficiency for tip injection at ADP is negligible because it can be shut off. Particularly for compressors working mainly at ADP condition this seems to be an interesting alternative. Replacing one of the used methods by a tip injection system

might increase the compressor ADP efficiency. To find out which method would give best results seems to be one of the next logic step in research. Furthermore it is to be investigated how a redesign of the engine compressor utilizing the strengths of tip injection could be used to increase efficiency and the effectiveness of the tip injection system. Considering the tip injection system it has to be found which combination of parameters gives the best performance for the particular compressor. Up to now little is known about how such a changed design could look like and a parameter study would clarify this.

Most studies on tip injection were performed doing rig tests or CFD computations. A complete parameter study though would require many different setup and for each setup a complete compressor map has to be generated. Obtaining these results from rig tests is time consuming and expensive and today CFD computations are too time consuming. Hence, such studies would ask for fast, but still reasonable accurate methods to obtain a "best" setup which than can be optimized using CFD and validated by rig tests.

At MTU preliminary design is performed with a streamline curvature tool (for more details see chapter 2). Streamline curvature computations are 2-dimensional and steady by nature. In order to facilitate pre design computations taking tip injection into account, a different approach has to be developed to run computations for tip injection which are 3-dimensional and unsteady.

The major points regarding such a correlation are as follows:

- *Correlation Theory*: Discrete Tip injection was found to be superior to a continuous slot (compare section 1.3) in terms of operation range extension. A rotor passing a discrete slot injection configuration experiences varying inlet conditions. It is known [7] that airfoils have an increased stalling angle if the inlet flow angle is oscillating rather than being constant. Hence, it has to be tested if the correlation has to account for the system dynamics and if so the parameters of such a method have to be identified.
- *Implementation of the correlation*: Once the theory is developed it has to be realized. First the procedure has to be developed and then a robust program has to be generated.
- *Validation*: Finally the correlation has to be applied to the test compressor and thus it can be verified that the expected trends are reproduced.

To validate the computation method for tip injection rig test data is available. The rig test data contains all required data for the overall characteristics as well stator leading

edge instrumentation (stagnation pressure and stagnation temperature). This data is available for both baseline (without injection) and tip injection tests. The injection slots are upstream of the first stage, so the leading edge probes of the first stage stator are of particular interest. A streamline curvature computation for the baseline setup has to be performed meeting the measured baseline rig test.

# Chapter 2.

## Numerical Method

SGV (german: Stromliniengeometrie Verfahren, english: streamline geometry method), a streamline curvature based program is extended for tip injection computations. In order to explain the developed method for tip injection later in this chapter the SGV program is introduced. In section 2.1 the basic numerical procedure, the streamline curvature method is briefly discussed. Correlations that are required to adapt the inviscid streamline curvature method to the actual flow field in the compressor passage are covered in section 2.2. Finally the flow chart of SGV is presented in section 2.3, showing the functionality of the SGV program.

### 2.1. Streamline Curvature Method (SCM)

#### Background

Streamline curvature methods (SCM) are widely used methods for pre estimates of flow through compressors as described by e.g. Cumpsty ([5], chapter 3). In order to give an understanding of the scope and limitations here the main aspects are presented. The full derivations of the method can be found in [5].

The flow through an axial compressor passage is inherently 3 dimensional. Today solutions to this problem, can be obtained using computational fluid dynamics (CFD). In preliminary design where the focus is on the speed of the methods CFD generally is too slow.

Wu [31] was the first who treated the flow on interrelated, intersecting streamsurfaces, rather than the fully three-dimensional flow. Streamsurfaces are categorized in two groups. They are defined by their domain entrance lines. One group, so called S1

surfaces, are composed by the streamlines passing through the circumference at particular radial positions. S2 surfaces, framed by streamlines going through one meridional

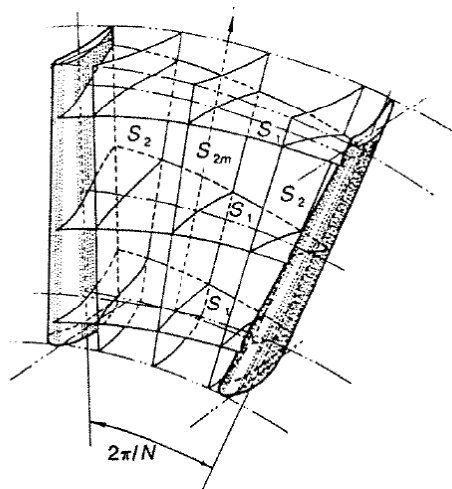


Figure 2.1.: System of Streamsurfaces proposed by Wu [31]

plane at blade row entrance are the second type of streamsurfaces. This model is shown in Figure 2.1. Since bounded by streamlines streamsurfaces are a result of computations and change with the flow. Therefore, the streamsurfaces shape isn't known in advance since planes at which the calculations are carried out change with every solution step. Using S1 and S2 surfaces thus yields an iterative solution procedure. In order to avoid this, meridional planes are used instead of S2 surfaces. S1 surfaces are replaced by surfaces of revolution built from streamlines laying in the meridional plane for the same reason. S1 computation results are not part of the streamline curvature method, but have to be provided by an external tool. This aspect is discussed in sections 2.2 and 2.3.

## Coordinate System

Before the SCM is derived the coordinate system is defined and described. In Figure 2.2 the coordinate systems are presented in a meridional view (a) and a view along the compressor axis (b). The  $r-x-\theta$  coordinate system is the widely used cylindrical coordinate system where  $r, \theta$  and  $x$  are radial, circumferential and axial direction respectively. Points A-B-C are on a streamline which lies in the mean hub-casing streamsurface (i.e. streamsurface from hub to casing that splits the channel between two adjacent blades in two circumferential equal sections). In the meridional view  $m$  and  $n$  axis are presented being tangential and perpendicular to the streamline. Streamline shape and position and thus its tangent and perpendicular direction are a result of the computation. In

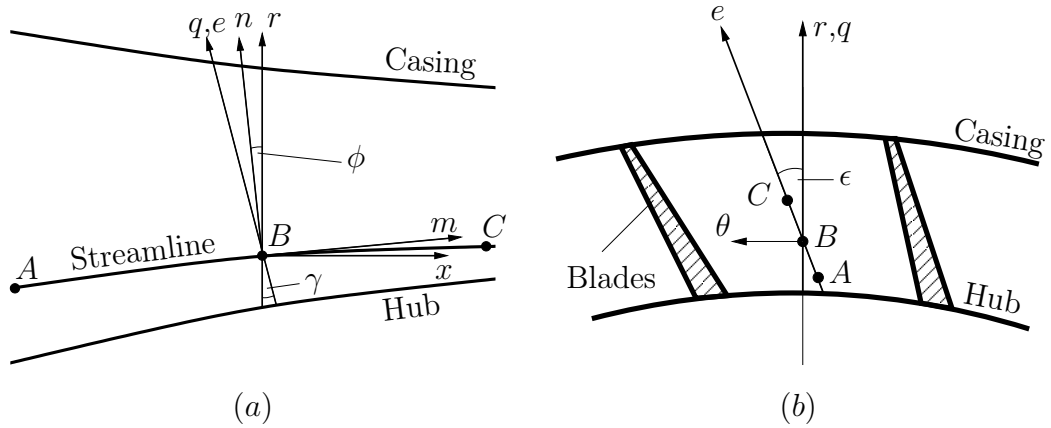


Figure 2.2.: Coordinate System for SCM Calculations [5]

order to formulate the equations on a coordinate system that is known in advance a so called quasi orthogonal direction  $e$  is chosen roughly perpendicular to the streamline and held constant for the computation. The projection of  $e$  onto the meridional plane is the unit vector  $q$ . In the meridional plane  $\phi$  is the angle of the  $n$ - $m$  coordinate system to the  $r$ - $x$  coordinate system and  $\gamma$  is the angle between the radial and quasiorthogonal direction.  $\epsilon$  is the inclination of the unit  $e$  vector to meridional plane about the axis.

### SCM Numerical Procedure

The derivation of the SCM is performed by simplifying the

- Continuity Equation, the
- Momentum Equations and the
- Energy Equation

using following assumptions

- steady flow
- axisymmetric flow
- inviscid flow
- adiabatic flow

The derivation of the basic SCM equation is presented for example in [5] (derivation emphasising physical basis) and in [28] (starting from continuity, Navier Stokes and energy equation). This yields to the full radial equilibrium or streamline curvature

equation defined by:

$$\begin{aligned} \frac{1}{2} \frac{\partial}{\partial q} v_m^2 &= \frac{\partial h_t}{\partial q} - T \frac{\partial s}{\partial q} + v_m \frac{\partial v_m}{\partial m} \sin(\phi + \gamma) + \frac{v_m^2}{r_m} \cos(\phi + \gamma) \\ &\quad - \frac{1}{2r^2} \frac{\partial}{\partial q} (r^2 v_\theta^2) + \frac{v_m}{r} \frac{\partial}{\partial m} (rv_\theta) \tan(\epsilon) \end{aligned} \quad (2.1)$$

This equation has to be solved iteratively. The solution gives the gradient of the meridional velocity  $v_m$  along the quasiorthogonal direction but since the level is not defined, it is obtained by solving the continuity equation:

$$\frac{\partial \dot{m}}{\partial q} = \rho v_m \cos(\phi + \gamma) 2\pi r. \quad (2.2)$$

## 2.2. Correlations

The SCM was derived using several assumptions. In order to represent reality in a better way correlations are used.

### Loss and Deviation correlation

One of the main assumptions of the SCM is that it is inviscid, meaning that losses is not accounted for. Losses are included into SGV by the use of loss correlations to correct the flow quantities in streamwise direction. Correlations used in SGV are based upon Grieb et. al. [11].

Stagnation pressure loss coefficient, defined by

$$\omega = \frac{\Delta p_t}{q} \quad (2.3)$$

where  $\Delta p_t$  is the stagnation pressure loss and  $q$  is the dynamic head, is used to quantify losses. For a blade row the stagnation loss, given by [11]

$$\omega = \left( \underbrace{\omega_{P,inc} + \omega_{P,co}}_1 + \underbrace{\omega_W}_2 \right) \left( \frac{Re}{Re_{ref}} \right)^{-0.2} + \left( \underbrace{\omega_{SEC}}_3 + \underbrace{\omega_t}_4 \right) \left( \frac{Re}{Re_{ref}} \right)^{-\epsilon} + \underbrace{\omega_{ss}}_1 \quad (2.4)$$

can be decomposed according to the mechanism it is generated by. Following losses is accounted for:

1. *Profile loss*: account for the losses caused by the profiles boundary layers and is composed by:  $\omega_P = \omega_{P,inc} + \omega_{P,co} + \omega_{ss}$ , where:

- *incompressible profile loss*  $\omega_{P,inc}$ : is obtained from cascade measurements according to a formula based on Lieblein [19] at design incidence.
  - *compressible profile loss*  $\omega_{P,co} = K_{co}\omega_{P,inc}$ :  $K_{co}$  depends on the Mach number at blade row outlet.
  - *shock loss*  $\omega_{ss}$ : is derived from an empiric correlation based on measurements.
2. *Wall friction*  $\omega_W$ : takes into account the boundary layers at hub and casing.
  3. *Secondary loss*  $\omega_{SEC}$ : accounts for the end wall losses at blade root and tip.
  4. *Tip clearance loss*  $\omega_t$

All loss contributions, except shock losses, are evaluated at Reynolds number  $Re_{ref} = 3 \times 10^5$ . For different Reynolds numbers these values are corrected by exponential laws on the Reynolds number fractions in equation 2.4. Assuming that the similarity law for hydraulic smooth surfaces is valid for profile and wall friction losses the exponent 0.2 is used. The Reynolds correction exponent  $\epsilon$  for tip clearance and secondary losses is obtained from compressor tests.

In terms of profile losses so far only losses for minimum loss incidence  $inc_{min}$  have been considered. The relative inflow angle at this incidence is referred to as  $\beta_{1,min}$ . At

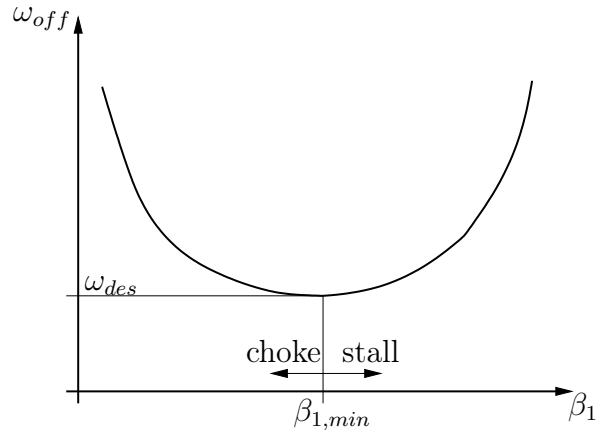


Figure 2.3.: Typical Loss Characteristics

incidences different to  $inc_{min}$  higher losses are generated by the profile. This effect is represented by so called loss characteristics. A typical loss characteristic is presented in Figure 2.3. It is depicted with an exponential law defined as

$$\omega_{off} = \omega_{des} (1 + K i_r^n) \quad (2.5)$$

with the so called incidence range defined by [17]

$$i_r = \frac{inc - inc_{min}}{inc_{max} - inc_{min}}. \quad (2.6)$$

$inc$  in equation 2.6 is the the incidence at which the off-design losses are desired and  $inc_{max}$  is correlated to fit the characteristic to test data.  $K$  and  $n$  are constants obtained by Köhler [17]. Depending on whether the actual incidence is smaller or bigger than the minimum loss incidence  $K$ ,  $n$  and  $inc_{max}$  take different values (choke and stall side of the characteristics).

In reality the exit flow angle is not equivalent to the blade exit angle. In order to account for this deviation a correlation based on Lieblein [20] is used. The structure of the correlation is used but the constants are adjusted to MTU airfoil data.

### Blockage

A SCM treats the flow in an inviscid manner, thus hub and casing boundary layers are not accounted for. Beside losses which are discussed above, boundary layers as well cause a velocity deficit. In the case of flat plates displacement thickness is used to account for this difference of inviscid to actual flow. If the plate surface would be displaced by this amount the boundary layer can be replaced by the free stream quantities up to the wall (i.e. inviscid flow). For compressors blockage is defined in a similar way by [5]

$$B = \frac{\dot{m}}{\int \rho v_x dA} \quad (2.7)$$

where  $\dot{m}$  is the total mass flow,  $A$  is the annulus cross-sectional area and  $\rho$  and  $v_x$  are density and axial velocity of the inviscid flow. Blockage is included into the SCM through the continuity equation (eq. 2.2) by multiplying the right hand side (RHS) with  $B$ .

## 2.3. SGV

Equations 2.1 and 2.2 can't be solved in closed form. Thus a numerical solution is performed on a grid composed by streamlines and calculation planes. Inner and outer streamline are hub and casing contours respectively and in between a freely chooseable number of streamlines is placed which gives the resolution in spanwise direction. The streamlines are commonly placed such that, the same mass flow passes through

every streamtube. In streamwise direction calculation planes are laid and the spacing of them gives the grid resolution in this direction. In this work all blade row inlet and exit planes are specified as calculation planes. Additional calculation planes may be laid in the vaneless space (e.g. if the streamwise extension is large, inlet, outlet,...). Inside the blade passages no calculation planes are placed in this work.

### Calculation Procedure

In Figure 2.4 the flow chart of the *SGV* program is presented. First the input file

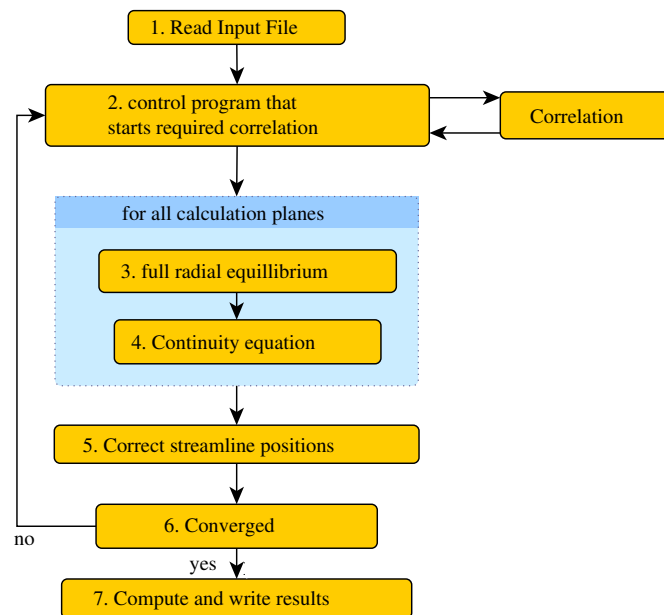


Figure 2.4.: *SGV* Flow Chart [2]

containing all required quantities (geometry information, correlation factors, ...) being described in the *SGV* manual [2] is read. For the first iteration an initial guess of the streamlines is required. This estimate can either be provided by the user, or if already one run of the program was performed the solution of the last run is available in the input file and used as an initial guess. A control program starts the required correlations based on this initial guess for the first run and on the flow field obtained from the solution of the previous iteration. Once all correlations are finished the basic SCM is started. Step 3 and 4 are executed for all calculation planes starting with the first and advancing in streamwise direction. Along the streamlines stagnation enthalpy (or in the relative system rothalpy (see Cumpsty [5])) is conserved. The meridional velocity gradient is obtained from the full radial equilibrium (eq. 2.1). Using this result the continuity equation (eq. 2.2) is solved for the meridional velocity along the

quasi orthogonal direction. Once these computations are finished for all calculation planes the new streamline positions are computed. If they changed with respect to the last iteration the process is restarted at step 2 with the new streamline positions. To keep the change of the streamline positions small and thus ensure stability relaxation is applied. Once the solution is converged the results are computed and written to the result files.

### Program Modes

SGV can be executed in several modes which differ by the quantities given and obtained. The modes used are briefly described. Here the basic working principle is presented to understand the application and a more detailed view can be found in the SGV Manual [2]. The modes are described in the way they are used in this work.

### Design Mode

In the design mode the desired stagnation stage pressure ratios and degrees of reaction are used to compute the blade angles. The following quantities have to be provided:

- *Geometry*: hub and casing contour, all desired calculation planes (blade inlet and exit planes are specified as calculation planes), IGV flow angles
- *Stage*: stagnation pressure ratio and degree of reaction
- *Inlet*: mass flow, stagnation pressure and temperature, number of streamlines and streamline slope
- *Miscellaneous*: rotor speed, streamline slope at outlet, flow angle at outlet, bleeds
- *Optional*: design incidence change, loss correlation factors, if available blade geometry details like leading edge thickness to improve correlation

The SCM is applied in streamwise direction thus the flow quantities at the calculation plane upstream are always known. In the vaneless space between two blades stagnation enthalpy is assumed to be constant.

Rotor outlet angles are obtained from the stage stagnation pressure rise. Considering isentropic (loss-free) compression enthalpy rise and thus work input are obtained from the stage pressure rise. Using the loss correlation factors the general loss correlations can be adjusted to give better results for the particular compressor. To account for the stage losses obtained by correlations an entropy which yields a higher work input for

the given pressure rise is considered. Using the Euler equation for turbomachinery the exit flow angle and velocity are calculated. Finally the blade angle is computed by subtracting the incidence (design incidence + incidence change for stability enhancement) from the flow angle.

In a similar way the stator outlet angles are obtained from the degree of reaction of the proceeding stage (see [6] for details).

### Off-Design Mode

In order to perform off-design computations a converged design calculation has to be available. Off design profile loss characteristics as well as design flow angles are obtained in the design case and are required for off-design computations. Hence the compressor geometry is fixed in this case. Some additional parameters not available in the design case, are now available. The set of adjustable quantities is thus:

- *Inlet*: mass flow, stagnation pressure and temperature, number of streamlines and streamline slope
- *Miscellaneous*: rotor speed, streamline slope at outlet, bleeds
- *off design specific*: variable guide vanes angles, IGV loss and deviation (are not correlated by SGV)

Specifying a new operating point by changing one or more quantities the flow field in the compressor is computed. The choice of a new operation point though is not arbitrary. For the first iteration the streamline positions results for the previous operation point is used as pre-estimate. If the new operation point has changed too much with respect to the old one, convergence can't be obtained. In this case additional points have to be used to allow for smooth changes. For computation of complete compressor maps a tool was developed where reduced mass flow, VGV schedule reduced corrected speed and clearance are automatically adjusted in a specified range.

Like in the design case the inlet flow angle to a blade row is computed from the outlet flow angle of the upstream row. For off-design conditions generally this inlet flow angle is different to the design flow angle and thus gives a different incidence from which deviation and losses are correlated. The sum of deviation and blade angle gives the new outflow angle. Using these angles and applying the SCM across the blade row the flow field and thus the static pressure rise is computed.

# Chapter 3.

## Modelling of Tip Injection for SGV

As pointed out in chapter 1 the unsteady 3-dimensional flow can't be computed using a streamline curvature tool but has to be modelled. In case of tip injection, discrete jets enter through the casing. Thus the outflow conditions of the preceding stator are changed. The rotor experiences modified inflow conditions which are derived in section 3.1 and are of unsteady nature in the rotor's frame of reference. According to Schneider [27] and Matzgeller [22] the unsteady effects are assumed to be significant and hence have to be considered. Therefore, in section 3.2 theory on unsteady flow about airfoils and on consideration of inlet distortions is presented. In terms of inlet distortions, methods have been developed that model the unsteady inflow. Similar modelling is then performed for tip injection yielding a dynamic system in section 3.3 linking the flow field ahead of the rotor to its transient response. Its implementation of the correlation is finally discussed in section 3.4.

### 3.1. Inflow Conditions

The Euler equation for turbomachinery defined by

$$w = u_2 c_{u2} - u_1 c_{u1} \quad (3.1)$$

gives the work added to the fluid by a rotor. Blade speeds  $u$  can be obtained from geometry and rotor speed.  $c_{u1}$  and  $c_{u2}$  are the circumferential absolute velocity components at rotor inlet and outlet respectively.  $c_{u2}$  is obtained from the flow about the rotor which depends on the rotor inlet conditions. Hence, first the unsteady rotor inlet conditions have to be modelled adequately to be suitable for a SCM.

The inlet conditions are obtained at the rotor leading edge (LE) surface. In 3.1 (a) the projection of one periodic unit (as discussed in section 1.3) of the inlet flow at the

rotor LE is presented. The inlet conditions shown are based on to the assumptions that are performed in this section. Jet and main-flow segments are indicated by different patterns. It is assumed that main-flow and jet quantities are constant in circumferential direction. Jets extend the height  $h_{inj}$  from the casing into the main flow to radius  $r_{inj}$ . This yields two different radial profiles. One comprising completely the main flow (e.g.

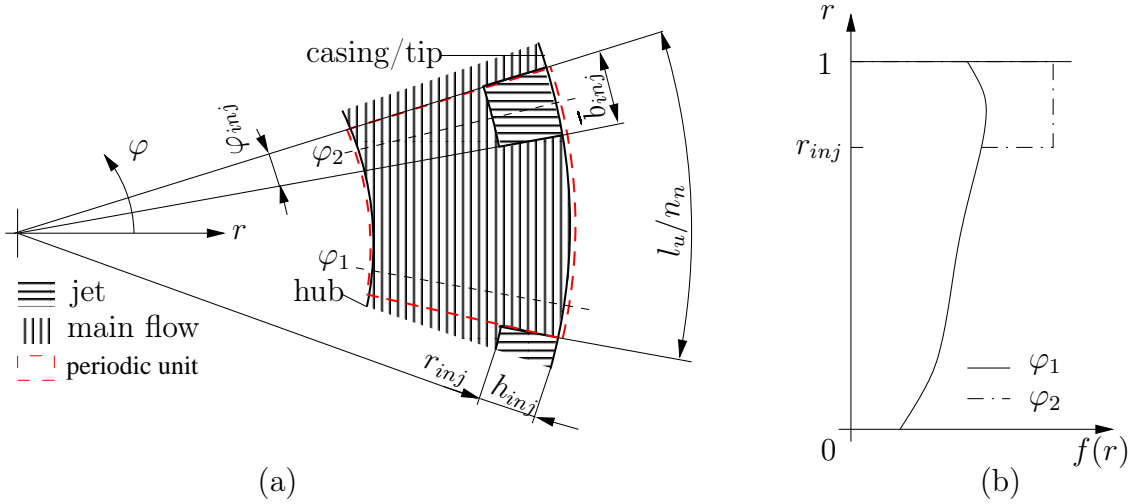


Figure 3.1.: Sections of Jet and Main flow presented in a View along the Compressor Axis

at  $\varphi_1$ ) for normed radius in the range of 0 to  $r_{inj}$ . The other (e.g. at  $\varphi_2$ ) comprising the main flow up to  $r_{inj}$  and jet quantities between  $r_{inj}$  and 1. In Figure 3.1 (b) these radial profiles are plotted. Thus, for normed radii in the range of 0 to  $r_{inj}$  both profiles are equivalent. For radii greater than  $r_{inj}$  the profiles are different.

In the rotor LE plane the set of flow quantities  $f$  has to be obtained as functions of the radius and the angular coordinate  $f(r, \varphi)$ . It is convenient to treat the circumferential distribution of flow quantities first  $c(\varphi)$ . Circumferential distributions at all radii give the flow field  $f(r, c(\varphi))$ . In this way the circumferential distributions are constant for radii smaller than  $r_{inj}$  because the whole circumference is of main-flow type. This assumption is verified later in this section. The circumferential characteristics of flow quantities for radii greater than  $r_{inj}$  are a function of the angular position  $\varphi$ .

Using tip injection as described in section 1.3 jets enter the annulus through slots. The nozzles are directed in a way that these jets turn to be aligned with the casing due to the Coanda effect. As they approach the rotor through main-flow interaction their direction and stagnation pressure are changed. This phenomena has been treated by Matzgeller [21] using CFD computations. A box with a nozzle located at the top face was used as calculation domain. The nozzle was inclined with respect to the top

surface at a certain angle obtained from the tip injection setup used in tests. It was also inclined to the main-flow in the horizontal plane. Injection flow was created by a higher stagnation pressure boundary condition ahead of the nozzle.

Results from CFD computations were obtained varying

- $\frac{p_{t,inj}}{p_s}$ :  $p_{t,inj}$  is the stagnation pressure in the injection pipe upstream of the nozzle and  $p_s$  is the static pressure in the main flow at the point of injection
- $AR_n = \frac{w_t}{h_t}$ : aspect ratio of the nozzle throat where  $w_t$  and  $h_t$  are width and height of the nozzle throat (compare Figure 3.2)
- $\Delta\alpha_{inj} = \alpha_{inj} - \alpha_{mf}$ : angle between the jet and main-flow in the horizontal plane

in order to cover the operation range expected for common tip injection setups. At several down-stream positions mean stagnation pressure loss and mean deviation of the jet were recorded in a results matrix. In Figure 3.2 the adaption of the geometric relations used in the generic CFD model described above are shown in a circumferential plane. The coloured box represents the slot with its inclination  $\alpha_{inj}$  to the circumfer-

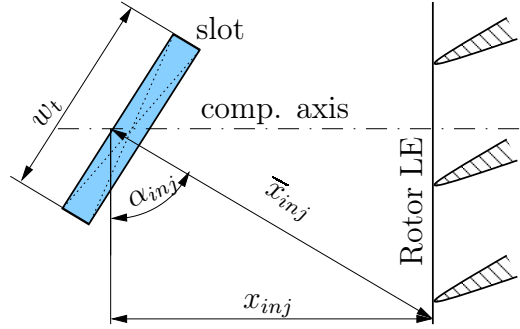


Figure 3.2.: Geometric Definitions of Correlation Parameters

ential direction.  $x_{inj}$  is the axial distance from the box to the rotor LE as shown in Figure 3.2. For deviation and stagnation pressure loss correlations by Matzgeller [21], the distance from the slot center to the rotor leading edge in jet direction defined by

$$\bar{x}_{inj} = \frac{x_{inj}}{\sin(\alpha_{inj})} \quad (3.2)$$

is required. Using these parameters  $c_d$  and  $c_\alpha$  can be computed from the result matrix obtained by Matzgeller [21].  $c_d$  is defined by

$$c_d = \frac{p_{t,LE} - p_s}{p_{t,inj} - p_s} \quad (3.3)$$

where  $p_{t,LE}$  is the mean of the stagnation pressure in the jet at rotor LE being a function of  $\bar{x}_{inj}$  and  $c_\alpha$  defined by

$$c_\alpha = \frac{\alpha_{LE} - \alpha_{mf}}{\alpha_{inj} - \alpha_{mf}} \quad (3.4)$$

where  $\alpha_{LE}$  and  $\alpha_{mf}$  are the mean of absolute flow angles in the jet at rotor LE and in the main flow upstream of the injection respectively. Rearranging equations 3.3 and 3.4 the stagnation pressure and absolute flow angle at rotor LE in the jet are obtained. It is assumed that no heat exchange between the jet and either wall or main flow occurs, such that the stagnation temperature of the jet remains constant.

The jets which are deviated and decelerated due to jet/main-flow interaction also affect the main-flow. Because the jets are generally small compared to the main-flow it is assumed that the deviation and stagnation pressure loss of the main-flow can be neglected. The jets though capture part of the annulus cross section and act like an additional blockage. Hence the change in the main-flow quantities due to injection has to be obtained for example by the SCM.

For radii greater than  $r_{inj}$  main-flow and jet quantities are apparent. The circumferential extension of either segment is required in order to derive the circumferential profile. Considerations performed in section 1.3 gave the circumferential extent of either flow segment at a plane immediately downstream of the injection slots. Assuming that the angular extend of the jet doesn't change between the slot and rotor LE the same angular distributions occur at rotor LE. For small  $\bar{x}_{inj}/w_t$  as used in the investigations in this work this is in good agreement with CFD (compare [21] and section 3.1). Referring to Figure 3.1 one periodic unit is composed by one jet section and its preceding main flow section. The circumferential fraction of the jet to the extent of one periodic unit is defined by:

$$a_{inj} = \frac{\bar{b}_{inj}}{l_u/n_n} = \frac{\varphi_{inj}}{2\pi/n_n} \quad (3.5)$$

where  $\varphi_{inj}$  is the angular extension of the jet given by  $\varphi_{inj} = \frac{\bar{b}_{inj}}{r_{tip}}$

Along the angular direction for every periodic unit at a radius greater than  $r_{inj}$  a main-flow section and a jet section exist. Assuming that in each section the flow quantities are constant a rectangular profile  $q(\varphi)$  results. Inside the jet the flow quantity has the value  $q_{inj}$  and in the main-flow it is  $q_{ms}$ . In order to obtain a uniform profile along the angular coordinate for all different flow quantities the transformation defined by

$$f(\varphi) = \frac{q(\varphi) - q_{ms}}{q_{inj} - q_{ms}}, \quad (3.6)$$

with  $q$  being an arbitrary quantity.  $f(\varphi)$  is the difference between quantity itself at an arbitrary angle and main flow quantity divided by the difference of jet and main flow quantity. Inside the jet and main flow  $f(\varphi)$  equals 1 and 0 respectively for all

main-flow quantities. In order to verify the assumption that the flow quantities within a segment are constant in angular direction a sample rectangular profile is plotted along unsteady CFD results at rotor LE (see [21]) in Figure 3.3 (a). The CFD profile

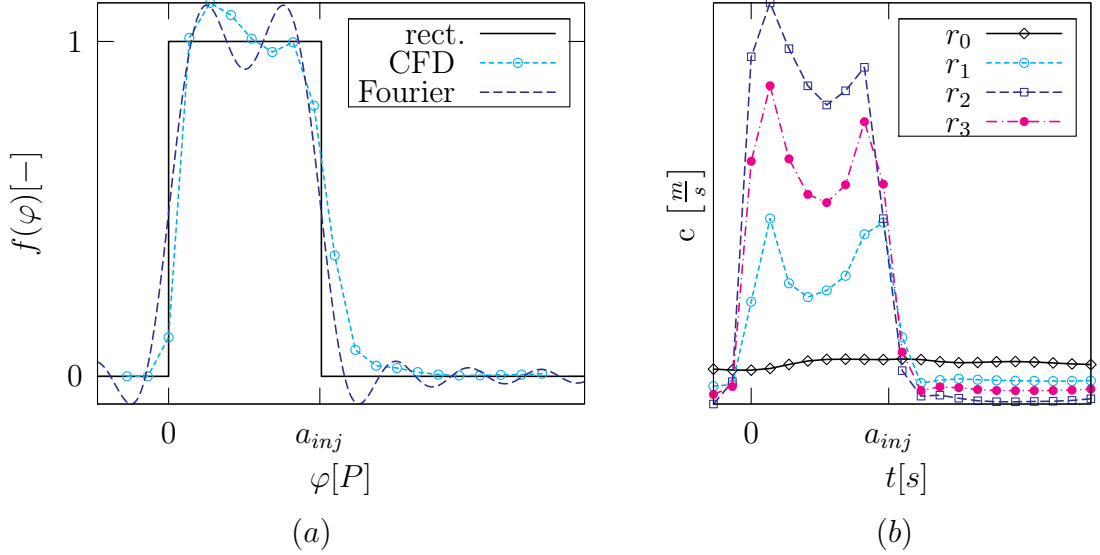


Figure 3.3.: (a) Comparison of Modelled Inflow Conditions with CFD; (b) Inflow Conditions obtained from CFD at various radii

plotted is obtained at a representative radius (maximum stagnation pressure along the radial profile which is close to the middle of the jet). In order to verify that this profile represents the angular distributions for other radii as well, distributions of absolute velocity at several radii are plotted in Figure 3.3 (b).  $r_0$  is immediately below the jet and it can be seen that there is little change of the velocity in the circumferential direction thus the assumption made above can be confirmed. Other radial positions bespeak positions inside the jet. The shape of the angular velocity profiles at these radii is similar but the magnitude is different which is a result of the shear layers (see Kahn [15]) at the interfaces to main-flow and wall. Thus only one radial position has to be treated in order to capture the profile's shape. Nevertheless, applying a pressure loss correlation ( $c_d$ -value) should give the mean of the radial profile.

In Figure 3.3 (a) it is easy to see that the angular extension at rotor leading edge of both rectangular and CFD  $f(\varphi)$ -profile is similar which confirms the assumption that the angular extension of the jet doesn't change from injection point to rotor LE. According to Matzgeller [21] at the jet borders vortices appear due to the interaction of jet and main flow because being the reason for the wiggles in the CFD  $f(\varphi)$ -profile (compare jet in crossflow i.e. [15]).

The rectangular characteristic is approximated by a Fourier series and thus transformed to a continuous function. This approximation on the one hand is convenient because a continuous function is easier to implement into a computer program but also represents the profile in a better way because no discontinuities occur. The order of the Fourier series ( $n = 9$ ) is chosen such that it complies best with CFD results. The resulting Fourier series is of the form

$$f(t) = \sum_{k=0}^9 [a_k \cos(k\omega t) + b_k \sin(k\omega t)] \quad (3.7)$$

with the Fourier coefficients for a rectangular input signal

$$a_k = \frac{1}{k\pi} \sin(2\pi k a_{inj}) \quad (3.8)$$

$$b_k = \frac{1}{k\pi} [1 - \cos(2\pi k a_{inj})] \quad (3.9)$$

and the angular frequency for period  $T$

$$\omega = \frac{2\pi}{T}. \quad (3.10)$$

In Figure 3.3 (a) the obtained Fourier series is plotted along the rectangular and CFD  $f(\varphi)$ -profiles.

Circumferential profiles of the inflow quantities have been derived up to now. In the derivation the radius  $r_{inj}$  was used as limiting value for constant profile below it and varying flow quantities for radii greater than it. Now this radius is obtained by the use of continuity equation defined by

$$\dot{m}_{inj} = \rho_{inj} c_{ax,inj} A_{inj} \quad (3.11)$$

where  $\rho_{inj}$  and  $c_{ax,inj}$  are given by the averaged flow quantities inside the jet. Thus knowing  $\dot{m}_{inj}$  the area  $A_{inj}$  can be obtained. On the other hand the area of the jet is given by the circular ring segment (compare Figure 3.1)

$$A_{inj} = (r_c^2 - r_{inj}^2) \pi a_{inj} \quad (3.12)$$

where  $r_c$  is the casing radius and  $r_{inj}$  is the inner radius of the jets. The jet height is defined by

$$h_{inj} = r_c - r_{inj}. \quad (3.13)$$

Combining and rearranging equations 3.11, 3.12 and 3.13 gives

$$h_{inj} = r_c - \sqrt{r_c^2 - \frac{\dot{m}_{inj}}{\pi a_{inj} \rho_{inj} c_{ax,inj}}}. \quad (3.14)$$

Summarizing the inflow conditions gives:

- $q(r, \varphi) = q_{ms}(r)$  for  $r \in [r_{hub}, r_{inj}]$
- $q(r, \varphi) = q_{ms}(r) + f(r, \varphi) (q_{inj} - q_{ms}(r))$  for  $r \in [r_{inj}, r_{casing}]$

In the inner segment constant flow conditions are present along the angular direction but the flow conditions in the outer segment vary with the angular position. These conditions are of steady nature in the absolute frame of reference but because the rotor turns with respect to the inlet profiles it experiences unsteady inflow conditions.

## 3.2. Unsteady Flow

The inlet conditions obtained in section 3.1 give an unsteady inflow profile in the relative frame of reference. Streamline curvature computations are performed in a steady way thus the unsteady effects can't be accounted for by this method. Hence, if the system dynamics have an impact on the flow field they have to be implemented by an external method.

Mazzawy et. al. [23] discussed compressor subjected to inlet distortions. A reduced frequency was defined as

$$\omega_{red} = k \frac{L \cdot f}{u}, \quad (3.15)$$

where  $L$  is the characteristic length of the system under consideration,  $f$  is the frequency of the dynamic inlet flow and  $u$  is the fluid velocity.  $k$  is a constant coefficient that is generally set to  $\pi$ . The reduced frequency is the ratio of the time it takes the fluid to traverse through the system ( $\frac{L}{u}$ ) to the period of the disturbances ( $\frac{1}{f}$ ). In the reduced frequency range  $\omega_{red} \in [0.01, 10]$  unsteady flow has to be considered. For reduced frequency less than 0.01 the system response is in quasi-steady manner. At reduced frequencies higher than 10 the fluid's unsteady period is much smaller than it takes the fluid to pass the system and the system has little time to respond. For tip injection the reduced frequency is in the order of 1 thus system dynamics have to be considered even though the amplitudes of the system response are assumed to be small.

In order to develop a method that can approximate the unsteady effects of tip injection using the steady SGV, considerations on airfoils subjected to unsteady inflow conditions are discussed. In contrast to blade rows, unsteady flow effects on airfoils have been investigated by several authors (e.g. Melick et. al. [24] [24], Kármán et. al. [16], Ericsson et. al. [7]).

First the relation of Lift and Drag for airfoils and the work input into a blade row is presented for steady flow to show the connection of considerations on isolated airfoils and blade rows. Then basic considerations on unsteady flow about isolated airfoils are considered, before the dynamic system used by e.g. by Melick for inlet distortions computations is presented. Even though inlet distortions generally affect big segments of the inflow face, there as well unsteady inflow conditions in the relative frame of reference have to be treated, which justifies their considerations in this work.

### 3.2.1. Relations between Isolated Airfoil and Blade Row

In order to apply results obtained for isolated airfoils to blade rows, first the step from isolated airfoils to blade cascades is presented and then the step from blade cascades to turning blade rows is performed. Weinig [33] showed that lift coefficients for isolated airfoils and airfoil cascades can be related using conformal mapping. In the steady case for an isolated airfoil the lift coefficient is a function of the inflow angle and this relation often is represented by the lift curve which has a slope of  $2\pi$  considering thin airfoil theory [9]. In terms of blade cascades in the steady case as well a lift coefficient can be defined which is briefly rederived in the following.

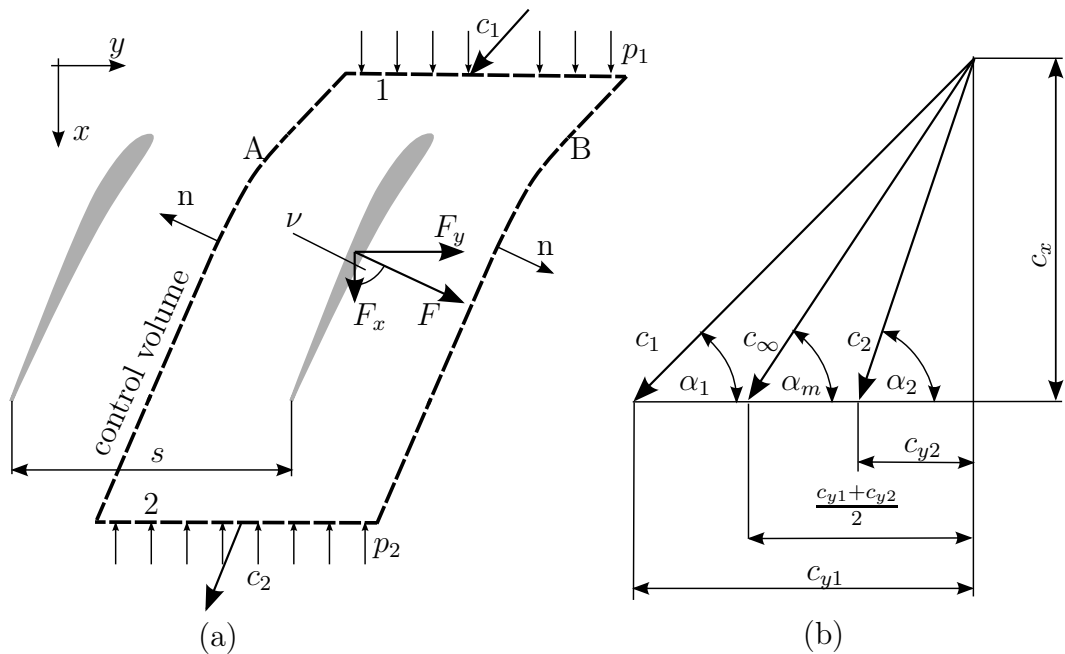


Figure 3.4.: (a) Momentum Balance about an Airfoil Cascade; (b) Velocity triangle [12]

In Figure 3.4 (a) an airfoil cascade is presented where  $s$  is the spacing of the blades. A and B are the mean streamlines of two adjacent blades and thus congruent. These streamlines and the horizontal inlet (1) and outlet (2) planes comprise a control volume

with unit height. The flow is assumed to be frictionless and incompressible. According to the Bernoulli equation [12] the pressure rise in the cascade can be expressed by

$$\Delta p = p_1 - p_2 = \frac{\rho}{2} (c_2^2 - c_1^2) \quad (3.16)$$

From the continuity equation one obtains that the axial flow velocities at inlet and outlet are equal.

$$c_{x1} = c_{x2} = c_x \quad (3.17)$$

Along both streamlines the same pressure is apparent but since normal vectors have different signs no resulting force appears. The momentum balance in  $x$ -direction given by [12]

$$F_x = (p_2 - p_1)s \quad (3.18)$$

can further be transformed by substituting the Bernoulli equation 3.16 to

$$F_x = s \frac{\rho}{2} (c_1^2 - c_2^2). \quad (3.19)$$

The momentum Balance in  $y$ -direction yields

$$F_y = -\dot{m} (c_{y2} - c_{y1}) = -\rho s c_x (c_{y2} - c_{y1}). \quad (3.20)$$

$\nu$  the angle of the blade force with respect to the axial direction is obtained by (compare Figure 3.4 (a))

$$\tan(\nu) = \frac{F_y}{F_x} \quad (3.21)$$

and substituting  $F_x$  and  $F_y$  it can be simplified to

$$\tan(\nu) = \frac{2c_x}{c_{y2} + c_{y1}}. \quad (3.22)$$

The mean vectorial absolute velocity  $\vec{c}_\infty$  is defined by (compare Figure 3.4) (b)

$$\vec{c}_\infty = \frac{\vec{c}_1 + \vec{c}_2}{2} \quad (3.23)$$

with its angle

$$\tan \alpha_\infty = \frac{c_x}{\frac{c_{y1} + c_{y2}}{2}} = \frac{2}{\cotan \alpha_1 + \cotan \alpha_2} \quad (3.24)$$

to the tangential direction. Comparing equations 3.24 and 3.22 one can easily see that  $\nu$  and  $\alpha_\infty$  are equal and thus the blade force is perpendicular to  $c_\infty$ . This statement is only true for frictionless flow. The blade force for the frictionless case is defined by

$$F = \frac{F_y}{\sin(\alpha_\infty)} \quad (3.25)$$

as for isolated airfoils the lift coefficient for airfoil cascades is introduced as dimensionless quantity (see [12])

$$c_l = \frac{F}{\frac{1}{2}\rho c_\infty^2 c_b} \quad (3.26)$$

where  $c_b$  is the blade chord length. Substituting equations 3.20 and 3.25 in 3.26 and using geometric relations (compare Figure 3.4 (b)) it follows that

$$c_{y_{1,2,\infty}} = c_x \cotan(\alpha_{1,2,\infty}) \quad (3.27)$$

for velocity triangles 1, 2 and  $\infty$  respectively and

$$c_x = c_\infty \sin \alpha_\infty. \quad (3.28)$$

Eventually for the lift coefficient following relation is obtained

$$c_l = 2 \frac{s}{c_b} \frac{c_{y1} - c_{y2}}{c_\infty} = 2 \frac{s}{c_b} (\cotan \alpha_1 - \cotan \alpha_2) \sin \alpha_\infty. \quad (3.29)$$

Equation 3.29 shows that in contrast to single airfoils the flow downstream of the airfoil is turned and the lift coefficient does not depend only on the inflow angle but also on the outflow angle.

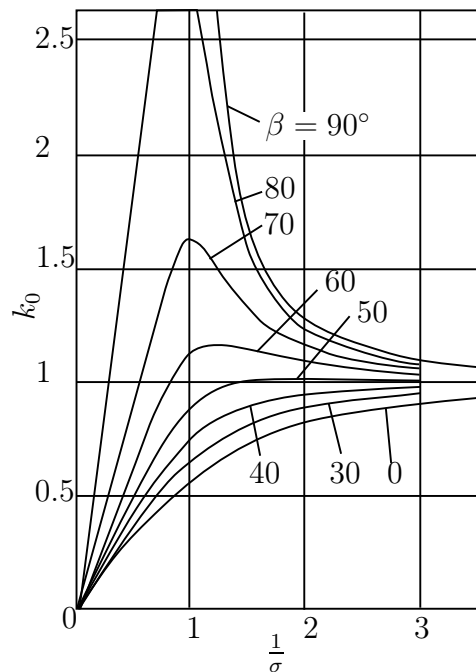


Figure 3.5.: Relation of lift coefficient for Isolated Airfoil and Cascade [33]

Between lift for isolated airfoils and lift in blade cascades (as derived above) a relation exists which is shown by Weinig [33]. This relation was obtained applying conformal

mapping to a blade cascade. A factor  $k_0$  being the ratio of lift coefficient for airfoil cascades to isolated airfoils is the result obtained:

$$k_0 = \frac{C_{l,cascade}}{C_{l,isolatedairfoil}} \quad (3.30)$$

It is found to depend on solidity defined by

$$\sigma = \frac{c_b}{s}$$

i.e. the ratio of blade chord to blade pitch and the stagger angle  $\beta$  with respect to the compressor axis can be defined. This relation is presented in Figure 3.5.

Considering a rotor lift can be related to work input into the fluid by the blade row thus the desired relation of lift for isolated airfoils and work input for steady conditions is finished. Using loss correlations the pressure rise can be obtained from the work.

Assuming adiabatic flow the power input to the fluid by a rotor can be expressed by

$$P = \dot{m} \Delta h_t = L_u u \quad (3.31)$$

where  $L_u$  is the circumferential component of the lift,  $u$  is the blade speed and  $h_t$  is the stagnation enthalpy rise in the stage. The circumferential component of the lift is

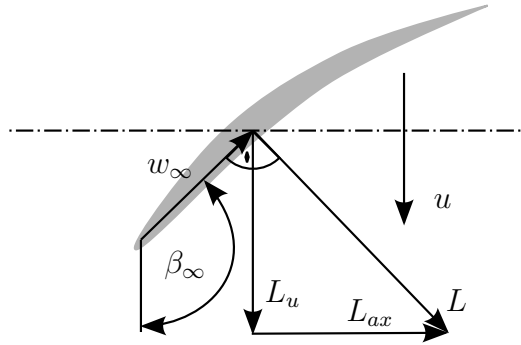


Figure 3.6.: Lift of a Blade Row

given by (compare Figure 3.6)

$$L_u = L \sin(\pi - \beta_\infty) \quad (3.32)$$

Substituting equation 3.32 in 3.31 and rearranging yields

$$\Delta h_t = L \frac{\sin(\pi - \beta_\infty) u}{\dot{m}} \quad (3.33)$$

showing the relation of lift to stagnation enthalpy rise in a rotor in the steady case. Hence, lift is related to the work input and thus stagnation temperature rise.

The circumferentially varying inlet conditions as depicted in section 3.1 yield different stagnation pressure rise which generally also leads to different static pressure rise. In order to combine the different circumferential segments a parallel compressor model would be in need up to the blade row at which the static pressure along the circumference is uniform again because of mixing effects. However, CFD results show that the circumferential static pressure distribution shows no significant variation at rotor exit arising from tip injection (Matzgeller [22]). The reason for this is expected to be the high reduced frequency for tip injection systems which yields low amplitude for the stagnation pressure rise at rotor outlet. Assuming that static pressure doesn't change for segments with and without tip injection no parallel compressor model needs to be applied. Also the dynamic system is comprised only by the first rotor because CFD suggests that the flow is mixed out at rotor outlet. The rest of the compressor is treated steady.

### 3.2.2. Unsteady flow about airfoils

Above the link of flow about isolated airfoils and blade rows was discussed. Assuming that these relations hold as well for dynamic considerations the effects apparent at isolated airfoils subjected to varying inlet conditions also occur in blade rows. Kármán et. al. [16] discussed lift generation of an airfoil in unsteady flow using unsteady thin airfoil theory. According to the thin airfoil theory lift is linked to bound circulation around it. A change in inflow conditions yields a change of the flow about the airfoil. Thus lift and bound circulation are altered. Due to the conservation of angular momentum to counteract the bound circulation vortices are shed into the wake. In steady flow the well known starting vortex results from this phenomenon. The effect of these shed vortices on the flow about the airfoil at a particular point depends on the inverse of the distance between the point and the vortex. Considering lift on an airfoil in steady flow it is assumed that sufficient time has passed and the distance of starting vortex and airfoil is large and does not influence the flow about the airfoil. In unsteady flow vortices are shed into the wake at every change of the inflow conditions, and therefore bound circulation. In order to obtain the flow about the airfoil for unsteady inflow conditions the wake vortices have to be considered.

Complementing Kármán [16] Ericsson et. al. [7] discussed additional phenomena's that occur around airfoils in unsteady flow using a semi-empiric way. These effects can be categorized to time lag effects and transient effects but are not further discussed here because they are approximated by a dynamic system discussed in the following.

According to Melick [24], Fung et. al. [8] suggested that for a change in angle of attack all these phenomenas can be approximated by a second order linear system of the form

$$L(s) = u^2 c \Delta \alpha \Psi(s) \quad (3.34)$$

in the Laplace domain where  $\Psi(s)$  and  $s$  are defined by

$$\Psi(s) = \frac{s^2 + s}{s^2 + 2.82s + 0.8} \quad (3.35)$$

$$s = 2 \frac{Ut}{c_b} \quad (3.36)$$

respectively.  $U$ ,  $t$  and  $c_b$  are free stream velocity, time and airfoil chord respectively.

Melick et. al. [24] proposed further simplification to a first order system. Applying a step input to the system the resulting relation in the time domain is given by

$$\Psi(t) = 1 - e^{-\frac{t}{\tau}}. \quad (3.37)$$

The time constant was found to be

$$\tau_M = \frac{c_b}{u} \quad (3.38)$$

and thus equal to the time it takes a particle to move from the leading edge to the trailing edge.

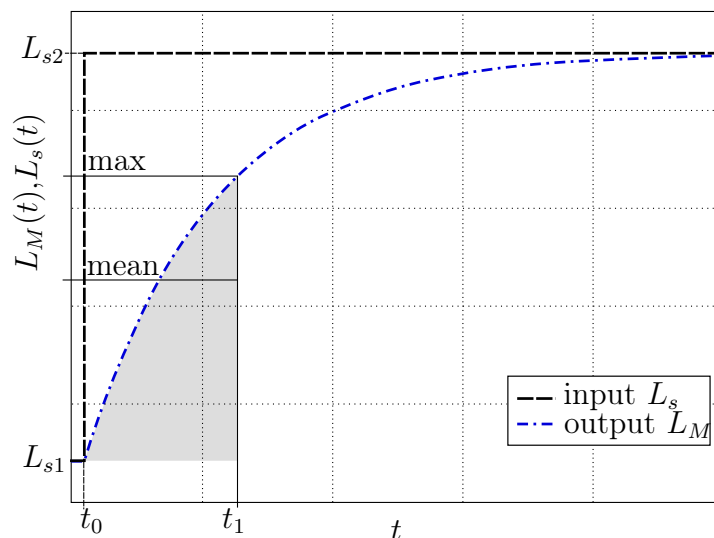


Figure 3.7.: Dynamic System for one Segment

In Figure 3.7 the response of this dynamic system (equation 3.37) to a step input is presented. At time  $t_0$  a step like change in the inflow conditions to the airfoil occurs.

Using the steady lift equation

$$L_s = \frac{1}{2} \rho u^2 c_l A \quad (3.39)$$

along with equation 3.37 the quasisteady lift is obtained, where  $A$  is the projected area of the airfoil. Computing the lift using equation 3.39 the lift follows the inflow conditions instantaneously. As discussed above the flow about the airfoil needs some time to adjust to the new inlet conditions and thus the actual lift lags the instantaneous change which is represented by  $L_M$  being the system response obtained by the first order system proposed by Melick.

Assuming that the inflow conditions change back to their value before  $t_0$  at time  $t_1$  (i.e. the inflow is disturbed for small time only) the steady state lift for the inlet conditions apparent in the time frame  $t_0$  to  $t_1$  is never reached. Considering that the inlet conditions in this time frame are unfavourable compared to the conditions outside this frame and would cause stall in the steady case, the dynamic system will not stall as long as the critical lift is not exceeded. The critical lift in the unsteady case is generally greater than in the steady case, because stall needs some time to develop. Hence, stall is further delayed because of this phenomena.

### 3.3. Dynamic System

In section 3.2 it was shown that unsteady flow effects about isolated airfoils can be computed using a first order dynamic system. Melick [24] and Mazzawy [23] treated compressors subjected to inlet distortion and both found that a first order dynamic system can represent the system dynamics sufficiently. Melick computed so called effective inlet quantities employing a dynamic system that uses the steady lift equation to compute the dynamic lift. In this section in a similar way effective quantities for the tip injection system are discussed.

In Figure 3.8 the semi dynamic system used in this work is presented along with a model known to be sufficiently accurate for computations of unsteady flows. Navier Stokes equations, continuity equation and energy equation are the modelling equation known to represent reality in a good manner. With this set of equations theoretically a close to reality solution can be obtained. However, solving is not possible in closed form and generally performed by computational fluid dynamics, known to be time consuming.

In order to accelerate the computations, the process presented in Figure 3.8 (a)

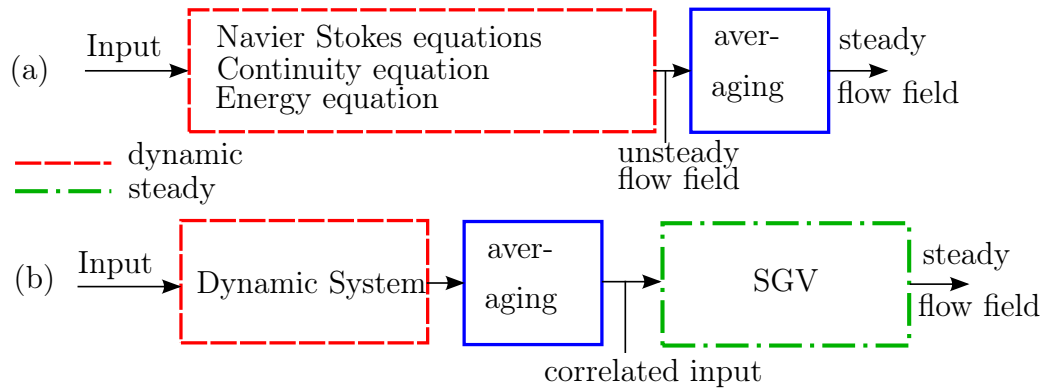


Figure 3.8.: (a) Unsteady Flow Model (b) Semi - Dynamic Model

is simplified to a semi-dynamic model yielding approximated solutions using SGV. Basically SGV solves the flow field through the compressor in a steady way. Good solutions for compressors without tip injection can be obtained in this way because correlations are applied to correct modelling errors sufficiently. These correlations don't account for the unsteady flow due to tip injection. Hence, in a first step the flow dynamics have to be captured using a dynamic system. This is achieved by introducing so called effective inlet quantities that capture the flow dynamics and can be used with steady aerodynamics. By time averaging, the dynamic quantities are transformed into the steady domain and forwarded to SGV where the steady flow field is computed. As pointed out in this section the reduced frequency for typical tip injection systems as used by Suder [30] and Hiller [13] are high such that fluctuations of flow quantities are small. This yields that the amplitude of the oscillations are rather small thus only its mean has to be considered.

### 3.3.1. Effective quantities

As mentioned above effective quantities can be derived in case of isolated airfoils in order to represent the blade's response to unsteady inflow conditions. The derivation of effective inlet quantities is presented in the following.

In section 3.1 it was found that the circumferential variation of inflow conditions at radii less than  $r_{inj}$  was small, thus at surfaces of revolution of  $r < r_{inj}$  constant inflow conditions along the circumference are present. Circumferential variation of the inflow conditions are just present for surfaces of revolution at radii in the range of  $r_{inj}$  to  $r_{cas}$ . This circumferential variation yields unsteady inflow conditions for the rotor because it is rotating in this flow field.

The unsteady process for a rotor subjected to unsteady inflow conditions in the relative frame of reference basically can't be treated by steady computations. In the following the steps from obtaining the work input to a blade row using unsteady aerodynamics to steady aerodynamics with adjusted inlet conditions is presented.

1. *Relation of blade row and isolated airfoil:* Due to the relation of isolated airfoil and blade row presented in section 3.2 and the assumption that this relation holds in the unsteady case instead of considering unsteady flow about airfoil cascades unsteady flow about isolated airfoils can be treated.
2. *Considering changing inflow conditions separately:* In case of tip injection flow velocity, inflow angle and density vary instantaneously. Assuming that the response of the lift on the change of either inlet flow quantity is similar concerning the order of the dynamic system, the three systems can be considered separately.
3. *Effective inflow conditions:* Similar to Melick [24], instead of computing the dynamic response to varying inflow conditions using unsteady aerodynamics, the inflow conditions are transformed to account for the unsteady flow effects, thus the lift can be computed using steady equations.

In the following the last two points are discussed in more detail.

Generally the jet has a different stagnation pressure and absolute flow angle than the main flow and might have a different stagnation temperature. This implies that  $\rho$ ,  $w_\infty$  and  $c_l$  change with respect to the circumferential position in the absolute frame of reference and thus in time in the relative frame of reference. As pointed out in section 3.1 inflow conditions can be approximated by a rectangular signal. Within one period two steps occur one from the main flow quantities to the jet and vica versa.

At first, a step input to the system at time  $t_0$  is considered. According to Melick (compare equation 3.37) the response of lift can be approximated by a first order linear system in the from

$$L(t) = L_0 + \Delta L(t) = L_0 + (L_{end} - L_0) \left[ 1 - e^{-\frac{t-t_0}{\tau}} \right] \quad (3.40)$$

where  $L_0$  and  $L_{end}$  are the steady state lift at  $t < t_0$  and  $t > t_0$  respectively. In the steady case lift is defined by

$$L = \frac{1}{2} \rho w_\infty^2 c_l c_b \quad (3.41)$$

where  $c_l$  is a function of in and outflow angles in case of a cascade (see equation 3.29) and of the angle of attack in terms of isolated airfoil.

In order to explain the concept of effective inlet quantities, the following considerations are performed using the density as varying quantity but also any other quantity on the right hand side of equation 3.41 could have been used. Effective density lagging its actual value as introduced by Melick [24] is defined by

$$\rho_{eff}(t) = \frac{L(t)}{\frac{1}{2}w_{\infty}^2 c_l c_b} \quad (3.42)$$

and because all other terms on the right hand side are held constant with time the same system dynamics that apply to the Lift (see equation 3.40) are also apparent for the density. Substituting equation 3.40 into 3.42 and simplification yields

$$\rho_{eff}(t) = \rho_0 + (\rho_{end} - \rho_0) \left[ 1 - e^{-\frac{t-t_0}{\tau}} \right] \quad (3.43)$$

Hence, the dynamic lift can be obtained by steady aerodynamics if the inlet quantities lag their real value assuming that the lift follows a first order linear system.

Performing similar analysis for the velocity  $w_{eff}$  and the lift coefficient  $c_{l,eff}$  equations 3.44 and 3.45 are obtained.

$$w_{eff}^2(t) = w_0^2 + (w_{end}^2 - w_0^2) \left[ 1 - e^{-\frac{t-t_0}{\tau}} \right] \quad (3.44)$$

$$c_{l,eff}(t) = c_{l,0} + (c_{l,end} - c_{l,0}) \left[ 1 - e^{-\frac{t-t_0}{\tau}} \right] \quad (3.45)$$

Using the effective quantities derived above the unsteady lift can be obtained by the use of the steady lift equation 3.41:

$$L(t) = \frac{1}{2} \rho_{eff}(t) w_{eff}(t)^2 c_{l,eff}(t) c_b \quad (3.46)$$

The advantage of this approach is, that the dynamic system and the aerodynamic system are separated. First the unsteady system is used to obtain effective inlet quantities and then the unsteady lift is computed by steady aerodynamics with these effective quantities.

Lift coefficient  $c_{l,eff}(t)$  is not an input quantity that is used for SGV thus the related inlet quantity has to be found. According to equation 3.29 the lift coefficient of a blade row depends on geometry and relative flow angles at inlet and outlet. For tip injection the reduced frequency is high yielding small amplitudes of the flow quantities at rotor outlet. Hence, it is assumed that deviation doesn't change with varying inlet angle. Therefore lift coefficient and inlet angle have the same system dynamics given by

$$\beta_{1,eff}(t) = \beta_{1,0} + (\beta_{1,end} - \beta_{1,0}) \left[ 1 - e^{-\frac{t-t_0}{\tau}} \right]. \quad (3.47)$$

### 3.3.2. Validation of the Dynamic System

Melick [24] proposed that for inlet distortions it is sufficient to obtain the effective inlet conditions using a first order dynamic system. In the following this approach is validated for tip injection using unsteady CFD computations carried out by Matzgeller [21]. First the dynamic system used later in this work is presented. Then the response of it to the CFD input data is computed and compared to the CFD response.

Effective flow quantities  $w_{eff}^2(t)$ ,  $\beta_{eff}(t)$  and  $\rho_{eff}(t)$  for a step input can be computed according to equations 3.43, 3.44 and 3.47. Each flow quantity, called  $q$  in the following, is of the form

$$q_{eff}(t) = q_0 + \Delta q_{in} \left[ 1 - e^{-\frac{t-t_0}{\tau}} \right] \quad (3.48)$$

Equation 3.48 is composed of a steady part  $q_0$  and an unsteady part  $\Delta q_{eff}(t)$  defined by

$$\Delta q_{eff}(t) = \Delta q_{in} \left[ 1 - e^{-\frac{t-t_0}{\tau}} \right] \quad (3.49)$$

The differential equation of equation 3.49 is

$$\Delta \dot{q}_{eff} + \frac{1}{\tau} \Delta q_{eff} = \frac{1}{\tau} \Delta q_{in}. \quad (3.50)$$

Substituting the time constant obtained by Melick (compare section 3.2) yields

$$\Delta \dot{q}_{eff} + \frac{1}{\tau_M(t)} \Delta q_{eff} = \frac{1}{\tau_M(t)} \Delta q_{in} \quad (3.51)$$

The time constant (see equation 3.38) is dependent of the flow velocity which changes with respect to time (i.e. a function of the relative rotor position). Thus equation 3.51 is nonlinear in case of tip injection. Rather than using the flow speed and chord length the axial flow velocity and axial chord length are used which gives better results for compressors subjected to inlet distortions. Eventually the dynamic system yields

$$\Delta \dot{q}_{eff} + \frac{c_{ax}(t)}{c_{b,ax}} \Delta q_{eff} = \frac{c_{ax}(t)}{c_{b,ax}} \Delta q_{in} \quad (3.52)$$

For a step change of the inflow conditions after about  $t \approx 5\tau$  ( $\tau$  being the time constant of the system) the steady state value is considered to be reached (from equation 3.49 where  $1 - e^{-5} = 0.9933$ ). Considering the rectangular signal that is apparent for tip injection the inlet conditions are periodic and consist of one main-flow section and one jet section (compare section 3.1) indicated by different patterns in Figure 3.3. In each section the time constant depends on the flow speed and is thus not constant for

the whole period. For a steady oscillation between both steady state values the time in each section has to be sufficient that the steady state value is reached (i.e.  $\Delta t \geq 5\tau$ ) In case of tip injection this is generally not the case and the steady state values are not reached. This implies that even if one steady state value would incept stall because of the dynamic system this value is not reached and thus the blade row might still operate in the stable range.

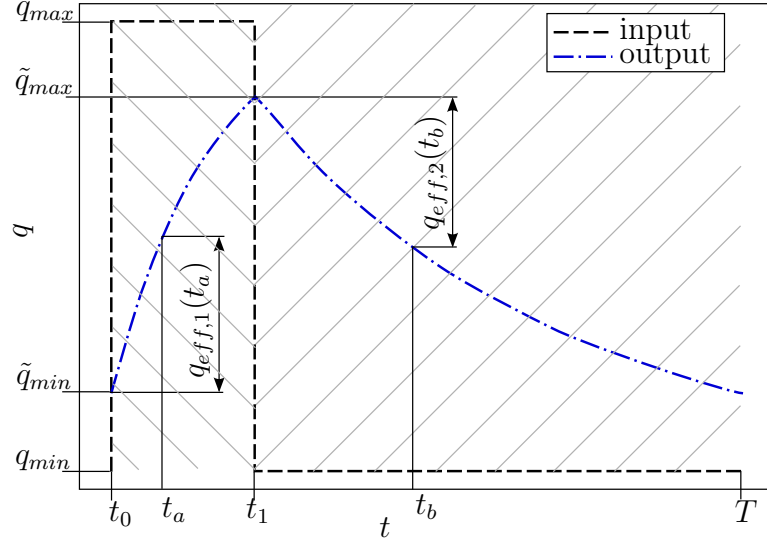


Figure 3.9.: Dynamic System Response to the rectangular Signal for Tip Injection

In Figure 3.9 the rectangular input signal obtained in section 3.1 as an approximation of the input signals for tip injection is shown. The flow quantity inside the jet is represented by  $q_{max}$  whereas  $q_{min}$  is the main-flow quantity. At time  $t_0$  the rotor enters the jet and at  $t_1$  the jet is left thus  $t_1 = a_{inj}T$  (see section 3.1). Applying the rectangular input signal presented to the dynamic system defined by equation 3.52 the system response presented in Figure 3.9 is obtained. This response is discussed in the following. Each flow speed in jet and main flow section is constant thus the time constant in each section is constant. The nonlinear differential equation 3.52 can be transformed into a system of two piecewise linear differential equations of the form

$$\Delta \dot{q}_{eff} + \frac{c_{ax,inj}}{c_{b,ax}} \Delta q_{eff} = \frac{c_{ax,inj}}{c_{b,ax}} \Delta q_{in} \quad t \in [0, t_1] \quad (3.53)$$

$$\Delta \dot{q}_{eff} + \frac{c_{ax,ms}}{c_{b,ax}} \Delta q_{eff} = \frac{c_{ax,ms}}{c_{b,ax}} \Delta q_{in} \quad t \in [t_1, T] \quad (3.54)$$

with discontinuities at 0 and  $t_1$ . Equations 3.53 and 3.54 result in

$$\Delta q_{eff,1}(t) = \Delta q_{in,1} \left[ 1 - e^{-\frac{c_{ax,inj}}{c_{b,ax}}(t)} \right] \quad t \in [0, t_1] \quad (3.55)$$

$$\Delta q_{eff,2}(t) = \Delta q_{in,2} \left[ 1 - e^{-\frac{c_{ax,ms}}{c_{b,ax}}(t-t_1)} \right] \quad t \in [t_1, T] \quad (3.56)$$

The dynamic system depends on  $\Delta q_{in}$  being the difference of the flow quantity at the beginning of the section and the steady state end value. From Figure 3.9 one obtains  $\Delta q_{in,1}$  and  $\Delta q_{in,2}$  to

$$\Delta q_{in,1} = q_{max} - \tilde{q}_{min} \quad (3.57)$$

$$\Delta q_{in,2} = q_{min} - \tilde{q}_{max} \quad (3.58)$$

In Figure 3.9 a steady oscillation is presented which means that the start and end value of the period are equivalent. In general equating a first order linear differential equation one is left with an integration constant that has to be identified from the initial condition. This initial condition affects the transient oscillation but after sufficient time a steady oscillation is performed which does not depend on the initial value. In this work only steady oscillation is considered.

Setting the initial condition to  $\tilde{q}_{min}$  for the system presented in Figure 3.9 the transient oscillation can be skipped and the desired steady oscillation is obtained. Thus  $\tilde{q}_{min}$  has to be derived. For a steady oscillation between the values  $\tilde{q}_{min}$  and  $\tilde{q}_{max}$ , at the end of the jet section  $\tilde{q}_{max}$  and at the end of the main-flow section  $\tilde{q}_{min}$  have to be reached. This implies that the magnitudes of  $\Delta q_{eff,1}(t_1)$  and  $\Delta q_{eff,2}(T)$  have to be equivalent yielding

$$(q_{max} - \tilde{q}_{min}) \left[ 1 - e^{-\frac{c_{ax,inj}}{c_{b,ax}}(t_1)} \right] = (q_{min} - \tilde{q}_{max}) \left[ 1 - e^{-\frac{c_{ax,ms}}{c_{b,ax}}(T-t_1)} \right] \quad (3.59)$$

The value at the end of the first period can be obtained by

$$\tilde{q}_{max} = \tilde{q}_{min} + (q_{max} - \tilde{q}_{min}) \left[ 1 - e^{-\frac{c_{ax,inj}}{c_{b,ax}}(t_1)} \right] \quad (3.60)$$

Substituting equation 3.60 into 3.59 and rearranging yields

$$\tilde{q}_{min} = \frac{q_{max} e^{-\frac{c_{ax,ms}}{c_{b,ax}}(T-t_1)} + q_{min} \frac{1 - e^{-\frac{c_{ax,inj}}{c_{b,ax}}(t_1)}}{1 - e^{-\frac{c_{ax,ms}}{c_{b,ax}}(T-t_1)}}}{e^{-\frac{c_{ax,ms}}{c_{b,ax}}(T-t_1)} + \frac{1 - e^{-\frac{c_{ax,inj}}{c_{b,ax}}(t_1)}}{1 - e^{-\frac{c_{ax,ms}}{c_{b,ax}}(T-t_1)}}}, \quad (3.61)$$

being the value at  $t = 0$  and all following periods  $nT$  where  $n \in \mathbb{Z}$ . Knowing the initial value for the steady oscillation the transient oscillation can be spared which saves time.

In section 3.1 it was found that the Fourier series gives the better match of the unsteady CFD inlet data. In contrast to the non-linear system with Fourier series input signal, a closed form solution can only be obtained for the simple rectangular input signal which makes a numerical solution necessary.

For the validation of the system the input signal is obtained from CFD and thus is a discrete signal. Performing a numerical solution an initial value has to be provided but can't be obtained in closed form. Fourier series as well as the CFD input can be approximated by the rectangular signal. For these two signals no closed solution for the initial value can be found and as the initial value  $\tilde{q}_{min}$  (equation 3.61) derived for the rectangular signal is used. The initial value of rectangular input and Fourier series is not the same thus a transient oscillation results. In order to obtain the steady oscillation several periods have to be computed until the first and last value within the period are equivalent.

Mainly the considerations up to this point were performed using the rectangular input signal. In section 3.1 it was shown that Fourier series suite CFD better. Nevertheless it is obtained from the rectangular signal thus considerations performed for the rectangular signal can generally also be applied to Fourier series.

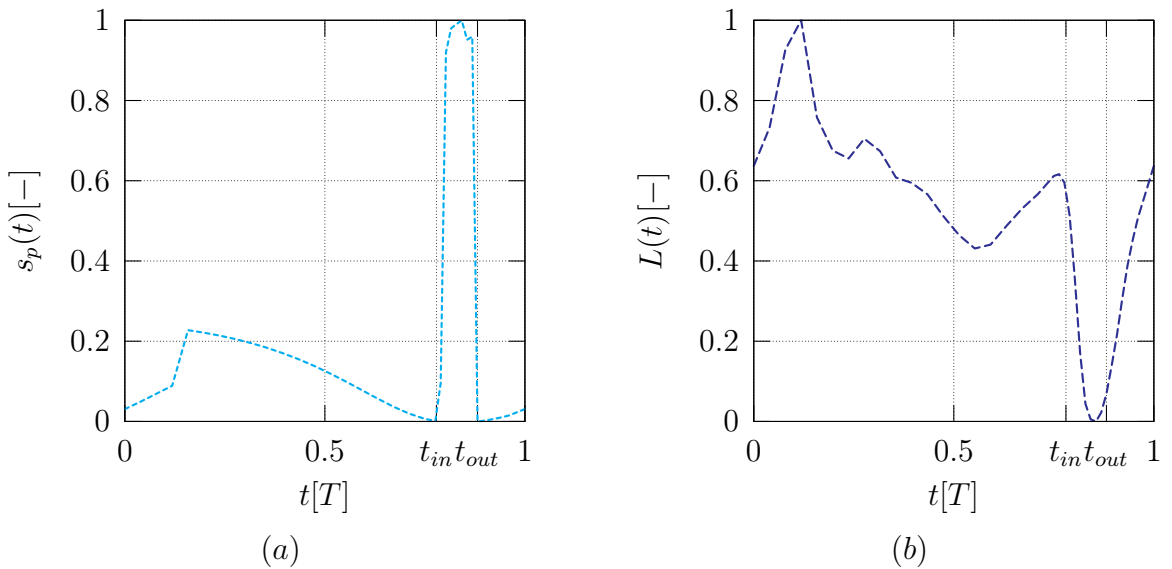


Figure 3.10.: System Verification Data Set: (a) input  $s_p$ ; (b) output  $L$

In order to verify that a first order system can be used to approximate the dynamic system, CFD data is used. Input and output data was provided by Matzgeller [21]. A representative radius (close to the maximum stagnation pressure inside the jet) is chosen at which the system identification is performed. Stagnation point position with respect to leading edge and lift per unit span  $\tilde{L}$  are selected as system input and output respectively. Stagnation point position is defined by

$$s_p = \frac{x - x_{max}}{x_{min} - x_{max}} \quad (3.62)$$

where  $x$  is the distance of the stagnation point along the airfoil to the leading edge and is

positive if the stagnation point is located at blade pressure side.  $x_{max}$  and  $x_{min}$  are the maximum and minimum stagnation point locations respectively. This transformation is performed to get the inlet conditions in a form as presented in section 3.1 (compare  $f(\varphi)$ ). In Figure 3.10 (a) the inlet quantity is shown. The inflow conditions are in good agreement with the rectangular profile and the Fourier series (compare Figure 3.3). Close to the end of the period a peak is apparent which represents a shift in stagnation point and thus the time span where the rotor is affected by tip injection.

In Figure 3.10 (b) the system output is presented. Nondimensional lift is defined in a similar way as the inlet conditions by

$$\tilde{L} = \frac{L - L_{min}}{L_{max} - L_{min}} \quad (3.63)$$

where  $L_{min}$  and  $L_{max}$  are minimum and maximum lift of the blade. At about 90% of the period a negative peak arises that can be related to the change in inlet conditions. A positive peak appears at the beginning of the period and it is caused by the unsteady flow of the adjacent blade (Matzgeller [22]). A dynamic system purely depending on the inlet conditions to the stage can't account for this peak. Emphasis is thus laid on the peak at about 90% period that is the response to the input signal.

Verification of the system is performed by comparing the CFD system output to the output of first order system like suggested by Melick to the CFD input of the form

$$\dot{y}(t) + \frac{1}{\tau}y(t) = ku(t) \quad (3.64)$$

where  $u$  is the input and  $y$  is the output. The system is solved numerically applying central differences

$$y_{n+1} = y_{n-1} + (t_{n+1} - t_{n-1}) \left( ku_n - \frac{1}{\tau}y_n \right) \quad (3.65)$$

using different time constants  $\tau$  and amplification factors  $k$  for jet and main flow. Jet and main flow are identified from the levels of the input signal in a way that for  $s_p \geq 0.5$  (compare Figure 3.10) the jet quantities are used. Changing the time constants and the amplification factors the system is adjusted to meet the peak at about 90% period. In Figure 3.11 the results are presented. Comparing CFD and first order response good matching of the negative peak can be seen. Time constants used for the system are of the same order of magnitude as the constants obtained by Melick. The ratio of the time constants of the jet to the main flow differs by 5%. Hence, a first order system is in good agreement with the negative peak. Considering this model the system dynamics is met reasonable. Better modelling can be performed by including the influence of the adjacent blade. However, the mean value along the period which is important for the work input (discussed in section 3.4) is reproduced in a good way.

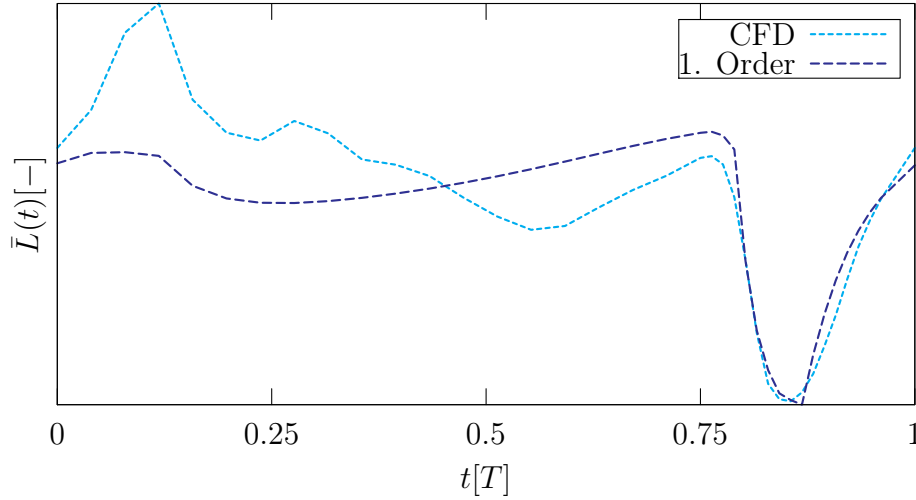


Figure 3.11.: System Verification

### 3.3.3. Summary

In this section various aspects regarding dynamic systems have been discussed. Inlet conditions were obtained in section 3.1 yielding that a good matching of the CFD inflow is obtained by the use of Fourier series:

$$q_{in}(t) = q_{ms} + [q_{inj} - q_{ms}] \sum_{k=0}^9 [a_k \cos(k\omega t) + b_k \sin(k\omega t)] \quad (3.66)$$

System dynamics were captured by effective inlet quantities of the form

$$q_{eff}(t) = q_0 + \Delta q_{eff}(t) \quad (3.67)$$

with

$$\Delta \dot{q}_{eff} + \frac{c_{ax}(t)}{c_{b,ax}} \Delta q_{eff} = \frac{c_{ax}(t)}{c_{f,ax}} \Delta q_{in} \quad (3.68)$$

being the governing differential equation. Equation 3.68 uses the time constant obtained by Melick [24] and was obtained for compressors experiencing inlet distortion. From the identification performed in this section a time constant could have been obtained but only for one particular compressor at one operating point. Nevertheless, performing a system identification for tip injection systems a time constant would be obtained that is expected to enhance the results. However, a high number of experiments would be required for the identification process in order to achieve trustable results. The time constants found in this identification are of the same order of magnitude thus it is assumed that time constant suggested by Melick can be used as well for tip injection.

Equation 3.68 employing the Fourier series as input is solved numerically using central differences yielding

$$q_{eff}(n+1) = q_{eff}(n-1) + [t(n+1) - t(n-1)] \frac{1}{\tau(n)} [q_{in}(n) - q_{eff}(n)] \quad (3.69)$$

where  $n$  is the discrete time. Solving equation 3.69 the values  $n-1$  and  $n$  are required which are not available for the first step thus for the first step backward difference of the form

$$q_{eff}(n+1) = q_{eff}(n) + [t(n+1) - t(n)] \frac{1}{\tau(n)} [q_{in}(n) - q_{eff}(n)] \quad (3.70)$$

is used. The initial value results from equation 3.61.

In the derivation process it was assumed that system dynamics of isolated airfoil and blade row are equivalent. Considering the unsteady thin airfoil theory by Kármán the unsteady effects are due to wake vortices changing the flow field about the airfoil. Also circulations of the adjacent airfoils in the cascade influence the flow field. For the steady case Weinig [33] defined the factor  $k_0$  (see equation 3.30) that gives the impact of the circulation about the adjacent airfoil on the present airfoil in terms of the lift coefficient. Lecht [18] suggested that this constant can be applied to the time constant as well in order to account for the influence of the adjacent blades thus the time constant is changed to

$$\tau(t) = \frac{5.5c_{b,ax}}{k_0c_{m,ax}(t)} \quad (3.71)$$

## 3.4. Implementation

The basic system and ideas about how the dynamic pressure and temperature rise can be accounted for by a first order dynamic system in combination with a steady SCM were presented up to this point. In this section the implementation of this approach into a computer program is discussed.

Two different sets of inlet conditions have been derived. Circumferentially varying inflow conditions were developed in section 3.1 that are called real inflow conditions in the following. In the relative frame of reference those inlet conditions are unsteady, because of the rotor speed. Unsteady inflow conditions can't be treated by a steady tool like SGV. Hence, different inflow conditions that capture the system dynamics were developed in section 3.3. This set of inflow conditions is referred to as effective inflow conditions. Both inflow conditions are generally different. Using the modelled

real inflow conditions the inflow field (i.e. the radial distribution of streamlines) is expected to be correct, but using them a steady work input to the stage is obtained. Effective inflow quantities are expected to give the correct unsteady work, but the inflow field is wrong. Hence, two separate SGV runs are performed. One with effective inflow conditions that is used to obtain the unsteady work and then a SGV run with real inflow conditions, for which the work input of the rotor affected by tip injection is corrected.

The SGV source code is available at MTU so at first it was considered to include the tip injection computation method directly into SGV. High flexibility and best performance would be the advantages of a direct implementation. On the other hand a change of the source code is required which makes the implementation more complex and thus was rejected.

A python script is developed that first reads the required input from a converged SGV solution for the same compressor without tip injection. This baseline computation is used to get the outflow of the stator upstream of the injection (or IGV for injection upstream of the first rotor). Hence the initial flow field for the tip injection calculation is given by the baseline computation and the injected jet is added at the injection location. An additional input file "injection.ein" (described in Appendix A) has to be provided for the script containing the tip injection parameters as well as some flags for program control. Altering the provided SGV input (s2.ein) file for the baseline computation the desired solution with real inflow quantities imposed by tip injection and unsteady work input over the rotor downstream of the injection slot is computed. Before this procedure is presented in a flow chart, SCM specific changes of the developed procedure, averaging and the modification of the input file "s2.ein" are discussed.

Up to now the dynamic system was treated at surfaces of revolutions. SGV uses a grid where the radial direction is resolved by streamlines. In order to obtain the radial profiles of the effective inflow quantities they have to be obtained from the dynamic system for all streamlines inside the jet. Generally the number of streamlines and the ratio of injected mass flow to the main-stream mass flow are small thus the jets remain well inside the first streamtube. Therefore the effective flow quantities are only obtained for the casing streamline and the radial profile of real and effective inlet flow quantities along the jet is assumed to be that at the casing and thus constant.

### Averaging

In section 3.1 the real inlet conditions to the rotor downstream of the injection depending on the angular direction were defined. Effective inlet conditions to this rotor as discussed in section 3.3 depend on the time. Generally the circumference could be discretised and at each point resulting from this discretisation one SGV run could be performed using the real inlet conditions and correcting the work input according to the effective inlet conditions in order to account for injection. But this would require many SGV runs slowing down the process significantly. A more simple approach is achieved by averaging the inlet quantities and then performing just one SGV computation with real inlet conditions and corrected work.

Real inflow conditions are of steady nature and depend on the circumferential position. In order to obtain the correct streamline distribution and the integral correct mean, flux quantities have to be mass averaged. Effective inflow quantities on the other hand are unsteady and in order to obtain the mean of the unsteady work input those inlet quantities have to be time averaged. First mass averaging of the real inflow quantities and then time averaging of the unsteady effective inflow quantities are discussed.

Fourier series were selected as inflow conditions because they represent CFD results well and are time-continuous (see section 3.1). The Fourier series are computed from the rectangular signal. Thus the mean of those two profiles is the same and the mean of the rectangular profile is computed, because a closed solution is easier in contrast to the Fourier series.

Averaging takes place in the angular direction to obtain the radial profiles that are used for SGV. Considering radii less than  $r_{inj}$  (i.e. circumferences positioned completely in the main flow) the angular mass averaged value is the one from the main flow. For radii in the range  $r_{inj}$  to  $r_{cas}$  (i.e. in the section where also jets are present) angular mass averaging is presented in the following.

In Figure 3.12 (a) a ring segment showing one main flow section and its adjacent jet (i.e. periodic unit according to Figure 3.1) on the inlet plane is presented in a view along the axis. The inner radius is  $r_{inj}$  and the outer radius is the casing radius  $r_{cas}$ . The mass flow through the area covered by the jet is given by

$$\dot{m}_{inj} = \rho_{inj} c_{ax,inj} A_{inj} \quad (3.72)$$

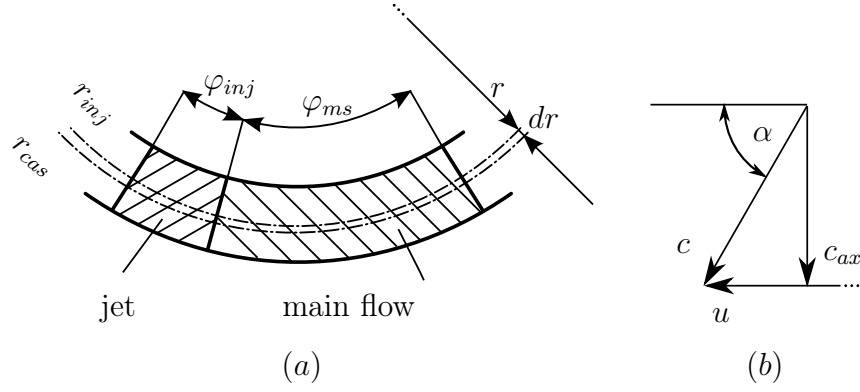


Figure 3.12.: View along the Compressor Axis on the Inlet Plane

where  $c_{ax,inj}$  is obtained from (compare Figure 3.12 (b))

$$c_{ax,inj} = c_{inj} \sin \alpha_{inj} \quad (3.73)$$

with  $\rho_{inj}$ ,  $c_{inj}$  and  $\alpha_{inj}$  are density, absolute velocity and absolute flow angle respectively. For the main flow equivalent consideration yields

$$\dot{m}_{ms} = \rho_{ms} c_{ax,ms} A_{ms} \quad (3.74)$$

and

$$c_{ax,ms} = c_{ms} \sin \alpha_{ms} \quad (3.75)$$

evaluated with main flow quantities. The area of the jet and main flow for a infinitesimal thin ring segments in one periodic unit are given by (compare Figure 3.12 (a))

$$dA_{inj} = 2\pi r \varphi_{inj} dr \quad (3.76)$$

and

$$dA_{ms} = 2\pi r \varphi_{ms} dr \quad (3.77)$$

respectively.

The mass averaged mean of an arbitrary flow quantity  $q$  along the angular direction for the infinitesimal thin ring segment is obtained by:

$$\bar{q}_m = \frac{q_{inj} \dot{m}_{inj} + q_{ms} \tilde{m}_{ms}}{\dot{m}_{inj} + \dot{m}_{ms}} \quad (3.78)$$

Substituting equations 3.72, 3.74, 3.76 and 3.77 into 3.78 and simplification yields

$$\bar{q}_m = \frac{q_{inj} \tilde{m}_{inj} + q_{ms} \tilde{m}_{ms}}{\tilde{m}_{inj} + \tilde{m}_{ms}} \quad (3.79)$$

with

$$\tilde{m}_{inj} = \rho_{inj} c_{ax, inj} a_{inj} \quad (3.80)$$

and

$$\tilde{m}_{inj} = \rho_{ms} c_{ax, ms} (1 - a_{inj}) \quad (3.81)$$

using  $a_{inj}$  as defined in equation 3.5.

The unsteady work is obtained by unsteady effective inflow conditions that have to be averaged with respect to time. Generally the time averaged value of flow quantity  $F$  in a period  $T$  is given by

$$\bar{F}_t = \frac{1}{T} \int_0^T F(t) dt \quad (3.82)$$

Using the numerical solution procedure of the dynamic system the time has to be discretised in an arbitrary number  $n$  of intervals with index  $k \in [0, n]$  and thus  $F$  is available at this discretised time values. Applying the trapezoidal rule to equation 3.82 the time averaged value is computed by:

$$\bar{F}_t = \frac{1}{T} \sum_{k=0}^n \frac{F_k + F_{k+1}}{2} (t_{k+1} - t_k) \quad (3.83)$$

### Prescription of Radial Profiles

For SGV with a common number of streamlines the radial extension of the jet is significantly smaller than the height of the first stream tube. Therefore, it is sufficiently accurate to obtain the averaged conditions valid for the whole jet using flow properties at the casing only. These values are used for the whole jet in

Averaging yielded the real and effective inlet conditions that have to be prescribed using the SGV inlet file which is not straight forward and thus thoroughly discussed in the next paragraphs.

SGV interpolates the required values for the computation from the the radial profiles provided in the input file "s2.ein" on the streamline position. In contrast to CFD the grid for SGV is coarse because it only consists of few streamlines and calculation planes (compare chapter 2). Therefore it can not be assumed that interpolating the desired radial profile with its infinite radial gradient at  $r_{inj}$  on the streamline position using either linear or splines interpolation is sufficiently accurate. Hence, a different approach has to be developed to prescribe the profiles to the SGV input file.

In Figure 3.13 (a) the influence of the streamline position on linear interpolated radial profiles is presented. On the abscissa the dimensionless radius defined by

$$r = \frac{R - R_{hub}}{R_{casing} - R_{hub}} \quad (3.84)$$

where  $R$ ,  $R_{hub}$  and  $R_{casing}$  are the radii at actual position, hub and casing respectively, is plotted. Along the ordinate,  $f(r)$  defined by

$$f(r) = \frac{q(r) - q_{ms}(r)}{q_{mean}(r) - q_{ms}(r)} \quad (3.85)$$

where  $q$ ,  $q_{ms}$  and  $q_{mean}$  are flow quantities at actual radial position, in the main stream and in the mean of the inlet profile for radii greater than  $r_{inj}$  respectively, is plotted. Hence,  $f(r)$  is the difference of quantity  $q(r)$  to the main flow with respect to the difference of the quantities mean value for radii greater than  $r_{inj}$  and main-flow. Therefore  $f(r)$  is 1 in the range  $r \in [r_{inj}, 1]$  and 0 in the range  $r \in [0, r_{inj}]$ . In Figure 3.13 (a) this profile is represented by  $f_{id}(r)$ . Generally, the extension of the jet is such, that only the

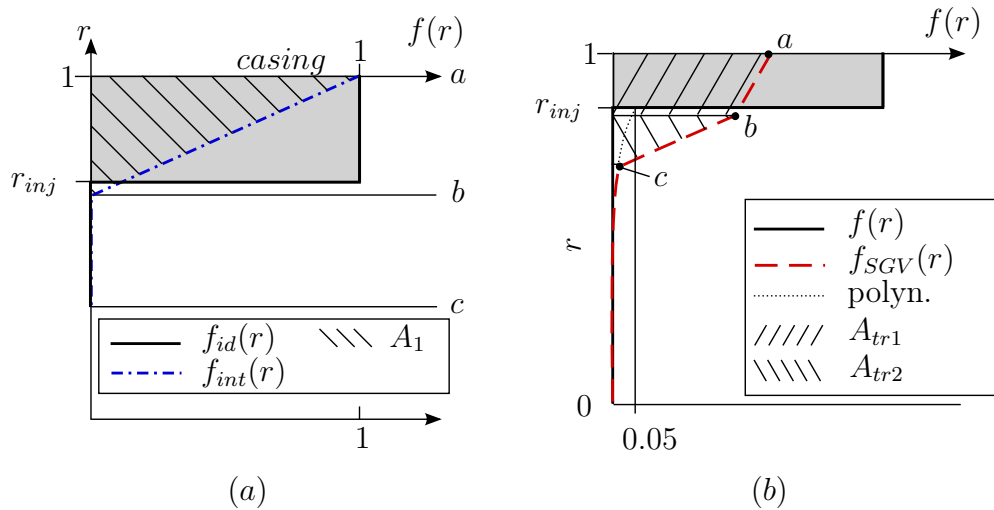


Figure 3.13.: Prescription of the Radial Profile: (a) Profile obtained by Interpolation; (b) Profile used for SGV input file

casing streamline (streamline  $a$  in Figure 3.13 (a)) is located inside the radial segment affected by the jet and all other streamlines ( $b$ ,  $c$ ..) are outside. Linear interpolation of the radial profile  $f_{id}(r)$  on the streamline position yields the profile  $f_{int}(r)$ . At the casing streamline  $a$  it takes the value 1 and the value at all other streamlines ( $b$ ,  $c$ ..) is 0.

Integrating  $f_{id}(r)$  along the radial direction the integral difference of  $q_{mean}$  and  $q_{ms}$  is obtained. Comparing the integrals (i.e. areas under the curves with respect to the radial axis) one can easily see that a big difference of the integrals of  $f_{int}(r)$  and  $f_{id}(r)$

is present. Hence, interpolation of the radial profile prescribes the a wrong integral value of the radial profile using a common streamline distribution. The problem about simple interpolation of the profile is the radial gradient at the boundary between jet and main-flow ( $r_{inj}$ ). In order to resolve this gradient properly several streamlines would have to be placed near this gradient. This would yield a profile being close to the values of desired profile  $f_{id}(r)$  and a similar area. For streamline curvature computations more streamlines are decreasing the accuracy of the method, once a certain number is exceeded [34]. Using common numbers of streamlines that generally give good accuracy of SGV this gradient can't be resolved.

As pointed out above the profile has to be developed to fulfil the integral mean value of the profile  $f_{id}(r)$ . In order to achieve this, the streamlines are first categorized in two groups regarding their position with respect to  $r_{inj}$ . All streamlines inside the jet (i.e  $r \in [r_{inj}, 1]$ ) and the first streamline below the jet give the "jet" streamline group. For the interpolated profile  $f_{SGV}(r)$  in Figure 3.13 (b) this means that streamline  $a$  and  $b$  are in the jet category and streamline  $c$  and all streamlines below  $c$  are in main flow category.

The general idea is to set the  $f(r)$ -value for streamlines belonging to the "main-flow" group to 0 and compute the  $f(r)$ -values for streamlines in the "jet" group to meet the area under the profile  $f_{id}(r)$ . SGV interpolates flow quantities from the prescribed values to the streamline distribution using spline interpolation. The steep radial gradient at  $r_{inj}$  leads to wiggles if not resolved properly by the streamlines. Placing sufficient number of streamlines in the annulus to resolve this gradient though is known to be negative for the accuracy of the SCM and thus not performed. In order to minimize these wiggles values belonging to the "main flow" group are not set to 0 but a polynomial of the form

$$f(r) = 0.05 \left( \frac{r}{r_{inj}} \right)^8 \quad (3.86)$$

is used (compare Figure 3.13 (b)). The polynomial is defined in a way that it passes through the points  $(0, 0)$  and  $(0.05, r_{inj})$ . The power 8 as well as 0.05 for the profile value are chosen arbitrarily in a way that a smooth shape for common profiles results. Using the trapezoidal rule the area under main flow section is computed by

$$A_{ms} \approx \sum_{k=1}^{n_c} [r_k - r_{k-1}] \frac{f_i(r) + f_{i-1}(r)}{2} \quad (3.87)$$

and then subtracted from the area under  $f_{id}(r)$  yielding the area under the upper

segments

$$A_{jet} = h_{inj} \times 1 - A_{ms} \quad (3.88)$$

The jet category is approximated by a trapezoid. Using a trapezoid a defined slope to the casing is generated and thus the gradient to the casing is limited. Steep radial gradients particularly to the casing often yield numerical problems in SGV which is avoided by this choice. Two trapezoids compose the area under the jet category and the area between the top most streamline in the "main-flow" group and first streamline below the jet thus the area is given by

$$A_{jet} = A_{tr1} + A_{tr2} = [1 - r_{n-1}] \frac{a + b}{2} + [r_{n-1} - r_{n-2}] \frac{b + 0.05}{2} \quad (3.89)$$

(compare Figure 3.13 (b)) where  $n$  is the number of streamlines.  $a$  and  $b$  are the desired quantities and in order to obtain them the ratio of them defined by

$$k = \frac{a}{b} \quad (3.90)$$

is introduced and substituted into equation 3.89. Rearranging yields

$$b = \frac{2A_{jet} - 0.05(r_{n-1} - r_{n-2})}{(1 + k)(1 - r_{n-1}) + (r_{n-1} - r_{n-2})} \quad (3.91)$$

and

$$a = kb. \quad (3.92)$$

$k$  is proportional to the slope of the profile to the casing.

As mentioned above the first streamline outside the jet is allocated to the "jet" group. Generally the number of streamlines is not sufficient to place two streamlines inside the jet. If this streamline would not be added to the "jet" group only the value of the profile at the casing streamline would be computed to fulfill the same area under  $f_{SGV}(r)$  and  $f_{id}(r)$ . Therefore, this value would be bigger than one which implies that the desired prescribed mean value would be exceed and additionally a steep gradient to the casing would be introduced yielding numerical problems. In order to prevent this, the above discussed profile is used.

In Figure 3.14  $f(r)$ -profiles obtained using the described method for two different numbers of streamlines are computed. Profile  $f_1$  has got the streamline distribution that is apparent in common SGV calculations. In order to achieve the right integral value the magnitude of the profile is decreased. A higher number of streamlines (compare profile  $f_2$  in Figure 3.14) improves the prescribed profile because the radial resolution is better.

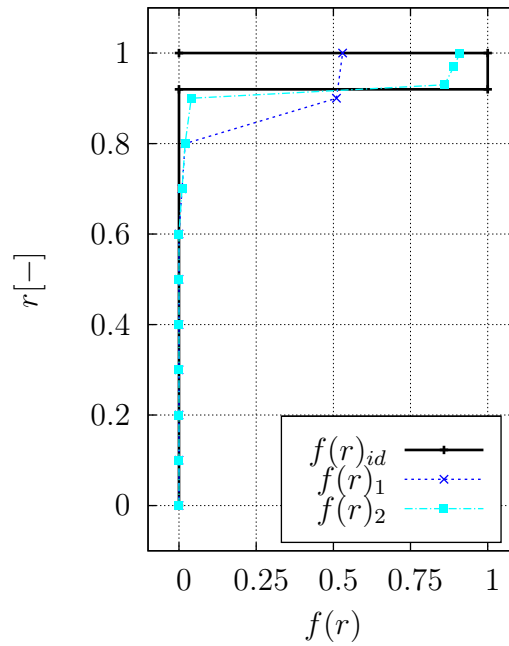


Figure 3.14.: Profiles created according to the presented Method with different Stream-line Resolution around  $r_{inj}$

### Obtaining inflow quantities for the Dynamic System

In section 3.1 the time dependent inflow conditions in terms of stagnation pressure, stagnation temperature and flow angle in the absolute frame of reference were discussed. For the dynamic system inlet conditions in terms of velocity and flow angle in the relative frame of reference and density are required (as shown in section 3.3). Using these inlet conditions effective inlet conditions are computed in the form of relative flow velocity, relative flow angle and density. As pointed out later in the SGV input file absolute stagnation pressure, absolute stagnation temperature and absolute flow angle can be altered. Thus the effective inflow quantities obtained from the dynamic system have to be transformed back. In the following this process is discussed.

Rearranging equation 3.3 yields

$$p_{t,LE} = p_s + (p_{t,inj} - p_s) c_d \quad (3.93)$$

the actual stagnation pressure at rotor leading edge where  $p_s$  is the static pressure in the main flow at the casing and  $p_{t,inj}$  is the stagnation pressure upstream of the nozzle. Using the isentropic relations the Mach number [6] is obtained by

$$M = \sqrt{\frac{2}{\gamma - 1} \left[ \left( \frac{p_{t,tat}}{p_s} \right)^{\frac{\gamma-1}{\gamma}} - 1 \right]}. \quad (3.94)$$

In the SGV solution file the static pressure at IGV outlet is provided which is used to obtain the Mach number. Generally as discussed in section 3.1, from the IGV to the location of the injection the main-flow accelerates due to the reduced annulus cross sectional area because of the jets. Nevertheless, because the nozzles are supposed to be choked for common tip injection configurations the jet velocity does not change for the expected variation of static pressure.

Using isentropic relations the static temperature equates to

$$T_s = T_{t,inj} \left( \frac{p_s}{p_{t,tat}} \right)^{\frac{\gamma-1}{\gamma}} \quad (3.95)$$

Density can be obtained from the ideal gas law by

$$\rho = \frac{p_s}{RT_s} \quad (3.96)$$

The absolute flow velocity of the jet can be obtained from the definition of Mach number and speed of sound by:

$$c = M\sqrt{\gamma RT_s}. \quad (3.97)$$

The actual flow angle in the absolute frame of reference is obtained in a similar way to the actual stagnation pressure from equation 3.4

$$\alpha_{tat} = \alpha_{inj} - (\alpha_{inj} - \alpha_{ms}) c_\alpha. \quad (3.98)$$

Relative flow quantities are obtained from the absolute ones by transformations according to velocity triangles. These relations are presented in a general form and can be applied to any velocity triangle under consideration. In Figure 3.15 a velocity triangle is presented where  $u$  is the blade speed,  $c$  and  $\alpha$  are absolute velocity and angle and  $w$  and  $\beta$  are relative velocity and angle respectively.

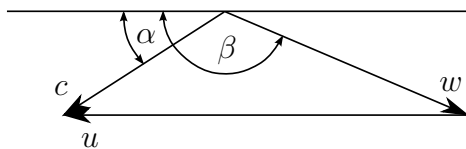


Figure 3.15.: Velocity Triangle

Knowing

- blade speed  $u$
- absolute velocity  $c$

- flow angle in absolute system  $\alpha$

the relative velocity can be obtained from the cosine law as (compare Figure 3.15)

$$w = \sqrt{c^2 + u^2 - 2cu \cos \alpha}. \quad (3.99)$$

Using the sine rule the flow angle in the relative system equates to

$$\beta = \pi - \arcsin\left(\frac{c}{w} \sin \alpha\right) \quad (3.100)$$

These quantities are now used with equations 3.42, 3.44 and 3.47 to obtain the effective inlet quantities.

### Effective Stagnation Pressure, Temperature and flow angle

The effective inlet conditions for the dynamic system were obtained in the relative frame of reference. As pointed out, later only absolute stagnation pressure, stagnation temperature and flow angle can be adjusted in the SGV input file. Thus the relative effective quantities have to be transformed to those quantities. First the relations are developed in a general form and then they are applied to the particular case.

First the relative effective flow quantities are transformed into the absolute system. Knowing

- blade speed  $u$
- relative velocity  $w$
- flow angle in relative system  $\beta$

the absolute velocity can be obtained from the cosine law as (compare Figure 3.15)

$$c = \sqrt{w^2 + u^2 - 2wu \cos(\pi - \beta)}. \quad (3.101)$$

Using the sine rule the flow angle in the absolute system equates to

$$\alpha = \arcsin\left(\frac{w}{c} \sin(\pi - \beta)\right). \quad (3.102)$$

The desired values are computed from the absolute quantities. Effective static Temperature equates from the ideal gas law to

$$T_{s,eff} = \frac{p_s}{R\rho_{eff}} \quad (3.103)$$

Using the effective absolute flow velocity the Mach number of the flow is computed according to

$$M_{eff} = \frac{c_{eff}}{\sqrt{\gamma R T_{s,eff}}} \quad (3.104)$$

From the absolute Mach number the effective stagnation pressure is obtained

$$p_{t,eff} = p_s \left[ 1 + \frac{\gamma - 1}{2} M^2 \right]^{-\frac{\gamma}{\gamma - 1}} \quad (3.105)$$

Using isentropic relations the effective stagnation temperature equates to

$$T_{t,eff} = T_{s,eff} \left[ \frac{p_{t,eff}}{p_s} \right]^{-\frac{\gamma - 1}{\gamma}} \quad (3.106)$$

### Interaction of SGV and the python program

In order to achieve the desired flow field for tip injection according to the above considerations input quantities have to be adjusted in the SGV input file. In section 3.1 the inlet conditions that are present in the annulus were discussed. Effective inflow quantities that give the correct dynamic work input to the stage were derived in section 3.3. Generally those two inlet conditions are not equal and therefore two separate SGV runs are performed. Using the real inlet conditions the modelled inflow altered by tip injection is obtained but the steady work input would be computed by SGV and thus the outflow conditions of the rotor are wrong. Also the losses and thus the stagnation pressure rise that would arise due to the steady work are obtained differs from the unsteady one.

Generally, SGV computes the flow field in the compressor using the given inlet conditions at the rotor front face, i.e. the first calculation plane. In the following the desired changes of the inflow to the rotor and the work input of the rotor downstream of the injection are presented along with the values that have to be adjusted in the SGV input file:

- *Inlet conditions:* As mentioned at the beginning of this section 2 different SGV runs have to be performed where radial profiles of following flow quantities ahead of the rotor downstream of injection have to be prescribed:
  - *Stagnation Pressure:* Stagnation pressure upstream is changed by modification of the stagnation pressure loss coefficient of the upstream blade row in order to account for the altered stagnation pressure due to tip injection at rotor inlet. From SGV the inlet conditions of the upstream blade row are known so that according to equation 2.3,  $\omega$  is adjusted to meet the desired stagnation pressure at row outlet.
  - *Stagnation Temperature:* At every calculation plane a temperature difference can be prescribed and thus the desired stagnation temperature can be

set.

- *Absolute flow angle*: The outflow angle of the upstream blade row is adjusted.
- *Mass Addition*: Injected mass flow has to be added to the main flow. In order to account for bleed mass flows the percentage of the main mass flow can be specified at the calculation plane at which the bleed is located. Using a negative value mass is added to the main flow to the casing streamtube.
- *Dynamic Work*: For the final SGV run with corrected work input for the rotor the unsteady work and losses have to be prescribed:
  - *Work Difference*: According to the Euler equation 3.1 the work input is the difference between the products of blade speed and circumferential component of the absolute flow velocity at rotor outlet and inlet respectively. The blade speed is fixed thus that either the circumferential component of the absolute velocity at inlet or outlet has to change.

At inlet the mass-averaged inlet conditions give the integral mean thus the inlet conditions are assumed to be correct. Therefore, the different work input can just be a result of a different circumferential component at rotor outlet for steady and unsteady work. It is not apparent if this change in circumferential velocity at rotor outlet is due to a change of the outflow angle or the flow velocity. However, only the outflow angle can be adjusted thus the different work input has to be realized using the outflow angle.

Rearranging the Euler equation the outflow angle can be obtained using the actual flow velocities by

$$\beta_2 = \pi - \arccos \left[ \frac{u_2^2 - W - u_1 c_{1u}}{u_2 w_2} \right] \quad (3.107)$$

where subscript 1 and 2 denote inlet and outlet conditions respectively,  $W$  is the unsteady work input and  $u$ ,  $w$  and  $c_u$  are blade speed, relative velocity and circumferential component of the absolute velocity respectively. According to equation 3.107 the outflow angle is computed from the flow quantities due to steady work input. Because of the changed work input the outflow velocity changes. Further, it is not accounted for the deviation correlation in equation 3.107. Hence, the outflow angle  $\beta_2$  depends on results of the computations such this is an iterative process.

- *Effective Loss*: For the annulus segment that is affected by tip injection the

losses obtained using effective inlet conditions and for the remainder losses computed using real inlet conditions are used. The stagnation pressure loss coefficients are adjusted in order to account for the changed losses.

The flow field for SGV computations with and without injection changes considerably. Prescribing the values obtained using the considerations performed in this chapter commonly yields no convergence because the changes are too high. Therefore, relaxation is used. The relaxation factor is defined by

$$r = \sqrt{\frac{i}{n}} \quad (3.108)$$

where  $n$  is the number of relaxations. Using this form of relaxation the change for later relaxations are smaller than in the beginning. Relaxation is applied to stagnation pressure, stagnation temperature, injected mass flow and flow angle at the same time such that a smooth change is achieved. It is only performed for the two SGV runs where the inflow quantities are changed but the work input is not corrected.

### Tip injection computation method flow chart

In this chapter the single aspects of the tip injection computation method were developed. Now the single pieces are put together and the program is presented in a flow chart. Ahead of the injection the main flow as well as the jet quantities have to be known. Jet quantities have to be provided in a separate file (`injection.ein`) that is thoroughly discussed in appendix A. Main flow quantities are obtained from a converged SGV (`s2.ein`) run having the same inlet conditions at the front face as the tip injection computation. In the desired working directory the `"input_folder"` has to be created and the input files (`injection.ein` and `s2.ein`) have to be placed in it. Then the tip injection method can be executed.

Above considerations are realized in a python program that is presented by the means of this flow chart. In this flow chart only the main steps are presented in order to understand the working principle. The program procedure is discussed in more detail in appendix B:

1. *Organisation*: First the file `"injection.ein"` is read to get the required additional input. Then the folder structure containing following directories is created automatically.
  - *working\_folder*: in this folder the SGV executable is placed and all SGV runs are performed in there

- *eintritt (engl: entry)*: in this folder files regarding the computations with real inflow quantities are placed
- *delta*: in this folder files regarding the computations with effective inflow quantities are placed
- *run*: in this folder files regarding the computations with real inflow quantities and corrected work are placed

and the SGV solver is copied to the "working\_folder"

2. *SGV pre-run*: A pre-run with the provided s2.ein is performed to check if the file is valid and to obtain the result file s2.ges.lst
3. *Main stream quantities*: All required main flow quantities are extracted from the SGV result file (s2.ges.lst)
4. *Real inflow conditions*: Using the main flow quantities and the jet values provided in the file injection.ein the Fourier series inflow conditions as derived in section 3.1 are computed. All values are extracted from the casing streamline.
5. *Effective inflow quantities*: Real inflow quantities are first transformed to the relative quantities. Effective quantities are obtained as discussed in 3.3 and then transformed back to give effective stagnation pressure, effective stagnation temperature and effective absolute flow angle.
6. *Averaging*: In order to obtain the mean steady work the effective and real quantities are averaged
7. *SGV run with effective inlet quantities*: Unsteady work is obtained by performing a SGV computation using effective inlet quantities.
8. *SGV run with real inlet conditions*: In order to obtain a start solution for the iterative process used to obtain final solution, a SGV run with real inflow conditions is performed. The flow field resulting from this computation already has the correct inlet condition to the rotor downstream of the injection, but the work input is the steady work input as computed by SGV
9. *Check Convergence*: If the solutions for effective and real inlet conditions are converged the iterative process for the final solution is started.
10. *Corrected Work*: Starting from the solution with real inlet condition and the blade outlet angle is adjusted in a way to give the unsteady work as discussed in this section. This process is iterative.

11. *Post Processing*: If the solution converged a summary file is written and plots presenting the effects of tip injection are created.

# Chapter 4.

## Results

A tip injection computation method was developed in chapter 3. In order to validate the functionality of this method, it is applied to a test compressor and the results are presented in this chapter along results obtained from compressor tests. Test results with and without tip injection (referred to as injection and baseline (BL) in the following) are available which show the influence of tip injection on the compressor. Before the influence of tip injection can be investigated the baseline solution has be met. An existing SGV design modelling the test compressor is available but the results don't comply with test baseline results. Thus this solution is first adjusted as presented in section 4.1 to give a better match of the test baseline results. Finally the effects of tip injection for test and SGV are compared to each other to validate the method in section 4.2.

### 4.1. SGV Baseline Computation

First the steps that have to be performed to adjust an existing design calculation to meet the measured compressor maps along with the resulting solutions are discussed. Finally the baseline characteristics are compared to test data.

#### **Straightening of Hub and Casing Contour**

In the existing SGV design the contour is specified with all contour details (e.g. waterfalls). As discussed in the following these details can't be resolved by the calculation grid. Thus the hub and casing contour are straightened in order to increase the accuracy of the method.

The annulus is defined by two splines employing multiple user specified contour points for hub and casing respectively. The number of points for the original design file results from resolving the annulus geometry for CFD. In SGV casing and hub contour are used as the outer streamlines. As described in chapter 2 between hub and casing the other streamlines are placed and their quasi-orthogonal position is computed along the calculation planes. For one streamline its point at each calculation plane are used to built a spline. Hence, because the number of computation planes is smaller than the number of contour points the hub and casing streamline can resolve more details than the other streamlines in the meridional direction.

In Figure 4.1 a sample section of the casing streamline along with its adjacent streamline is presented in a meridional view. In order to resolve contour details at the casing

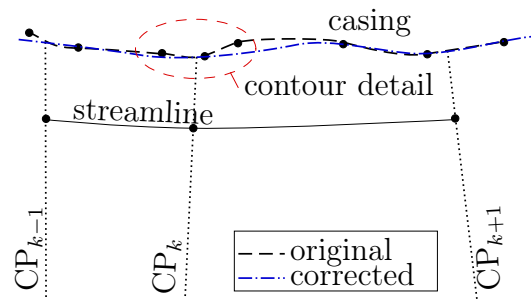


Figure 4.1.: Contour Correction

around these details several contour specification points were put closely together in the meridional direction. The high number of specification points is required to resolve the locally high curvature. This curvature can't be resolved by the streamline adjacent to the casing because of the axial distance of the calculation planes. This has a negative effect on the accuracy of the method. Thus this locally high curvature at hub and casing are decreased by changing the specification points of the contour.

According to best practice guide [2] streamline curvature of the casing should not exceed  $50m^{-1}$  significantly for computations with SGV. On the other hand casing geometry should be resolved in a good way. In the process of straightening the casing it is cared that the maximum curvature of the casing is less than  $50m^{-1}$  and that the casing specification points represent the casing curvature from one calculation plane to another rather than the local curvature and thus contour details.

Adjusting the contour some points are removed and other points are moved slightly in order that the same intersection points of either hub and casing with the calculation planes are obtained. Further it is tried to keep the overall shape of the compressor annulus as closely to the original as possible.

## Rotating Stall

From test data it is known that even if the compressor does not surge at the first rotor rotating stall appears if no form of tip injection is applied (Matzgeller [22]). In section 2.2 it is pointed out that SCM is inviscid thus losses are correlated. Rotating stall however is a viscid phenomena and can not directly be predicted by the SCM. Loss correlation do not account for rotating stall phenomena either.

In order to identify the onset of rotating stall by SCM the main aspects of rotating stall are summed up. A more detailed view on rotating stall can be found in [5]. In Figure 4.2 rotating stall is presented in a circumferential plane. As soon as this

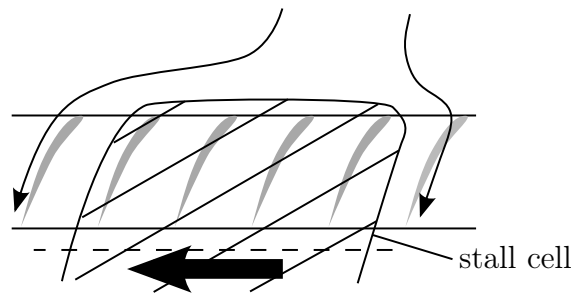


Figure 4.2.: Rotating Stall

phenomena arises a number of blades start to stall. Therefore, the axial velocity for these blades decreases significantly. Flow approaching this section is by-passed since the free flow area is reduced. Hence, rotating stall acts like circumferentially distributed blockage. According to Figure 4.2 incidence for blades left of the stall cell is increased because of the flow deflection due to the stall cell yielding higher blade loading. Blades to the right are less loaded due to this effect. This implies that blades to the left will stall whereas the flow at the right hand side is stabilized and the blades return from stall. Hence the stall cell moves in the right direction.

Further the mean axial velocity through the not stalled section is increased because part of the annulus is blocked by the stall cells. Therefore, the mean incidence is decreased and not stalled parts of the blade row are generally less loaded because the incidence is decreased.

As shown, rotating stall is a circumferential phenomenon and thus can't be computed by an axisymmetric tool like SGV. However, for highly throttled states SGV results show an effect similar to rotating stall presented in the following. This effect commonly yields a high increase of the losses. Thus a particular aspect about the loss correlations has to be discussed before the phenomenon is presented. As discussed in section 2.2

the profile off-design losses are computed from an exponential relation to the range parameter (i.e. incidence). This implies that the profile off-design losses increase exponentially with the incidence. In reality this is not exactly true. For high incidences the losses saturate and to cover this, a loss limiter is included. This limiter is a constant value that can be adjusted by the user. Hence, if the incidence increases about a certain critical incidence where the losses are equal to the limiter a further increase in incidence yields no increase in losses anymore.

For highly throttled states, SGV shows a phenomenon where the losses suddenly increases and is commonly limited by the user defined limiter. Along with this a sudden decrease in the axial velocity and absolute flow angle at the casing streamline occurs as presented in Figure 4.3 (a) and (b). The work input at the casing streamline is increased due to this effect because the resulting circumferential component of the

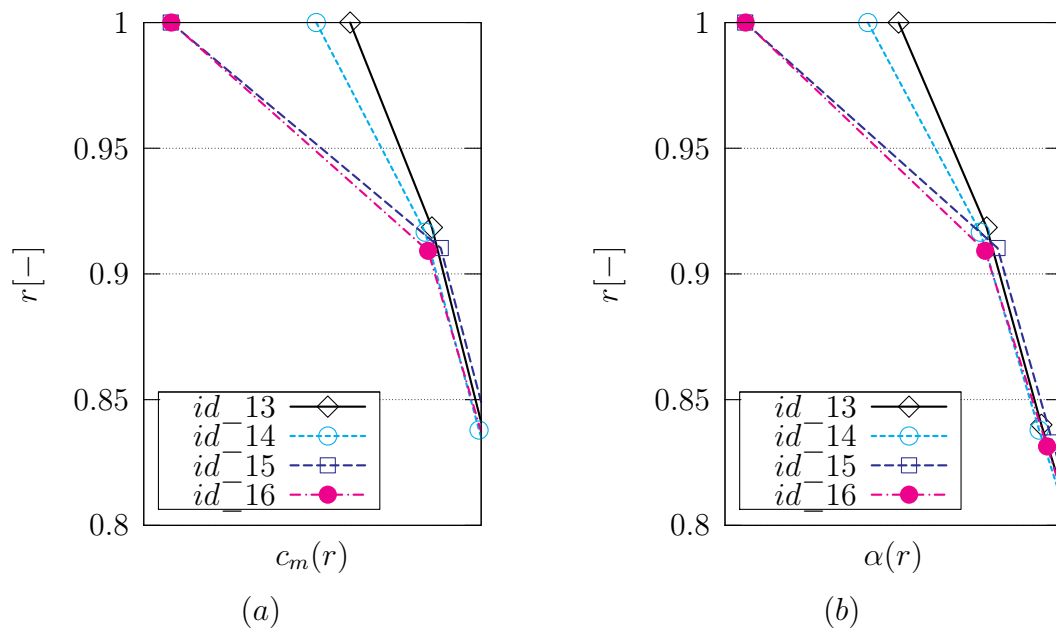


Figure 4.3.: Rotating Stall Analogy: (a) Axial Velocity  $c_m$ ; (b) Absolute Flow Angle  $\alpha$

axial velocity  $\Delta c_u$  increases. The stagnation pressure ratio drops because the losses across the row rise significantly. Comparing rotating stall and the behaviour of a SCM for highly throttled states both show a decrease in axial velocity and increased losses. Like for rotating stall the streamline below the casing is unloaded because of the decreased incidence. Therefore it is assumed that when this phenomena occurs the rotor experiences rotating stall. But the SCM phenomena does not have any circumferential stall cells as apparent in reality.

### Area Averaging vs. Mass Averaging

Stator Leading edge instrumentation was installed on the test rig (see PVD [26]). These data are used to validate the SGV solution to the test. Using the mean of stator leading edge test data (stagnation temperature and stagnation pressure) quasi-stage characteristics can be obtained. Quasi-stages are composed by the rotor and its preceding stator such that the first quasi-stage consists of the inlet guide vane (IGV) and the first rotor. To represent the integral work input of the quasi-stage the measured profiles of stagnation pressure and stagnation temperature have to be mass averaged. However, from the test data the mass flow distribution is not apparent. Therefore commonly these quantities are area averaged. In Figure 4.4 the stage stagnation pressure ratio of

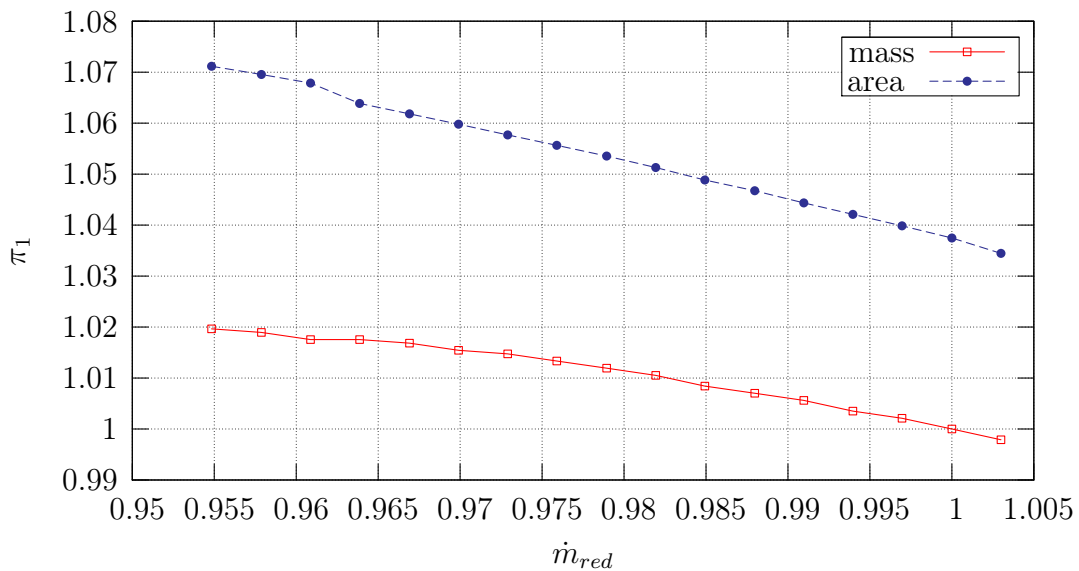


Figure 4.4.: First quasi-stage Stagnation Pressure Ratio: Comparison of Mass and Area Averaged Ratios

the quasi-stage 1 is plotted versus the reduced mass flow at quasi-stage inlet employing 2 different averaging methods. The area averaged characteristic is plotted versus the mass averaged characteristic. All quantities are normed with the working line point of the mass averaged curve. The change of the characteristic is significant. Thus in order to compare test data to results obtained by a SCM mass averaged characteristics can't be used but the radial profiles have to be area averaged.

### Adaption of the Original Design Solution

SGV is used in preliminary design and thus has to be a fast method. In order to obtain this fast method several simplifications are performed. Using correlations it is tried to

correct some of the modelling errors. These correlations though are commonly semi-empirical and represent a variety of compressor test. In order to adjust them, factors that work on the correlations can be adjusted. Also effects like casing boundary layers can't be computed and blading sometimes is adjusted to give better results in these areas. Hence, the design solution does not meet the characteristics using the default factors for the correlation. In order to meet test data the original SGV design is adjusted as presented in the following. As pointed out in chapter 2 in the design case stagnation pressure rise and degree of reaction in conjunction with loss correlations are used to obtain the blade angles. Assuming that stagnation pressure ratios and degree's of reaction of test and SGV are the same in the design case the only adjustment possibility are the loss correlation factors. Adjusting these factors the design solution is adapted to meet the test characteristics satisfactorily. Further the stagnation pressure ratios are radially adjusted at hub and casing but the overall stage stagnation pressure rise held constant.

Tip injection is applied between IGV and the first rotor, thus it has its biggest impact on the first rotor. In order to benchmark the correlation, particularly the first rotor is of interest. This rotor together with the IGV composes the first quasistage. IGV losses are not correlated but prescribed from a CFD computation [21]. The IGV outflow angle computed of SGV and CFD are not significantly different and thus the deviation of the IGV is assumed to be correct. Assuming that CFD results of the IGV are correct in the first quasi stage only the first rotor causes the difference of SGV and test characteristics. Hence, the rotor has to be adjusted to meet the characteristics which allows for a good match. For all other rows the adjustment process bears the problem that only one stage characteristic is available to adjust 2 rows yielding some uncertainties.

### **Baseline Characteristics**

Validation is performed at 90% relative reduced rotor speed. Throttling lines and the following results are compared at this reduced rotor speed. In the test the radial profile of stagnation pressure was measured at a position upstream of the IGV. This plane is located downstream of the swan-neck. The SGV computation domain inlet is placed at this plane thus the stagnation pressure profiles at this location are prescribed as inlet condition to SGV. In Figure 4.5 the stagnation pressure ratio of the baseline compressor of the first quasi-stage is plotted versus the reduced mass flow at quasi-stage inlet. The SGV results are plotted versus test results. All quantities of each

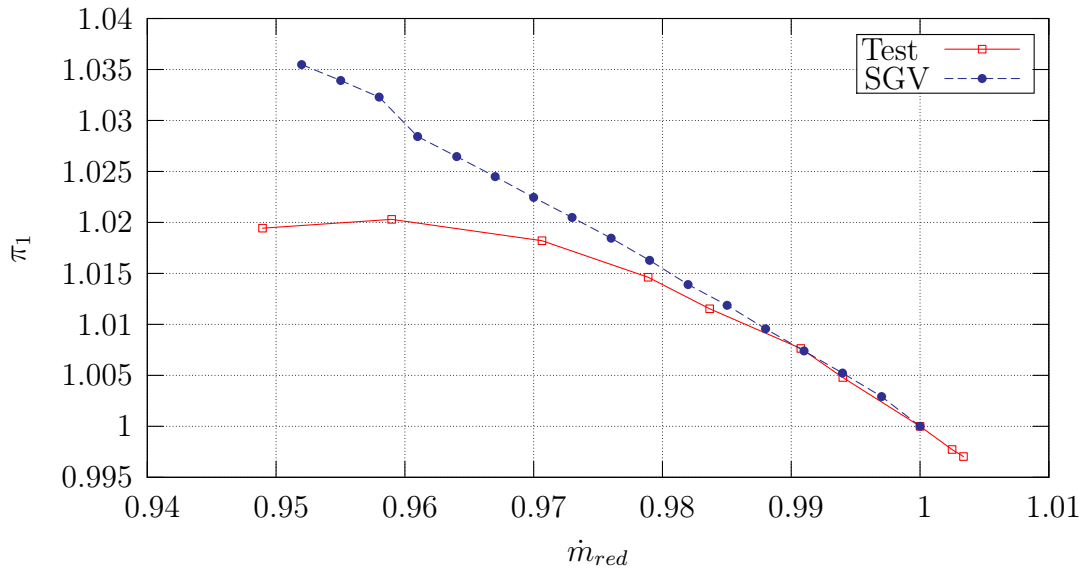


Figure 4.5.: Quasi-Stage 1 Characteristics of SGV Baseline Compressor at 90%  $n_{red}$

characteristics are normed with the working line point of it. As mentioned earlier for tip injection stall of the blades particularly that one affected by tip injection and surge of the compressor are of interest. Stall of the blade row (i.e. the phenomena assumed to be similar to rotating stall) occurs at the changed slope at a normed  $m_{red}$  of about 0.961. In contrast to expectations an increased slope of the quasi-stage characteristics occurs at blade stall. This is mainly due to the fact that losses are limited. It is further amplified because in order to compare the stage characteristics of SGV to test the stagnation pressure ratios are area-averaged (compare Figure 4.4). Compared to the test stall occurs at a slightly higher reduced mass flow. This was achieved by adjusting the loss correlation factors for the rotor. Adjusting the factor of the loss correlations in a way that losses are increased at the rotor yields stall at higher reduced mass-flow. Decreasing the losses by adjusting the factor of the correlation delays the stall to smaller reduced mass flows. Therefore, the factors on the loss correlations are given but this aspect though changes the shape of the characteristics as described in the following.

Close to the working point the slope of the quasi-stage characteristics is predicted reasonable well. But for smaller reduced mass flows the slope of the SGV results is too steep. The slope of the characteristics as well as the radial profiles suggest to increased losses particularly at mid-span and rotor tip, but those values are fixed because the primary target is to predicate the occurrence of stall at the mass-flow found from test data.

Only adjusting the loss correlation factor the compressor characteristics and the

shape of the quasi-stage characteristics couldn't be achieved. In order to obtain a better match the stagnation pressure ratios and degrees of reaction would have to be adjusted as well. Except for minor changes of the radial stagnation pressure rise ratios of the first rotor only the mean values of the adjustable parameters in the SGV design solution were used. In order to achieve a better match of the compressor if possible the radial profiles of the quantities need to be adjusted. The factors available to change the loss correlations though don't allow for radially distributed values. The SGV results though showed that there is significant improvement potential. Particularly adjusting the radial profiles of the parameters is expected to enhance the results.

Overall stagnation pressure ratio of the baseline compressor plotted versus the reduced mass flow at compressor inlet is presented in Figure 4.6. Compressor characteristics of SGV and test are plotted versus each other. SGV and test characteristics are

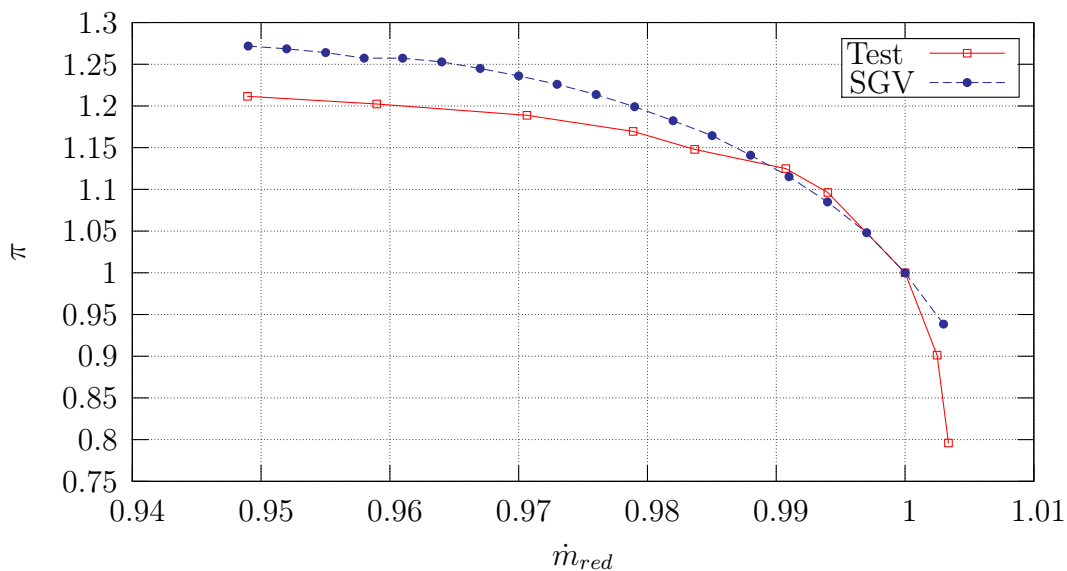


Figure 4.6.: Overall Characteristics of SGV Baseline Compressor at 90%  $n_{red}$

normed to SGV and test working point respectively. At throttled states (i.e. normed  $\dot{m}_{red} < 1$ ) the characteristics are met reasonable well. Also the surge point is found at almost the same normed  $\dot{m}_{red}$ . For de-throttled operating points the characteristics are improvable, but because tip injection is commonly of interest in delaying stall and surge this was skipped.

## 4.2. Computations with Tip Injection

Applying the tip injection computation method developed in chapter 3 to the baseline computations (BL) results for tip injection are obtained. For validation the radial profile of stagnation temperature ratio in the first quasi-stage and the first quasi-stage characteristics will be compared to test data.

### Comparison of SGV results with test data

In order to account for the unsteady effects due to tip injection the work input of the rotor has to be changed (compare section 3.4). Work input is related to the stagnation temperature rise across the stage. In Figure 4.7 (a) stagnation temperature ratios  $\theta$  of the first quasi-stage are compared. Baseline results (i.e. compressor without injection) of test and SGV are plotted versus tip injection results.

An operating point for the baseline test results (operating point at a normed  $\dot{m}_{red}$  of 0.99 on the "Test BL" curve in Figure 4.8) is selected and compared to a SGV computation with a similar radial  $\theta$ -profile of the quasi-stage. Particularly the  $\theta$ -profile at the rotor tip is of interest, because tip injection particularly influences the rotor tip. The SGV baseline operating point found to have a similar radial  $\theta$ -profile as the test baseline operating selected is the one at a normed  $\dot{m}_{red}$  of 0.96 on the "SGV BL" characteristics in Figure 4.8. Comparing the SGV and test BL results it is obvious that at rotor tip ( $r \in [0.75, 1]$ ) the work input of SGV is slightly smaller than in the test. On the remainder of the radius the work input is increased. As pointed out in 4.1 this is because only the stage mean values were considered but the radial profiles wasn't looked at during the process of adjusting the SGV baseline design computation. Considering tip injection where the radial matching is changed this might lead to errors but it is assumed that trends are consistent and the delta values are of similar magnitude.

In order to compare injection and BL results a operating point of the injection test is used that has a similar mass flow through the rotor (i.e. mass flow through front face + injected mass flow) of the first stage. In terms of SGV the operating point at a  $\dot{m}_{red}$  of 0.95 is obtained and for the test the operating point at a  $\dot{m}_{red}$  0.98 results (see Figure 4.8).

Comparing the results of test BL cases and injection cases unloading at the rotor tip which is due to the decreased incidence can be seen. At the lower 80% normed

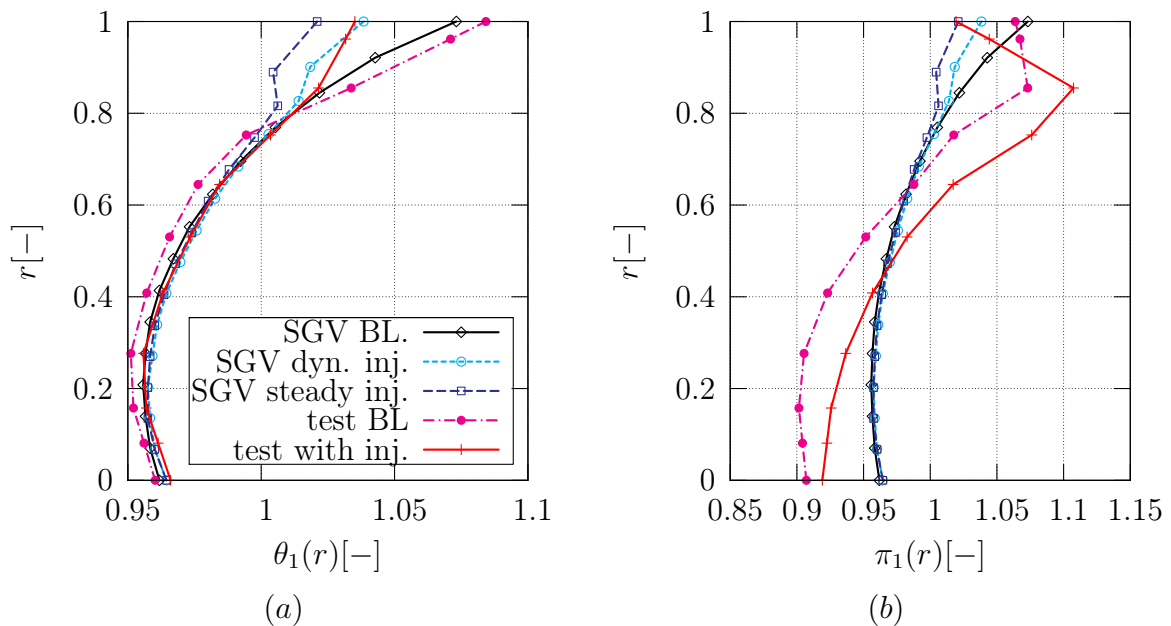


Figure 4.7.: Radial Profiles of SGV and Test results for quasi-stage 1 with Tip injection:  
 (a) Stagnation temperature ratio  $\theta_1$ ; (b) Stagnation Pressure ratio  $\pi_1$

radius the loading is increased. Applying the the computation method for tip injection developed throughout this work in conjunction with SGV, the radial  $\theta$ -profile "SGV dyn. inj." is obtained. At the casing streamline the load reduction in case of SGV (between BL and "SGV dyn. inj.") is slightly lower and at the streamline below the casing it is higher than in case of the test. This is due to the prescription of the radial profile. As pointed out in section 3.4 the radial profile is prescribed in a way that unfavorable gradients to the casing are prevented. The change of the radial profile of the main-flow quantities due to injection is generally limited to a small radial extension and is distributed onto two streamlines. In order to achieve the same integral value the magnitude of this change is decreased. This decreased magnitude of the effects and the increased radial extension is also apparent in the results.

The curve denoted with "SGV steady. inj."  $\theta$ -profile in Figure 4.7 represents a SGV run where the only mass averaged real inflow conditions are prescribed. Thus, in contrast to "SGV dyn. inj." the work input is not corrected for the unsteady part. It is obvious that the unloading of "SGV steady. inj." is higher than for "SGV dyn. inj.". Comparing "SGV steady. inj." and "SGV dyn. inj." to the test it can be seen that in terms of the  $\theta$ -profile "SGV dyn. inj." gives a better match. Hence, it is shown that the unsteady work input plays an important role and can't be neglected. Considering rematching both "SGV dyn. inj." and "SGV steady. inj." underestimate this effect with respect to the test curve.

In Figure 4.7 (b) the radial stagnation pressure ratio profiles associated with the  $\theta$ -profiles presented in Figure 4.7 (a) are plotted. Comparing the results of "test BL" to "SGV BL" a significantly higher pressure loss is apparent at rotor tip in the test results. This difference as pointed out in section 4.1 is due to the effect that the factors for the loss correlations in SGV has to be set in a way that the losses at rotor tip and mid span are underestimated.

Considering the stagnation pressure ratio difference between BL and injection case the change in case of the test is bigger than it is for SGV BL to "SGV dyn. inj.". The difference of stagnation pressure ratio between "SGV steady. inj." and "SGV BL" is greater than in the test case at the casing streamline. As discussed for the  $\theta$ -profiles the magnitude of unloading at the casing itself is less but the radial extent is greater. This as well has to be the case for the stagnation pressure ratio. In the case of "SGV steady. inj." the unloading at the casing is bigger and for "SGV dyn. inj." it is smaller than in the test case. Hence, "SGV dyn. inj." complies better with the test data.

In Figure 4.8 the quasi-stage characteristics of the first stage for test and SGV cases are plotted. Baseline results already have been presented in Figure 4.5 and are in

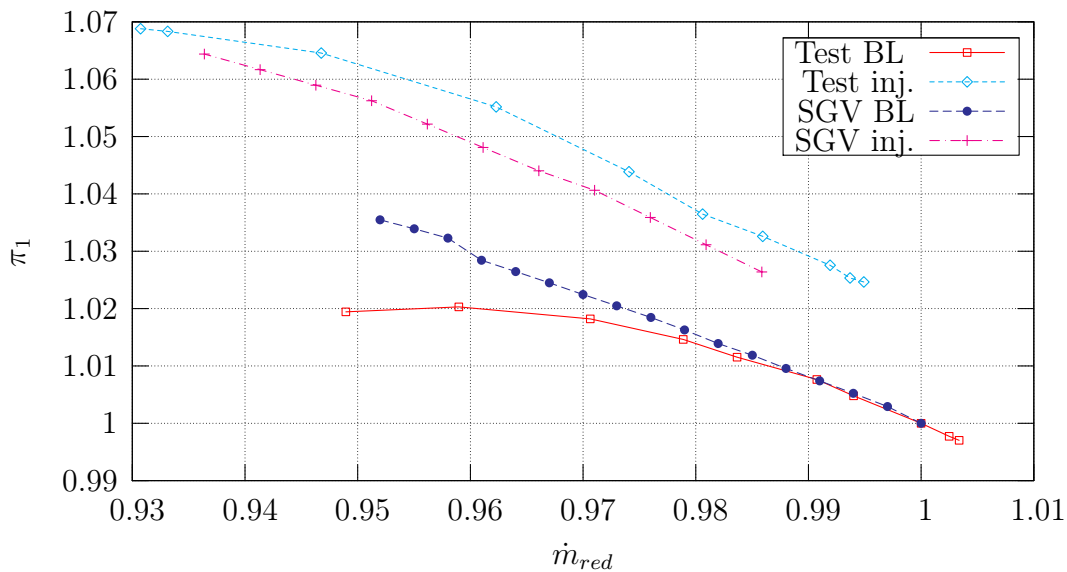


Figure 4.8.: First Quasi-Stage Characteristics of Test and SGV results 90%  $n_{red}$

this plot used as reference only. BL characteristics are normed with their working line point. The results for the test tip injection case and SGV case are normed with the working line point of the associated BL working point. The stage characteristic shows the correct trend even though the shift of the quasi-stage characteristics of BL to injection results for the test case is greater than it is computed by SGV.

Considering the quasi-stage characteristics with injection, both for the test case and the prediction by SGV, the stall point is not reached. In case of the test, the compressor surged before the rotor stalls thus no measurements can take place. SGV is not able to obtain the results for smaller reduced mass flows because the flow field for a rear stage rotor can't be computed at the hub. This could be resolved by optimizing the loss characteristics of the rear stages which was not performed because this is assumed to not directly affect the changes due to tip injection. However, looking at the diffusion factor defined by Lieblein the rotor is close to stall.

# Chapter 5.

## Conclusions and Suggestions for Future Work

The main objective of the present work was to develop a fast method for tip injection calculations in order to enable parametric studies of tip injection and preliminary design. Steady SGV computations were corrected for phenomena that arise when using tip injection system.

In order to obtain a fast computation method various assumptions had to be made. However, the method showed the expected trends and fits test data reasonable well. The main assumptions are discussed in the following before the chapter is finished with considerations about the validation process.

### **Inflow correlation**

Employing tip injection jets enter through the casing and interact with the main-stream. Generally jet and main-stream have significantly different flow velocities and angles. Phenomena that arise through jet main-stream interaction were discussed for example in [15] using CFD results. Matzgeller [21] carried out similar investigations for a setup closely related to the tip injection setups in terms of flow speeds and flow angles. Using these results Matzgeller computed the stagnation pressure loss and deviation of the jets at several positions downstream of the injectors. Using the downstream position of the rotor leading edge with respect to the injector the flow angle and stagnation pressure loss at rotor leading edge are correlated. Altogether these correlations for stagnation pressure loss and deviation are expected to give a good approximation of the inflow condition to the rotor downstream of the injectors.

In order to account for various tip injection setups and compressors several param-

eters that influence the correlation have been considered. Nevertheless, one parameter was not accounted for. Flow velocity of the main-stream is expected to influence the jet main-stream interaction but all CFD computations in [21] were carried out for one main-stream velocity. This main-stream velocity was chosen as an averaged value for the tip injection computations in this work, thus the influence of this issue on this work is expected to be not significant. In literature [15] it is explained that jet main-flow interaction depend on the velocity ratio which was changed in terms of the jet velocity but not in terms of main-flow velocity. Hence, in order to extend the scope of these correlation to account for different compressors and tip injection setups this parameter needs to be considered in the correlation.

### **Dynamic System**

Tip injection changed the flow field in the angular direction as discussed in section 3.1. It was found that this inflow field can be approximated by a Fourier series based on a rectangular input signal where the order was chosen such, that CFD results were fitted best. In the absolute frame of reference this inflow conditions varied with angular position and because of the rotor speed thus results in unsteady inflow conditions to the rotor in the relative frame of reference.

Generally this arrangement would have to be solved using unsteady aerodynamics. Melick [24] showed that the lift obtained by unsteady aerodynamics can be computed by considering system dynamics first and then the flow field is computed using steady aerodynamics. In this way, "effective" inlet quantities are derived that capture the system dynamics. Using effective inlet quantities and the steady lift equation the same lift is obtained as in case of the real inflow conditions and unsteady aerodynamics. This approach was than applied to compressor subjected to inlet distortions.

In this work this idea was modified for tip injection computations. The results obtained using this approach fitted test data reasonable well. Thus it was concluded that this method worked for tip injection as well. However, looking closer at the dynamics system two aspects should be further investigated.

The dynamics system was validated and the results are shown in Figure 3.11. It was found that using a time constant similar to that one suggested by Melick the part of the system output resulting from the system input was captured reasonable well. But another part of the system output was significantly disturbed by the adjacent blade. When the jet hit the LE of the adjacent blade a vortex was shed from the LE

and influenced the flow about the present blade [22]. In order to enhance the system dynamics this disturbance should be accounted for.

The time constant suggested by Melick [24] was used for tip injection as well. System validation showed, that the system can be predicted reasonable well using similar time constants for jet and main-flow section. However, only one particular system with a distinct period and ratio of the jet to the period was considered. It is expected that for common tip injection setups this system can be used but in order to validate it a system identification based on various compressors and tip injection systems should be performed. Further, the time constant was developed for single airfoils by Weinig [33]. In order to adjust it for blade rows as suggested by Lecht [18] a factor defined for the ratio of the lift coefficients was used for the time constants.

Cassina [4] showed that the effects of tip injection depended on  $a_{inj}$  defined in equation 3.5 (i.e. ratio of the jet extension to period) and the extend of the period. Considering mass averaging of the inlet quantities for a segment that completely encloses the jet the mass averaged mean does not depend on the aspect ratio of the injectors. The means of the inflow quantity on the other are used to compute the work input to the system and the losses. Thus, in order to comply with the results obtained by Cassina the means of the inflow conditions have to vary for different aspect ratios. The dynamic system used captured this effect as presented in the following. In case of the dynamic system the time constant varied with time. For jet and main-flow section it depends on the axial flow velocity inside the jet and main-flow respectively. In case of this non-linear system the mean depends on the ratio of the time constants and  $a_{inj}$ . Changing the number of injectors and aspect ratio of the injectors  $a_{inj}$  is changed, thus mean and work input vary. Hence, the observations of Cassina are supposed to be represented using this method. Additionally this effect is influenced by the loss and deviation correlation by Matzgeller [21], that depend on the aspect ratios of the nozzles.

Comparing the results of test and SGV injection results to baseline results it was found that the unsteady work input was significant and improved results. Comparison of unsteady stagnation pressure loss for blade rows with and without injection showed that those were matched good as well. Assuming that the baseline computations were met the first order system is found to be sufficient.

Reduced frequency as defined in section 3.2 can be used to categorize the dynamic systems. If the reduced frequency is in the order of magnitude of 1 the system response varies little in amplitude. The reduced frequency of the tip injection system used

fulfilled this requirement. Consulting CFD results Matzgeller [21] confirmed that the static pressure variation at outlet was small. This allowed for two major assumptions. On the one hand the use of a parallel compressor model has not to be applied and on the other hand just the mean of the dynamic system had to be considered. For a smaller number of injectors though the reduced frequency might not allow for this assumption anymore. A general reduced frequency range (particularly a lower limit) for which this assumptions can be used was not found, but would be of interest for future work.

### **Implementation of the tip injection computation method**

In order to compute the flow field of compressors subject to tip injection the solution process is split into a dynamic system and steady aerodynamics as discussed in section 3.3. Steady aerodynamics are computed using the streamline curvature method based solver SGV. As discussed in section 3.4 a python program was developed that obtains the values of the main-flow using a converged SGV base computation and computes real and effective inlet quantities. Using the effective inlet quantities the unsteady work is obtained and this work is then prescribed to a SGV computation with real inlet quantities. The implementation was performed in order that the SGV source code was not adjusted. In the following assumptions that were applied in order to implement the method into SGV and their impact are discussed.

Tip injection changes the inflow conditions to the rotor downstream of the injection which has to be accounted for using SGV. Flow angle and stagnation pressure were prescribed using outflow angle and stagnation pressure loss coefficient  $\omega$  of a stage that only can be applied to blade rows and change the quantities at the outlet calculation plane of the row. Hence, instead of applying the changed inflow at the location of the injection, inflow conditions are adjusted at the exit of the stator or IGV upstream. In order to be consistent the whole dynamic system considerations and averaging takes place at outlet calculation plane of the row upstream of the injectors. Altogether the effect of this axial shift is assumed to be not to significant because in general the axial distance is small and the casing radius at outlet plane of the upstream blade row and at the inlet plane of the downstream blade row are similar.

In order to compute the inflow conditions, the static pressure at the injectors was required. This static pressure was obtained from a SGV computation without injection. The jets though act like an additional blockage. Thus the main-stream flow speed would increase, yielding a smaller static pressure. In terms of the prescribed flow velocity inside the jets the influence was expected to be small, because the injectors

were choked and the jets are small compared to the main-flow, thus the static pressure and the velocity were not expected to change considerably.

The unsteady work input was realized changing the outlet blade angle. Generally, in order to obtain a changed work input it would be necessary to adapt the turning and deceleration of the flow. In terms of SGV only the outlet flow angle can be changed by changing the blade angle. It is not obvious if this assumption is correct. In order to get an idea about the possible error introduced with this assumption the difference between outflow angle at the rotor with and without injection were compared between CFD and SGV. Computing the difference according to

$$\Delta\beta = \frac{[\beta_{BL} - \beta_{inj}]_{SGV}}{[\beta_{BL} - \beta_{inj}]_{CFD}} - 1, \quad (5.1)$$

where indices BL and inj are results without and with injection respectively, the difference was found to be 20%. Hence the effect of increased work is not purely achieved by turning. As pointed out in section 3.4 a SGV solution with real inflow conditions is obtained which is then corrected to obtain the solution with the corrected work. Hence, assuming that the change in work input would be purely due to further deceleration the outflow would be that of this computation. The angular difference according to equation 5.1 was found to be -40%. This implies that the outflow angle was changed by the unsteady work. Therefore, the unsteady work input of the rotor is a combined effect of additional turning and deceleration with respect to the steady case. The blade angle in the case of unsteady work input is smaller it is expected to be the better approach.

### SGV baseline solution

Test data was available for cases with and without tip injection at the same reduced rotor speed. In case of discrete tip injection as used in this work, jets enter the casing and affect the inflow at rotor tip. Due to a radial change of the streamline distribution because of the jets also the inflow conditions at the remainder of the annulus are modified. This affects the work input of the rotor and thus the outflow conditions yielding different inflow conditions to the following blade rows thus radial and axial matching are changed.

Comparing the differences of the stagnation temperature and pressure rise across the first stage and the stall point of the first stage for results with and without tip injection the computation method was validated. As pointed out above tip injection affects radial and axial matching that depended on geometry such that first the SGV baseline computation had to be adjusted to meet the test baseline. The adjustment process was

based upon the quasistage characteristics such, that only one mean radial value was fitted per stage. It was found that this might be an oversimplification considering the effects of tip injection which changed the radial inflow profile of the stages. In order to clear out any uncertainties the baseline solution should be improved. Particularly the loss correlations and the blade angles should be adjusted looking at radial profiles.

# Bibliography

- [1] <http://www.newac.eu/>
- [2] <http://intra-cax/wiki/cae/aero/wiki/index.php/Category:SGV>
- [3] Bock S., Horn W., and Sieber J.: *Active Core Technology within the NEWAC Research Program for Cleaner and more Efficient Aero Engines* in NEWAC Publication, No. 005
- [4] Cassina G., Beheshti B., Kammerer A., and Abhari R.: *Parametric Study of Tip Injection in an Axial Flow Compressor Stage* In ASME Turbo Expo 2007, GT2007-27403
- [5] Cumpsty N. A.: *Compressor Aerodynamics* Krieger Publishing Company, Malabar FL, 2004.
- [6] Bräunling W. J. G.: *Flugzeugtriebwerke* Springer Verlag, Berlin, 2004
- [7] Ericsson L. E. and Reding J. P.: *Fluid Mechanics of Dynamic Stall Part I. Unsteady Flow Concept* In Journal of Fluids and Structures 1988 2, 1-33
- [8] Fung Y. C.: *An Introduction to the Theory of Aeroelasticity* John Wiley and Sons, inc., New York 1955
- [9] Green R. *Aerodynamics and Fluid Mechanics 3* Lecture Notes Univeristy of Glasgow, 2007
- [10] Greitzer E. M.: *The Stability of Pumping Systems* Department of Aeronautics and Astronautics, Massachusetts Institute of Technology, Cambridge 1981
- [11] Grieb H., Schill G. and Gumucio R.: *A semi-empirical method for determination of multistage axial compressor efficiency* AMSE Paper No. 75-GT-11
- [12] Hennecke D. and Wörrlein K.: *Flugantriebe und Gasturbinen* GFA Darmstadt 2. Auflage WS2000/2001
- [13] Hiller S., Matzgeller R. and Horn W.: *Stability Enhancement of a Multistage Compressor by Air Injection*. In ASME Turbo Expo 2009, GT2009-59868

- 
- [14] Kahl G. and Wurm S.: *Zukunftsweisende neue Technologien für Hochdruckverdichter der nächsten Generation* 2004
- [15] Kahn Z. U.: *On vortex generating jets*. International journal of heat and fluid flow, Vol. 21, pp.506-511, Elsevier sciences inc., 2000
- [16] Kármán Th. and Sears W.: *Airfoil Theory for Non-Uniform Motion* in Journal of the Aeronautical Sciences 1938, Volume 5 Number 10
- [17] Köhler C.: *Berechnung von Kennfeldern eines ummantelten Propfans unter Berücksichtigung der gegenseitigen Beeinflussung der gegenläufigen Verstellrotoren* Diplomarbeit TU Braunschweig, 1990
- [18] Lecht M.: *Beitrag zum Verhalten von Axialverdichterstufen bei stationärer Störung in der Zuströmung*. Forschungsbericht DFVLR-FB 83-39. Institut für Antriebstechnik Köln, 1983
- [19] Lieblein S.: *Loss and Stall of Compressor Cascades* ASME paper No. 58-A-91
- [20] Lieblein S.: *Aerodynamic design of Axial-Flow Compressors* NASA-Report SP 36 pp. 183-226
- [21] Matzgeller R.: *Zusammenfassung bereits durchgeführter Arbeiten (1+2 Quartal 2010) - Ausblick auf nachfolgende Themen*, Presentation - MTU Aero Engines GmbH, 2010
- [22] Matzgeller R.: *private communication* 2010
- [23] Mazzawy R., Banks G. and Weber C.: *Compressor Critical Response Time Determination Study* Report no. AFAPL-TR-76-45, 1976
- [24] Melick H. and Simpkin W.: *A unified Theory of Inlet/Engine Compatibility* AIAA paper No. 72-1115
- [25] Prince J. D., Wilser D. D. and Hivers D. E. *Study of Casing Treatment Stall Margin Improvement* NASA CR-134552, 1974
- [26] Kern M. et. al. *Performace Validation document Rig 260 built 3* Technical Note - MTU Aero Engines GmbH, 2004, MTU-N09TEA-0071
- [27] Schneider T.: *Numerische Untersuchung der Verdichterabstimmung an einem mehrstufigen Hochdruckverdichter mit Fluideinblasung* Diplomarbeit TU Berlin, 2009
- [28] Smith L. H.: *The radial-equilibrium equations of turbomachinery* Trans ASME

- Journal of Engineering for Power 88: 1-12, 1966
- [29] Strazisar J.A.: *Compressor stall control through endwall recirculation* Proceeding of ASME Turbi Expo 2004, Power for Land, Sea and Air, 2004 GT2004-54295
- [30] Suder K., Hathaway M., Thorp S., Strazisar A., Bright M.: *Compressor Stability Enhancement using discrete Tip Injection* in ASME Turbo EXPO 2000, GT2000-GT-650
- [31] Wu C.H.: *A general theory of three-dimensional flow in subsonic or supersonic turomachines of axial-, radial- and mixed-flow type* NACA TN 2604, 1952
- [32] Weigl H., Paduano J., Frechette L., Epstein A., Greitzer E., Bright M. and Strazisar A.: *Active Stabilization of Rotating Stall and Surge in a Transonic Single Stage Axial Compressor*, ASME Journal of Turbomachinery, Vol 120, No.4,pp 625-636, 1998
- [33] Weinig F.: *Die Strömung um die Schaufeln von Turbomaschinen Beitrag zur Theorie axial durchströmter Turbomaschinen* Barth, Leipzig 1935
- [34] Willinger R.: *Numerische Berechnung thermischer Turbomaschinen* Skriptum TU Wien, 2008

# Appendix A.

## Injection.ein

In the following the file "injection.ein" is described. This file is the input file for the tip injection computation and it has to contain the following input.

- *path*: Is the path to the SGV executable.
- *pt\_ein* [Pa]: The stagnation pressure upstream of the nozzle  $p_{t,inj}$  in the high stagnation pressure reservoir (see 1.3)
- *loss\_corr*: (True/False) If this flag is set to "True" the loss correlation according to Matzgeller [21] is performed (see equation 3.3)
- *f\_cd*: This factor  $f_{cd}$  is used to correct the dynamic head loss obtained from the correlation according to Matzgeller in the form  $c_{d,LE} = f_{cd}c_{d,M}$  where  $c_{d,LE}$  is the dynamics pressure loss obtained from the correlation and  $c_{d,M}$  is the value used for the tip injection computation.
- *deviation\_corr*: (True/False) If this flag is set to "True" the deviation correlation according to Matzgeller [21] is performed (see equation 3.4)
- *f\_alpha*: This factor  $f_{alpha}$  is used to correct the deviation correlation according to Matzgeller in the form  $c_{\alpha,LE} = f_{alpha}c_{\alpha,M}$  where  $c_{\alpha,M}$  is the deviation computed using the correlation and  $c_{\alpha,LE}$  is the value used for the tip injection computation.
- *cd*: If the flag *loss\_corr* is set to false the dynamic pressure loss has to be provided by the user (If no dynamic pressure loss is desired the value has to be set to 1).
- *c\_alpha*: If the flag *deviation\_corr* is set to false the value for the deviation has to be provided by the user (If no deviation is desired the value has to be set to 0).

- *pos* [m]: is the axial distance of the the lower edge of the injection jet to the rotor leading edge  $x_{inj}$  (see section 3.1 Figure 3.2) [m]
- *width* [m]: is the width of the nozzle
- *m\_inj* [%]: is the mass flow through the injectors in percent of the core mass flow.
- *Tt\_ein* [K]: is the stagnation temperature of the injection system upstream of the nozzle.
- *alpha\_ein* [°]: The angle of the injectors to the circumferential direction (see 1.3).
- *n\_slot*: is the number of injectors.
- *gitter*: is the index of the blade row ("Gitter" value given in SGV).
- *stufe*: is the index of the stage ("Stufe" value given in SGV).
- *ar\_nozzle*: is the aspect ratio of the nozzle throat  $\frac{w_t}{h_t}$  where  $w_t$  and  $h_t$  are width and height respectively (see section 3.1 Figure 3.2)
- *plot*: (True/False) If this flag is set to true several plots showing the effects of tip injection are created.
- *comparison*: (True/False) If this flag is set to true a baseline SGV computation with the same flow coefficient through the rotor downstream of the injection is created.

For debugging and program development an "expert" version was created where several additional parameters have to be provided. These are discussed in the following:

- *k1*: this constant is a multiplier of the Melick time constant for the dynamic system for the velocity in the form  $k1 \frac{c_b}{c_{ax}(t)}$  (see equation 3.37)
- *k1a*: this constant is a multiplier of the Melick time constant for the dynamic system for the angle in the form  $k1a \frac{c_b}{c_{ax}(t)}$  (see equation 3.37)
- *k2*: is a factor for a desired first derivative in the input signal and should be set to 0 (obsolete).
- *k2a*: is a factor for a desired first derivative in the input signal and should be set to 0 (obsolete).
- *ktau1*: this quantity can be used to adjust the time constant in the jet section in the form  $\tau_{used} = ktau1 \tau_M$

- 
- *ktau2*: this quantity can be used to adjust the time constant in the main-flow section in the form  $\tau_{used} = ktau2\tau_M$
  - *test*: a factor that multiplies the final value of all quantities that are adjusted due to injection (i.e.  $\Delta q_{used} = test\Delta q_{computed}$ )
  - *n\_relax*: number of relaxations while setting the real and effective inflow conditions (see 8. *Running SGV base runs* in appendix B)
  - *calc*: (True/False) if this flag is set to true, than just the real and effective inflow conditions are computed and the results are written to a file.
  - *analyse*: (True/False) if this flag is set to true, a s2.ein with real inflow conditions is created but not solved with SGV.
  - *averaging*: (mass/area) gives the type of averaging of the radial profiles for the comparison SGV run. If set to "mass" then the equivalent flow coefficient is obtained by mass averaging of the radial profiles and if set to "area" this value is obtained from area averaged radial profiles.
  - *maxiter*: is the maximum number of iterations for the adjustment of the exit flow angle in order to obtain the unsteady work
  - *circumf\_averaged*: (True/False) if set to True a computation with circumferential averaged inlet flow quantities is performed. (obsolete)

# Appendix B.

## Program Flow Chart 2

In section 3.4 a flow chart focusing on the procedure in terms of the working principle was presented. The flow chart presented in the following presents the program in more detail and is closely related to the program. First the defined methods used are presented with input and return values. Then the main program is explained.

This section is written to understand the source code written in Python and is not required to understand the working principle of the method. Therefore this section refers to values used in SGV and the source code and it might be difficult to understand it without access to the source code and SGV. However, this section is not required to understand the thesis, it is thought to help future developers of this program to understand the code.

### Defined Methods

The methods as defined in the programs are presented in the following list and their input values, function and return values are briefly discussed.

1. *read\_list\_e(datei, val, ebene, kmax)*: This method parses the s2.ges.lst located at the path given by the string *datei* and reads the radial profile of a physical quantity specified by the string *val* on the calculation plane with index *ebene*. *kmax* is an integer with the number of streamlines such that the method can check if the return vector contains a value for every streamline. The return value of this method is vector of length *kmax* containing the radial profile of *val*. *val* is the first keyword in the line of the desired quantity (e.g. PT, TT, ...)
2. *read\_list\_g(datei, val, ebene, kmax)*: This method parses the s2.ges.lst located at the path given by the string *datei* and reads the radial profile of a physical

quantity specified by the string *val* of the blade row with index *ebene*. *kmax* is an integer with the number of streamlines such that the method can check if the return vector contains a value for every streamline. The return value of this method is vector of length *kmax* containing the radial profile of *val*. *val* is the first keyword in the line of the desired quantity (e.g. INC, OMEGA, ...)

3. *read\_list\_s(datei,val,ebene,kmax)*: This method parses the s2.ges.lst located at the path given by the string *datei* and reads the radial profile of a physical quantity specified by the string *val* of the stage with index *ebene*. *kmax* is an integer with the number of streamlines such that the method can check if the return vector contains a value for every streamline. The return value of this method is vector of length *kmax* containing the radial profile of *val*. *val* is the first keyword in the line of the desired quantity (e.g. Work, ...)
4. *read\_ebene(datei,ebene)*: parses the s2.ein file located at the string *datei* and gives back a vector of string names defined in the form of (ebe1\_up, ebe2\_up, n, ebe1\_down, ebe2\_down, c) where ebe1\_up, ebe2\_up, n, ebe1\_down and ebe2\_down are the calculation plane indices of inlet plane and outlet plane to the row upstream and downstream of the injection respectively. n is the rotor speed and c is the chord length. *ebene* defines the row index (gitter) of the rotor downstream of the injection.
5. *relativ(u,c,alpha)* : is the transformation of flow velocity *c* and flow angle *alpha* from the absolute to the relative frame of reference. *u* is the blade speed. The vector w,beta (i.e. flow velocity and flow angle in the relative frame of reference) is the return value.
6. *absolut(u,w,beta)*: is the transformation of flow velocity *w* and flow angle *beta* from the relative to the absolute frame of reference. *u* is the blade speed. The vector c,alpha (i.e. flow velocity and flow angle in the absolute frame of reference) is the return value.
7. *sgv(dat,folder)*: performs an SGV run with a valid s2.ein located at the path given by the string *dat*. First the s2.ein is copied to the working folder and renamed to fort.10 (i.e. input file for the FORTRAN program SGV and then SGV is executed. The results files fort.13 and fort.51 are then copied back into the *folder* as s2.ein and s2.ges.lst respectively
8. *lin\_int(x,x\_vec,y\_vec)*:is the linear interpolation of *x* on the vectors *x\_vec* and *y\_vec*. The return value is the float digit resulting from the linear interpolation.

9. *multil(dat, val)*: is used to get the radial profile of the physical quantity *val* from the s2.ein located at the path defined by the string *dat*. *val* is the first keyword in the line of interest.
10. *sgv\_con(datei)*: is used to check if a SGV run has converged. If an SGV run is converged a entry "Qualitaet der Stromlinienlage: 1 " is created. This method parses the file located at the string *datei* and looks for this entry. If it exist the return value is True, otherwise False is returned (Boolean)
11. *read\_list\_e\_m(datei, val, ebene)*: like *read\_list\_e(datei, val, ebene, kmax)* but instead of obtaining the radial profile the mean is obtained and thus the number of streamlines is not required.
12. *read\_list\_s\_m(datei, val, ebene)*: like *read\_list\_s(datei, val, ebene, kmax)* but instead of obtaining the radial profile the mean is obtained and thus the number of streamlines is not required.
13. *rad\_prof(r, h\_inj)*: computes the radial profile according to 3.4. *r* are the radial positions of the streamline along the calculation planes and *h\_inj* is the height of the jets as defined in section 3.1
14. *l\_transp(inlist)*: transposes the list *inlist* and returns the obtained list.
15. *area\_av(inlist, rlist)*: computes the area averaged value of the *inlist* given at radial positions *rlist* and returns the area averaged mean.

## Main Program

This flow chart is an extended version of that presented in section 3.4.

1. *Organisation*: First the file "injection.ein" is read to get the required additional input. Then the folder structure containing following directories is created
  - *working\_folder*: in this folder the SGV program is placed and all SGV runs are performed in there
  - *eintritt(engl. entry)*: in this folder files regarding the computations with real inflow quantities are placed
  - *delta*: in this folder files regarding the computations with effective inflow quantities are placed
  - *run*: in this folder files regarding the computations with real inflow quantities and corrected work are placed

and the SGV solver is copied to the "working\_folder"

2. *SGV pre-run*: A pre-run with the provided s2.ein is performed to check if the file is valid and to obtain the result file. Then the resulting s2.ein and s2.ges.lst are copied to the folders *eintritt*, *delta* and *run*.
3. *Reading required quantities from the pre-run results*:
  - The mass and number of streamlines are obtained from the file s2.ein.
  - Running the method *read\_ebene(datei,ebene)* with the pre run s2.ein and the gitter value from the input file injection.ein the calculation plane indices of upstream and downstream rows inlet and outlet as well as rotor speed and chord length of the profile.
  - Using the plane indices obtained above the required main flow quantities are obtained using the method *read\_list\_e(datei,val,ebene,kmax)* with the s2.ges.lst.
4. *Inflow correlations*: The correlations according to Matzgeller [21] are applied and the so corrected jet values at rotor leading edge is obtained.
5. *Real Inflow Conditions*: Using the main flow quantities and the corrected jet values the Fourier series inflow conditions as derived in section 3.1 are computed. All computations are only performed for the casing streamline quantities.
6. *Effective Inflow quantities*: Real inflow quantities are first transformed to the relative quantities. Effective quantities are obtained as discussed in 3.3 and then transformed back to give effective stagnation pressure, effective stagnation temperature and effective absolute flow angle.
7. *Averaging*: In order to obtain the mean steady work the effective and real quantities are averaged
8. *Running SGV base runs*: For the SGV base runs the inflow conditions have to be adjusted as defined in section 3.4. One run is with real inflow conditions and the other with effective. For each run omega (i.e. VLGI in SGV terms) the outflow angle (i.e. BETZ in SGV terms) and the stagnation temperature difference (i.e. DTZ in SGV terms) have to be adjusted. Using relaxation and the method *rad\_prof(r,h\_inj)* first the profiles of above quantities are created. Then the adjusted input file is created by parsing the s2.ein file in the folder (*eintritt* for real inflow and *delta* for effective inflow) and adjusting it as described in the following. If a line does not contain any value of interest it is written without

any change. Otherwise the values are changed and the lines are replaced. Then the SGV runs for real and effective inflow quantities are performed.

9. *Check Convergence*: If the solutions for effective and real inlet conditions are converged the iterative process for the final solution is started.
10. *Corrected Work*: Starting from the solution with real inlet condition and the blade outlet angle is adjusted in a way to give the unsteady work as discussed in this section. This process is iterative. For every iteration the input file is adjusted similar as discussed in point 8 for the blade angles. Real inflow profiles as well are adjusted in this run that in case of a changed radial streamline distribution at the IGV outlet the values are prescribed correctly. As discussed in section 3.4 the resolution in radial direction is coarse such that prescribing the radial profile at the actual streamline position at every iteration the values are fixed at the streamline position and thus are not interpolated.
11. *Post Processing*: If the solution converged a summary file is written and plots presenting the effects of tip injection are created.

In the "expert" version additionally a file "calculation.dat" is created. This file contains the values that are obtained by the computation of the dynamic system. The entries are self-explanatory. Post processing is performed using the PYPLOT toolbox that has a similar syntax to the MATLAB plot command. Using switches at the beginning of the plot section the single plots can be switched on and off. Additionally a general summary file is written, where the entries are self-explanatory.